# Buckling and postbuckling behavior of cracked structures.

# BUCKLING AND POSTBUCKLING BEHAVIOR OF CRACKED STRUCTURES

by

Mehmet Sahin

Presented to the Graduate and Research Committee of

Lehigh University

In Candidacy for the Degree of

Doctor of Philosophy

In

Mechanical Engineering

**Lehigh University**

**September 2004**

Approved and recommended for acceptance as a dissertation in partial fulfillment of the requirements for the degree of Doctor of Philosophy.

08/26/2004
Date

Prof. Herman F. Nied
Dissertation Advisor

August 23, 2004
Accepted Date

Committee Members

Prof. Terry J. Delph

Prof. Fazil Erdogan

Prof. Joachim E. Grenestedt

Prof. Herman F. Nied
(Dissertation Advisor and
Chairman of the Committee)

Prof. Raymond Pearson

# Acknowledgments

This study was made possible by the financial support from the Semiconductor Research Corporation (SRC) under contract No: 826.002

The author wishes to express his grateful appreciation and thanks to his advisor, Prof. Herman F. Nied, for his invaluable, continuous support and great guidance throughout the Ph.D. study. Cooperation of the Ph.D. committee members is also appreciated.

I would like to thank the following for their help and support during this research.

Dr. Murat Ozturk, for his valuable help, advice, comments, support, and for being available anytime he can be during my entire Ph.D. study.

Dr. Gary Harlow, for his support at the beginning of my Ph.D. study.

My wife, for her patience, support, understanding, and taking care of my children more than me during the study.

# TABLES OF CONTENTS

# LIST OF TABLES

# LIST OF FIGURES

# ABSTRACT

In this study, finite element formulation and solution procedures for buckling and post-buckling analysis of regular and cracked structures under various loading conditions were studied. The study consists of two main parts. The first part focuses on the finite element formulation for buckling (eigen) analysis of regular and cracked structures and some eigen-analysis applications of cracked structures. The second part covers post-buckling analysis procedures with some applications. Buckling and post-buckling analysis of cracked structures requires special elements and additional procedures to trace fracture information during pre-and post-buckling stages. The "enriched crack tip element" is one of the special element types used to adopt the crack tip stress singularity into the finite element method. By using this type of element, post-buckling fracture information at crack tips or crack fronts in 3-dimensional structures can be properly traced with a high degree of precision

In the first part of this study, basics of continuum mechanics, strain and stress definitions, and equilibrium equations are derived. Formulation of the finite element equations based on continuum mechanics was obtained. The subspace iteration method, as an eigen-solution technique, with effective sparse matrix storage format, was implemented into the FRAC3D finite element analysis software. Thin plates with cracks or cutouts under tensile loads exhibit local buckling. Although, this problem has been known for decades, it presents very difficult mathematical challenges even in cases with geometric simplicity. For example applications, buckling analysis of

cracked thin plates with inclined and straight central cracks under tensile loads were analyzed. Parametric studies were carried out to examine the effects of geometric and material properties on the critical buckling loads.

In the second part of this study, post-buckling analysis procedures are discussed and a perturbation method is applied to obtain postbuckling solutions for cracked structures. It was observed that post-buckling fracture behavior is fundamentally different than linear fracture analysis, in which buckling and large deformations are not considered. It can be concluded that fracture analysis of structures with cracks that exhibit localized buckling under tensile, thermal or other loading conditions, should be analyzed correctly by using coupled fracture/buckling and post-buckling analysis.

# CHAPTER ONE: INTRODUCTION

## 1.1 Background

There are various forms of local or global structural failure modes which can occur either sequentially or at the same time. Combined fracture and buckling behavior is more common in layered structures such as, composites, electronic packages, or any other structures manufactured with layering techniques. However, simple structures such as thin isotropic plates, shells, and membranes with cracks can also buckle locally under different loading conditions even under tensile loading. Layered structures consist of highly dissimilar materials with large differences in material properties, thermal coefficients, and geometry. Initial delaminations caused by manufacturing defects or excessive loading during service life are potential areas for further local failure under different loading conditions. For examples, blisters can form in electronic packages due to initial debonds between the layers under thermal and moisture induced loads. Local buckling of cracked areas show bifurcation type buckling and cause sudden change in deformation, stress redistribution and consequently change fracture parameters significantly. Postbuckling behavior can occur in layered structures during manufacturing and service life. This damage can result in global or local failures depending upon the size and form of the damage. Thus, it is highly desirable to develop predictive methodologies that can be used to estimate the life of the structure based on some pre-existing damages, e.g. cracks,

delamination etc. "Fail-safe" design methodologies based on fracture mechanics information can be used in conjunction with non-destructive inspection techniques.

## 1.2 Fracture and buckling

Simultaneous occurrences of fracture and buckling is more likely in thin structures with cracks or in layered structures that contain delaminations, subjected to compressive stress distribution around the crack. The compressive stress around the crack can be local even though the global load may be tensile loading. The simplest example of this is a thin plate with a central crack, subjected to tension at the plate's outer edges. In this case, the second principal stress distribution (parallel to the crack) around the surface of crack is compressive and can cause local buckling Other common examples of local buckling are observed in layered structures with pre-existing delaminations, such as composites, coatings, microelectronic packages, etc. [1, 2].

Existence of multi-layered configurations with interfaces represents potential sites for damage initiation and growth of interfacial cracks. Local buckling can develop in the neighbourhood of these interfacial cracks due to compressive stresses caused by various loading and boundary conditions. Material imperfections in composite materials are almost inevitable during manufacturing due to improper bonding of the materials. Improper bonding during manufacturing processes and excessive loads, e.g. impact, thermo-mechanical loads, and fatigue can result in

significant reduction in load-bearing capabilities. Delamination, once initiated, can grow under fatigue loading and the local stress near the delamination may be redistributed such that another delamination may appear in another location. Debonds may continue to grow and accumulate until a structural failure occurs, such as buckling or fiber failure. Although delamination may not cause total collapse of the load-bearing capacity of the component, it may significantly reduce the stiffness of the structure and may be a precursor to the global collapse. Therefore, knowledge of a composite's resistance to interlaminar fracture is useful, not only for product development and material screening, but as a generic measurement of the interlaminar fracture toughness of the composite for establishing design allowables for damage tolerance analyses of composite structures.

From a structural mechanics perspective, electronic packages are composite structures consisting of dissimilar materials. In electronic packages, different layered materials, with different elastic and thermal properties are fabricated into a single package for different functional and electronic purposes. Stresses are largely due to differences in thermal properties of the layers, material imperfections, manufacturing defects, and cyclic thermal loading. Blisters in electronic packages are a buckled form of delamination, usually caused by thermal and moisture induced stresses. Therefore, it is highly desirable to develop predictive methods to estimate the life of the packages having these kinds of imperfections.

Design methodologies based on statistical methods require information about operation loading limits, material imperfections, such as preexisting flaws and geometric variations of the structure. Development of predictive methodologies for

estimating life of a structure based on a fracture mechanics methodology is highly desirable and requires computational tools suitable for this approach. The finite element method is widely used and seems to be the most appropriate numeric tool for buckling and postbuckling analyses, especially if the structure contains cracks. However, current commercially available finite element packages have limited capabilities for the analysis of cracked structures, especially if postbuckling is involved. In this study, the FRAC3D finite element package [3, 4] was modified to examine buckling and postbuckling analysis of coupled fracture/buckling problems.

## 1.3 Examples of combined fracture and buckling

There are numerous examples of buckling problems combined with fracture behavior. Some commonly encountered problems are examined in this section. First, initiation of this type of failure mechanisms requires the existence of cracks, which may exist because of manufacturing defects, or excessive loading, such as impact. The second phase of the failure is associated with buckling and postbuckling behavior. After accumulation of compressive loads around the cracks, buckling can occur, resulting in redistribution of stresses. Postbuckling always exhibits nonlinear behavior, which requires special solution methods, because of the resulting large displacements that can occur after buckling.

### 1.3.1 Plate with elliptical hole and crack

Surprisingly, certain structures with cracks or cutouts that are subjected to global tensile loads, can exhibit local buckling. This is due to local compressive stress distributions around these free surfaces. Fig. 1-1 shows two buckling modes of a cracked plate, subjected to axial tensile load with $a/b = 0.5$ ($a$ = half crack length, $b$ = plate width) aspect ratio. The buckling in this example is local and may or may not cause global failure, depending on the material properties, the magnitude of the loading and whether crack propagation occurs. If the load exceeds a critical buckling load, the first mode of local buckling may suddenly develop around the opening of the crack. The first mode shape is similar to a pop-up. Postbuckling behavior is very different than the deformation in the pre-buckled state and causes out of plane deformation, a stress redistribution, and changes in the fracture parameters. Linear elastic analysis is limited to predicting behavior in the pre-buckled state and cannot be used to predict postbuckling behavior. A 3-D nonlinear analysis is essential for the solution of these types of coupled buckling/fracture problems. The sudden out of plane displacement, is a characteristic of this type of problems.

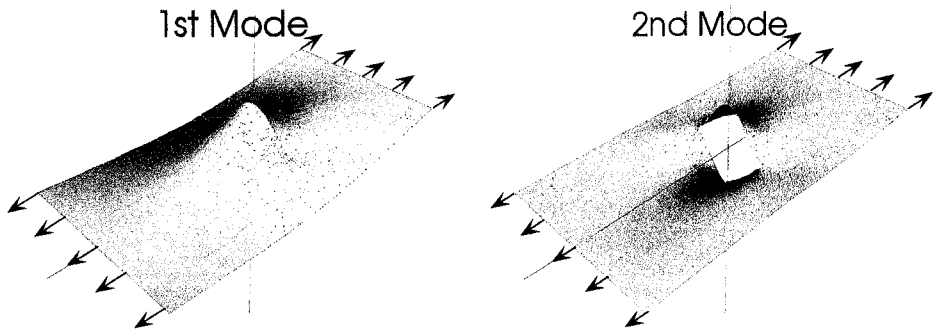


**Fig. 1-1** First two buckling modes of a cracked plate with a/b = 0.5 aspect ratio

In planar structures subjected to tensile or compressive loads, e.g. plates, shells and films, compressive stresses develops around the cracks or cutouts. When the loads reach a critical level, sudden out of plane displacements occurs. If the loading continues to increase after the first buckling level is reached, the resulting deformation moves into the postbuckled state, with higher buckling modes contributing to the deformed shape, i.e. the subsequent total displacements. However, the most dominant mode shape is usually the first buckling mode shape.

Fig. 1-2 and Fig. 1-3 show normalized first principal stress ( $S_1 = \sigma_1 / \sigma_0$ ) and second principal stress ( $S_2 = \sigma_2 / \sigma_0$ ) contours, for a plate subjected to uniaxial uniform stresses applied to the ends. The $X$ and $Y$ axes are normalized axes with respect to half crack length, i.e., $X = x / a$, and $Y = y / a$. Thus, the normalized crack length is two. Note that the first principal stresses values are positive except near the crack free surface where the stress is zero, i.e., there is no internal crack surface pressure. However, the second principal stress ($S_2$) is compressive parallel to the

crack surface and reaches a maximum asymptotic value $S_2$ = -1, ($\sigma_2 = -\sigma_0$), parallel to the crack surface. This stress distribution is the main driving force for local buckling when the global stress $\sigma_0$ reaches a critical value, which is called critical buckling stress.

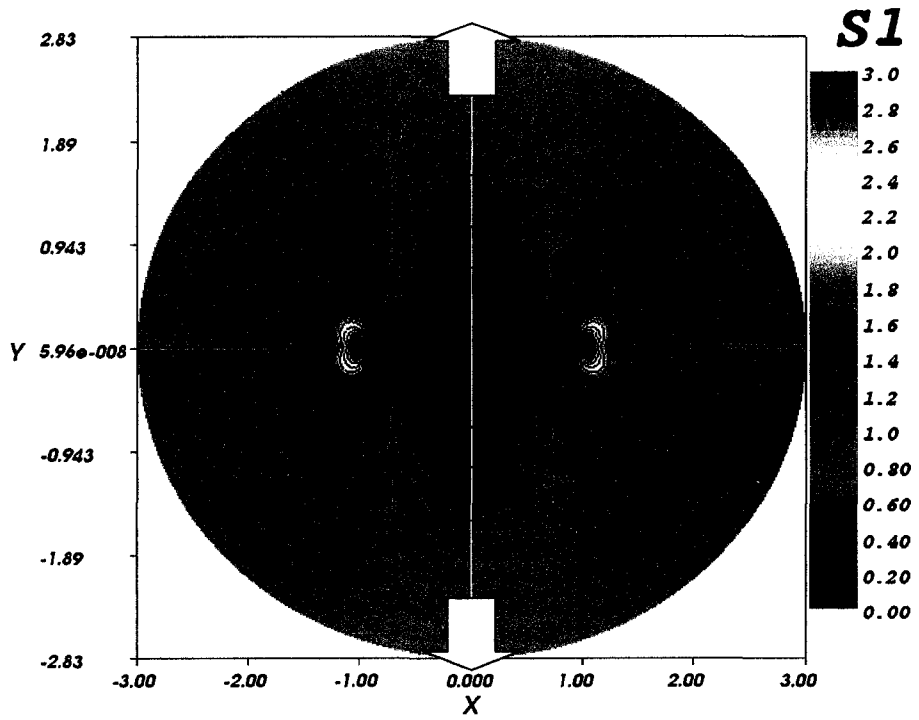


**Fig. 1-2** Normalized first principal stress $S_1 = \sigma_1 / \sigma_0$ distribution around a crack before local buckling. Thick contour lines show 1.0.

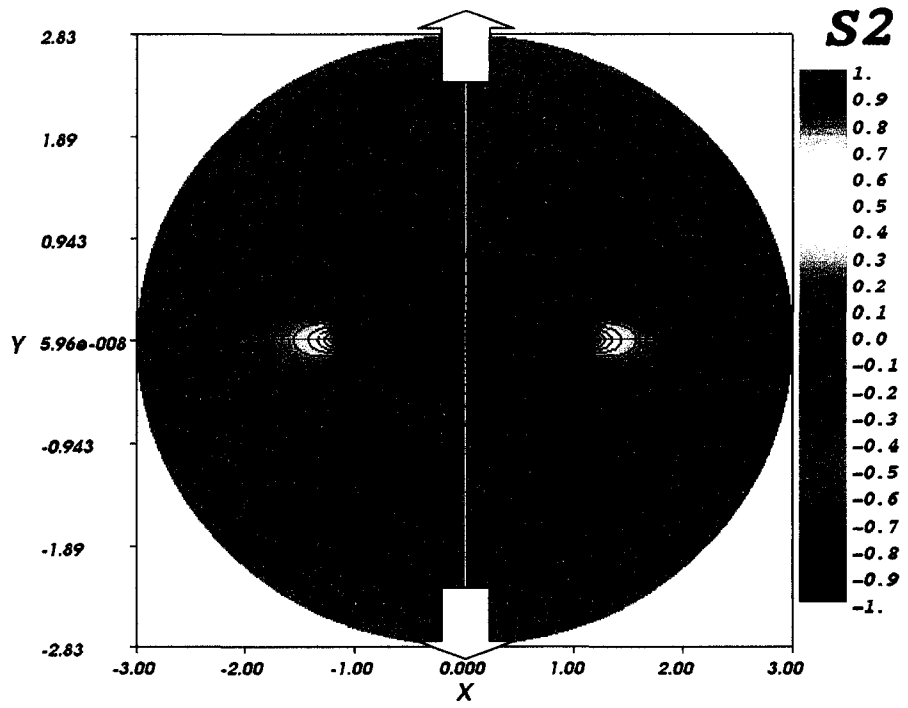


**Fig. 1-3** Normalized second principal stress $S_2 = \sigma_2 / \sigma_0$ distribution around a crack before local buckling. Thick contours show 0.0 contour levels

Plates with circular or elliptical holes show similar compressive stress distributions, but spread on a smaller region of the cutout surface. The comparison of compressive stress distributions for a cracked plate in Fig. 1-3 and a plate with an elliptical hole in Fig. 1-4, shows that the cracked plate is more likely to buckle when subjected to the same level of applied external tensile load. It can be concluded that the critical buckling load for the cracked plate is smaller than it is for a plate with an equivalent elliptical cutout having major axis equal to the crack length.

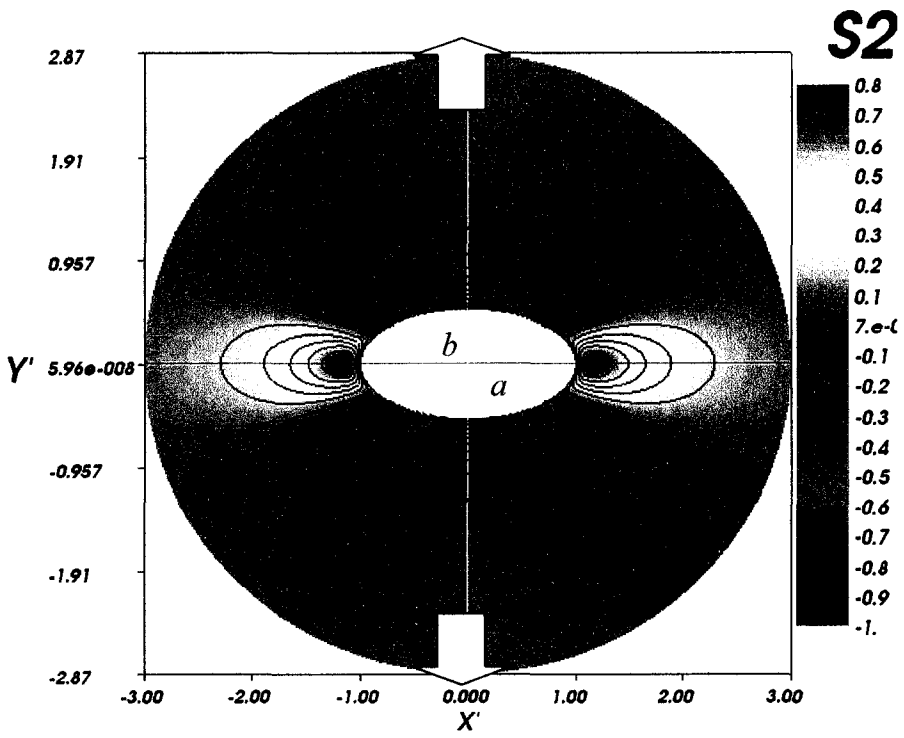


**Fig. 1-4** Normalized second principal stress $S_2 = \sigma_2 / \sigma_0$ contours for an elliptical hole ($b / a = 0.5$), dark thick contour lines show 0.0 contour level.

### 1.3.2 Delamination buckling in composite materials

Analysis of certain types of delaminated structures can be simplified by reducing the problem to a 2-D analysis [1, 2]. If the delamination is sufficiently long and loading is constant along the dimension in the depth direction a plane strain analysis is possible. Alternatively, an axisymmetric delamination can be reduced to 2-D if the geometry, elastic properties, loads, and boundary conditions are all axisymmetric, nothing varies in the angular direction and material points have displacements components only in radial and axial directions. These simplifications

are limited in scope and can be applied only in certain idealized cases. Three dimensional modeling often requires more realistic analyses. For example, initial axisymmetric buckling may quickly become generalized 3-D non-symmetric due to secondary circumferential buckling. Calculation of the fracture parameters for these kinds of problems is essential for accurate life estimate of structural parts with a postulated flaw.

Delamination of layered structures, e.g. composite materials, is another example of coupled buckling and fracture. A delaminated zone in a laminate panel can be caused by manufacturing defects, production errors, impact damage or the presence of cut outs or splices. The delamination acts as an initial imperfection. When the cracked panel is loaded with a compressive force or thermal loading, the debonded region may buckle. In thermal loading, because of the different coefficient of thermal expansions (CTE) of the layers, the layers may expand by different amounts, and cause tensile or compressive stresses depending on the detailed nature of the thermal loading, i.e. heating or cooling. Fig. 1-5 shows a buckled cross-section of a delaminated composite material subjected to compressive loading at the left and right ends. Delamination reduces the compressive strength and the local buckling load of the composite structure. It can also lead to global failure at a lower load than the undamaged composite structure. To estimate the overall performance of a composite, it may be necessary to identify the influence of the buckling and delamination failure. It is obvious that knowing the fracture properties related to the delamination process can help to estimate stability of the delamination (crack) growth. Overall, the problem includes fracture mechanics, 3-D stability analysis and material properties.

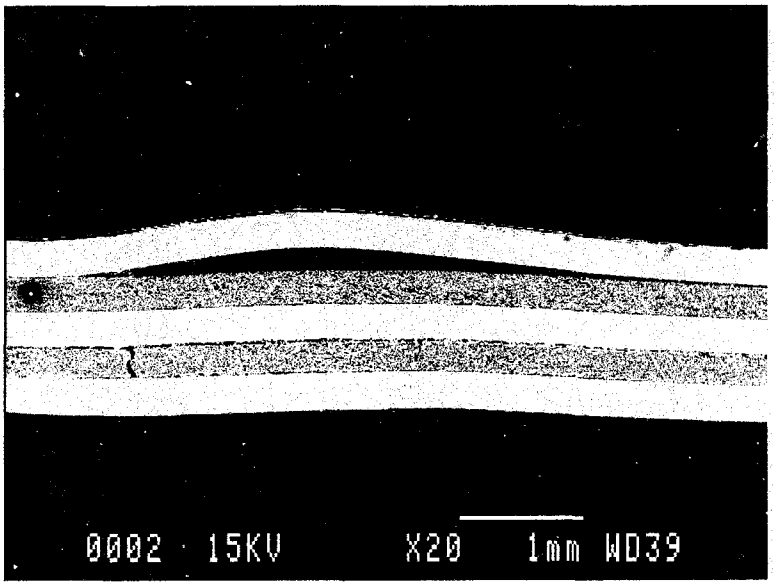


**Fig. 1-5** Buckled cross-section of a delaminated composite material subjected to compressive loading at the ends. [5]

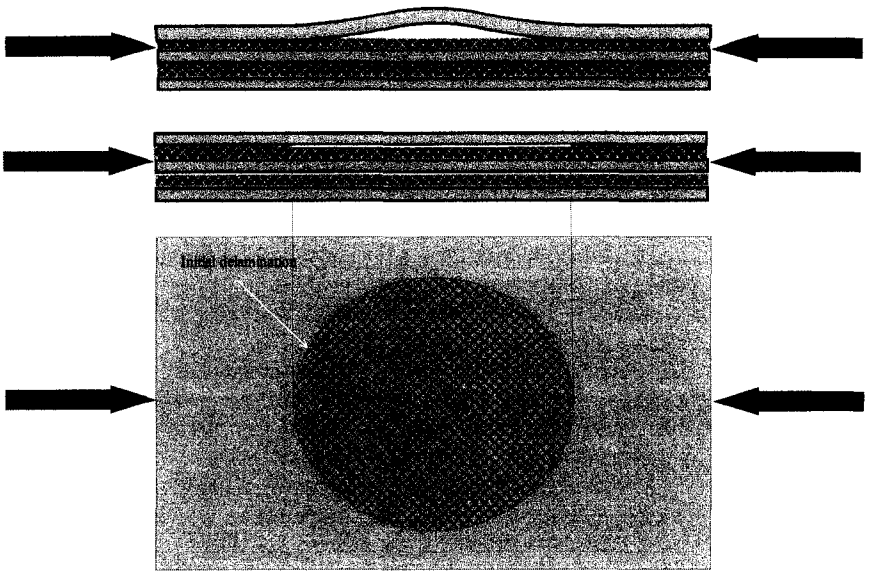


**Fig. 1-6** A circular delamination of a composite material under compressive end loads

Fig. 1-6 schematically depicts a typical circular delamination in a laminated composite material related to what is observed in Fig. 1.5. This type of delamination is caused by an initial manufacturing defect.

### 1.3.3 Blister formation in electronic packages

Buckling/fracture behavior is often observed on the microscopic scale. This example of buckling and fracture occurrence is often classified as blisters. For example, in electronic packaging, thin epoxy coatings are applied to IC packages to protect the package against moisture and corrosion. The coatings are very thin, e.g. 5 microns or less in thickness. If the coating fails, corrosion may occur in the electronic structure of the package and may cause a functional failure of the device.

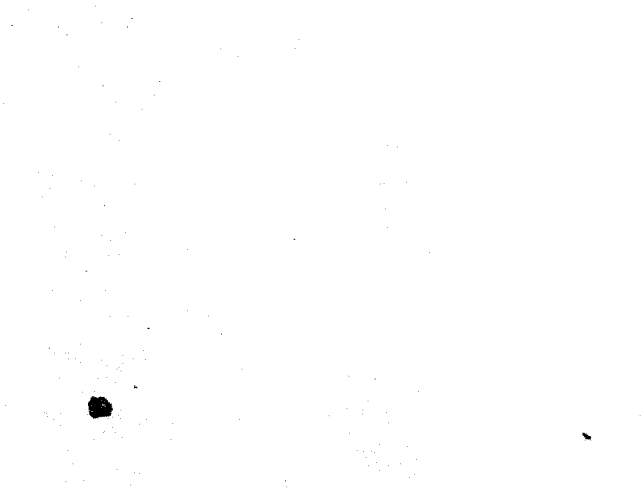

**Fig. 1-7** Blister formations in an electronic package [6, 7]

Fig. 1-8 show images of thin film blister formations [6, 7]. These images are those of test chips which had been used at Lehigh University for statistical analysis of the electrical degradation when the device was subjected to various environmental conditions. The thickness of the thin films covering the chip is 3 to 5 microns. The metallization lines restrict blister growth, but if the blister overcomes this restriction and if the blister is larger in diameter than the distance between the metal lines, water can be trapped between the lines and an electrical short circuit will occur. The Fig. 1.8 shows different blisters that have formed close to, or on top of, electronic circuitery.

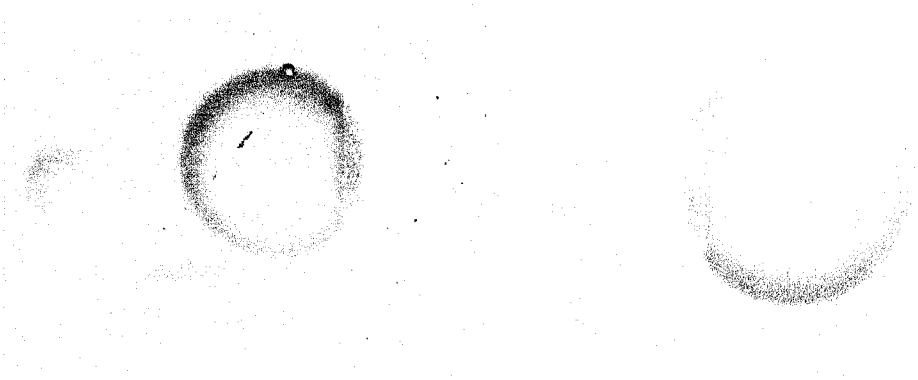

**Fig. 1-8** A blister formation forcing the metallization layers [6, 7]

There are always small defects during the manufacturing process of IC packages. When an epoxy film coating is deposited onto a substrate surface, defects on the substrate surface may prevent the film from bonding properly. For an electronic package that is regularly exposed to severe environmental conditions, e.g., moisture and temperature cycles, these extreme conditions cause the coating to be subjected to

relatively high stresses. Since the coefficient of thermal expansion (CTE) of the coating and substrate are different, temperature change causes different volumetric expansion in the coating and substrate. The film has a much higher CTE than the substrate and when heated, the substrate restricts the film from fully expanding, causing compressive stresses in the film and tension in the substrate. Similarly, cooling will cause the reverse effects in the substrate and film. Moisture diffusion in and out of the film has a very similar effect to thermal loading. The coefficient of hygroscopic expansion (CHE) for the film is higher than that of substrate. When moisture diffuses into the package the film will try to expand more than the substrate. This will introduce compressive stresses in the film and tensile stresses in substrate. The resulting thermal or moisture induced stresses can result in delaminations in weakly bonded regions where substrate defects exist. Besides the thermal and hygroscopic stresses in the coating, moisture can diffuse into the voids which may exist between the film and substrate applying pressure loading to the film. This internal pressure loading may also contribute to the formation of initial delaminations between the film and the substrate.

In spin cast coatings, the coatings are usually in a state of residual tension after cooling to room temperature, because the coating is applied at high temperatures and the cooling film tries to contract more than the substrate. Heating the package and diffusion of moisture into the package, will cause the film to try to expand, with the substrate restricting this expansion. This causes the residual tension in the film to change to compressive stresses.

If the compressive stresses in the delaminated part of the film become large enough, the film covering the delaminated region will buckle away from the substrate. An example of this type of blister formation is shown Fig. 1-7. When the film buckles and a blister is formed, the local stress distribution changes considerably. The buckled state is more prone to additional delamination (crack) growth than it would have been in the unbuckled state. This can be attributed to the out of plane displacement of the film caused by the buckling.

Blister formation is an example of combined fracture and buckling mechanisms. In the design and life prediction of electronic packages with thin film coatings, the fracture behavior of blisters is of considerable importance. The first step in analysis of blisters is to calculate the critical load level and buckling mode [6, 8]. Subsequent postbuckling analysis enables one to trace the driving force for secondary fracture behavior.

## 1.4 Previous work

A large amount of research has been performed to understand the initial buckling behavior of cracked structures. However, postbuckling analysis of cracked structures has received considerably less attention. This can be attributed to the numerical and modeling difficulties associated with this highly nonlinear problem. Analysis of buckling behavior for certain types of cracked structures subjected to compression can be quite complex because of possibility of contact of the crack faces.

This type of crack surface contact problem adds on additional nonlinear behavior that often needs to be considered. Thin cracked structures can undergo localized buckling, without any contact under global tension loads. Early studies on local buckling of plates with a central crack subjected to axial loads go back to the 1960's [9-13]. Studies on this subject focused on thin isotropic plates with an opening or crack. These studies can be mainly classified as analytical, experimental and numerical works.

Beyond a handful of approximate analytical solutions, exact eigen-analysis of structures with cracks or cutouts does not appear to be tractable for even the simplest examples. Cherepanov [9] assumed membrane behavior for the buckled zone and plane stress behavior for the unbuckled zone, in a thin plate with a hole subjected tensile loads. In [9], Cherepanov presented a closed form solution for the displacement contour line of the buckled region. Most research on this subject has focused on developing numerical or experimental methods to identify the critical parameters affecting buckling behavior of thin plates with cracks and openings.

The majority of the experimental work on the buckling of thin plates with cracks, is related to determination of the critical buckling load and corresponding mode shapes under uniaxial [12-15] and biaxial [16] loads. Some approximate formulas were proposed to predict the buckling loads for uniaxial [12] and biaxial [16] loading cases. The effect of parameters, such as plate size and crack aspect ratio, has been investigated for a limited number of the specimens [13]. Petyt [11] investigated static and vibration characteristics of cracked plates subjected uniaxial loads and proposed approximate formulas to find the critical buckling loads. He also considered the nonlinear postbuckling behavior of cracked plates. There are numerous

experimental studies related to buckling and fracture for different types of engineering structures. Blister formation and phone cord type buckling in electronic packages, composite materials with delaminations are common examples of buckling/fracture coupling in different engineering branches[17]. Phone cord buckling is a particularly interesting type blister which forms a periodic buckling pattern [18]

Delamination and buckling analysis of composites is a wide area of investigation in which investigators have mainly focused on planar and axisymmetric analysis [1, 2]. There is a tremendous amount work related to delamination and buckling of composite materials, which makes a complete review of this particular problem beyond the scope of this study. However, it should be noted that the numerical and modeling tools available for three dimensional analysis of buckling/fracture are currently very limited.

# CHAPTER TWO: STRESS DISTRIBUTION AROUND HOLES AND CRACKS IN PLATES

## 2.1 Introduction

Buckling is an important structural failure mode and is associated with a sudden energy release that occurs when the loading reaches a critical value. This critical loading is usually called the critical buckling load and may cause total collapse of the structure without any prior warning. Alternatively, local buckling may or may not cause global failure, depending upon the location, loading conditions, and material properties of the structure. Local buckling is usually due to local compressive stress concentrations. Examples include, a bent pipe under internal pressure and plates with holes.

In this chapter, the stress distribution that results in local buckling of a cracked thin plate will be analyzed. It is well known that, thin cracked plates subjected to tensile forces, have compressive stress concentrations in the neighborhood of the crack. For sufficiently thin plates, remote tensile loads can cause local buckling to develop around the crack [11-13, 16]. In local buckling analysis of thin cracked structures, three-dimensional analysis is desirable because of the true three dimensional nature of the problem, since out of plane displacement occurs during and after buckling. In the following sections, various buckling problems for plates will be analyzed and the compressive stress regions will be examined.

## 2.2 Circular Hole in a thin plate subjected to uniaxial tension

Consider a sufficiently large plate, with a small circular hole with a radius *a,* subjected to uniaxial tensile loading (Fig. 2-1). The solution for the infinite plate with a circular hole can be adopted for the solution of a finite width plate, since the stress distribution becomes almost constant after approximately a distance of 5a from the hole [19]. The solution for a plate with biaxial loading can also be calculated using superposition of the elastic solution. In that case, it is only necessary to substitute the angle ($\pi/2+\theta$) for $\theta$ and superpose the stress values from the original uniaxial solution given in terms of $\theta$.

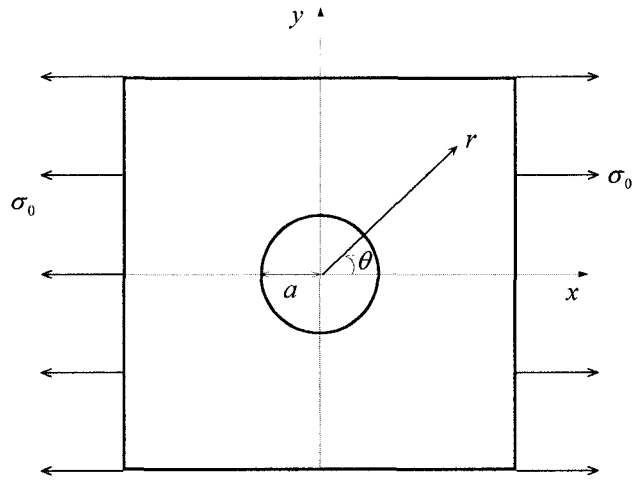


**Fig. 2-1** Plate with circular hole and subjected to uniaxial stress

The internal radial and circumferential stresses are given as [19].

$$\frac{\sigma_r}{\sigma_0} = \frac{1}{2}\left[\left(1-\frac{1}{R^2}\right)+\left(1-\frac{4}{R^2}+\frac{3}{R^4}\right)\cos(2\theta)\right] \tag{2.1}$$

$$\frac{\sigma_\theta}{\sigma_0} = \frac{1}{2}\left[\left(1+\frac{1}{R^2}\right)-\left(1+\frac{3}{R^4}\right)\cos(2\theta)\right] \tag{2.2}$$

$$R = \frac{r}{a} \quad , \quad 1 \le R < \infty \tag{2.3}$$

where, $R$ is the normalized radius. The normalized shear stress is

$$\frac{\sigma_{r\theta}}{\sigma_0} = -\frac{1}{2}\left(1+\frac{2}{R^2}-\frac{3}{R^4}\right)\sin(2\theta) \tag{2.4}$$

The principal stresses can be calculated by using the following equations

$$\frac{\sigma_r+\sigma_\theta}{\sigma_0} = 1-\frac{2}{R^2}\cos(2\theta) \tag{2.5}$$

$$\frac{\sigma_r+\sigma_\theta}{\sigma_0} = -\frac{1}{R^2}+\left(1-\frac{2}{R^2}+\frac{3}{R^4}\right)\cos(2\theta) \tag{2.6}$$

First, the normalized maximum shear stress in polar coordinates can be found from

$$\frac{\tau_{r\theta,\max}}{\sigma_0} = \frac{1}{\sigma_0}\sqrt{\left(\frac{\sigma_r-\sigma_\theta}{2}\right)^2+\sigma_{r\theta}^2} \tag{2.7}$$

The first and second normalized principal stresses are calculated as

$$\frac{\sigma_{1,2}}{\sigma_0} = \frac{1}{\sigma_0}\left(\frac{\sigma_{rr}+\sigma_{\theta\theta}}{2} \pm \sqrt{\left(\frac{\sigma_{rr}+\sigma_{\theta\theta}}{2}\right)^2+\sigma_{r\theta}^2}\right) \tag{2.8}$$

The terms in eq. (2.8) are somewhat cumbersome. However, the first principal stress ratio $(\sigma_1/\sigma_0)$ is a maximum at $(R=1,\theta=\pi/2)$ which is given by $\sigma_{1,\max}=3\sigma_0$. The

first principal stress minimum occurs at $(R=1,\theta=0)$ and has a magnitude of zero. Fig. 2-2 shows the first principal stress contours around the hole.

The second principal stress value, is minimum and compressive at $(R=1,\theta=0)$ and is given by $\sigma_{2,\ min}$=-$\sigma_0$. It is interesting that the first and second principal stresses are minimum at the same location $(R=1,\theta=0)$. Fig. 2-3 shows the normalized second principal $(\sigma_2/\sigma_0)$ stress contours around the circular hole. Since there are some compressive stress regions around the hole, it can be expected that local buckling can occur around the hole for sufficiently thin plates.

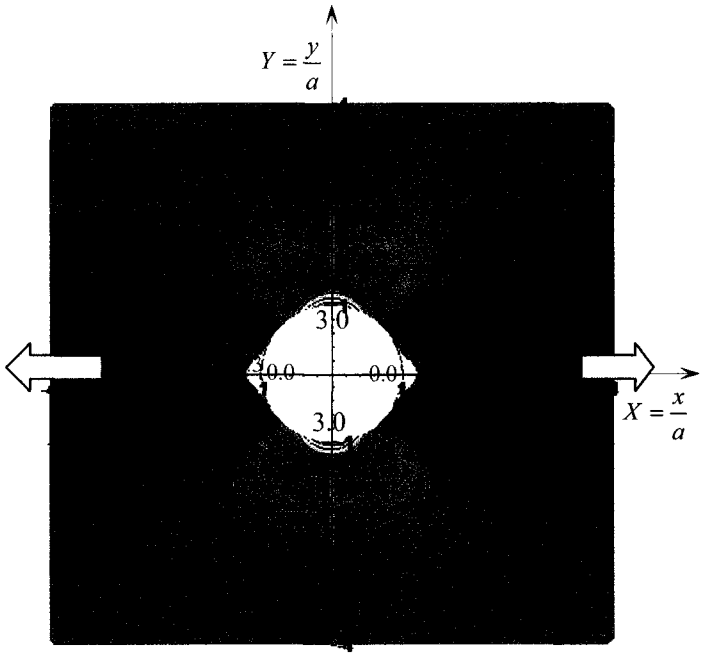


**Fig. 2-2** Normalized the first principal stress $S_1 = \sigma_1/\sigma_0$ contours around the circular hole

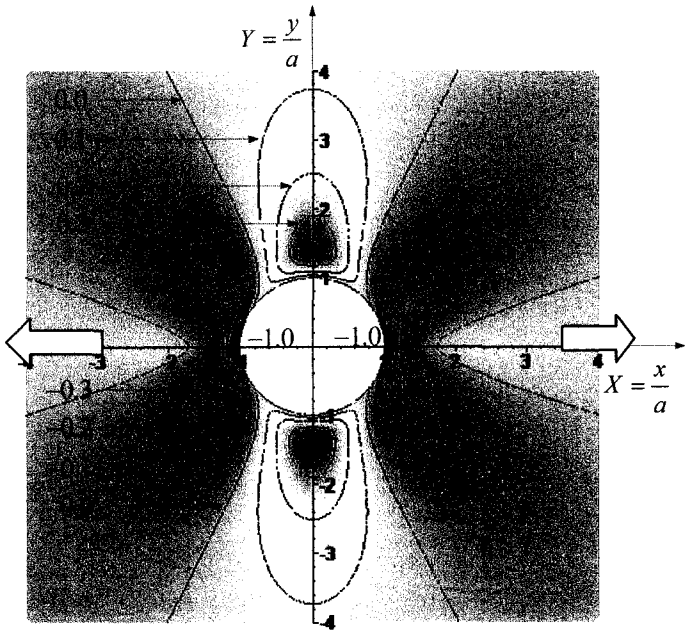


**Fig. 2-3** The normalized 2nd principal stress $S_2 = \sigma_2 / \sigma_0$ contours around circular hole

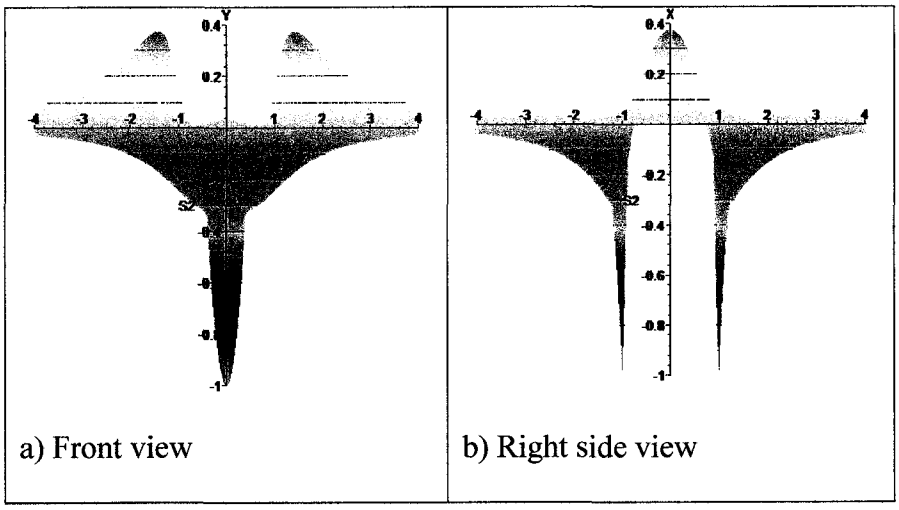


**Fig. 2-4** The normalized second principal stress distributions around the circular hole

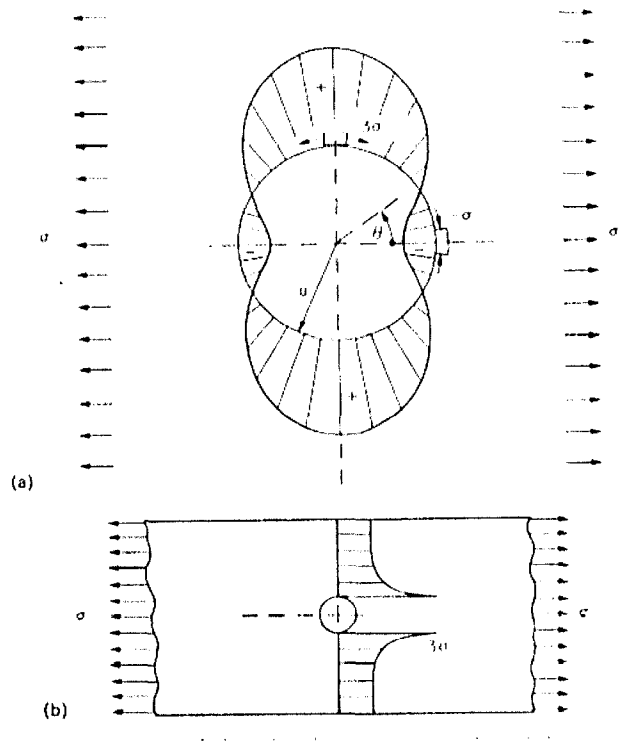


**Fig. 2-5** Distribution of hoop stress component $\sigma_{\theta\theta}$ (a) around the circumference of the circular hole in a large body, and (b) radial distribution along the ligament where $\theta = \pi / 2$

## 2.3 Thin plate with an inclined elliptical hole and subjected to biaxial loading

A model more representative of crack like defects in a plate is a plate with an inclined elliptical hole. Fig. 2-6 shows a homogeneous, isotropic infinite plate subjected to biaxial loading $\sigma$ along $y'$ and $k\sigma$ in the $x'$ direction. This plate has a stress-free elliptical hole and its major axis makes an angle $\beta$ with respect to the $y'$

axis. Taking the limit of some of the geometric variables, permits this model to approximate either a circular hole or a crack. For example, a circular hole can be modeled by taking the semimajor and semiminor axes equal to each other. When the length of the minor axis is approximately zero, a crack can be modeled. In between these two limiting cases, any elliptical hole can be modeled.

As seen in the Fig. 2-7, $a$ and $b$ are lengths of the semi-major and semi-minor axes respectively for the ellipse. $c$ is half of the distance between the foci and the relation between these variables is given by

$$c = \sqrt{a^2 - b^2} \tag{2.9}$$

Note, that for an circle $c = 0$ and for a sharp crack $c = a$.

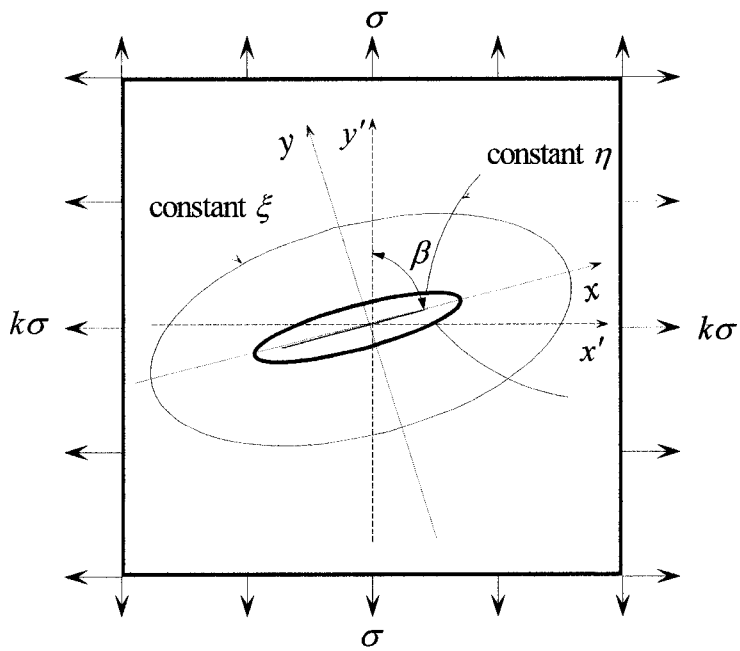


**Fig. 2-6** Geometry of a plate with an inclined elliptical hole subjected to biaxial loading

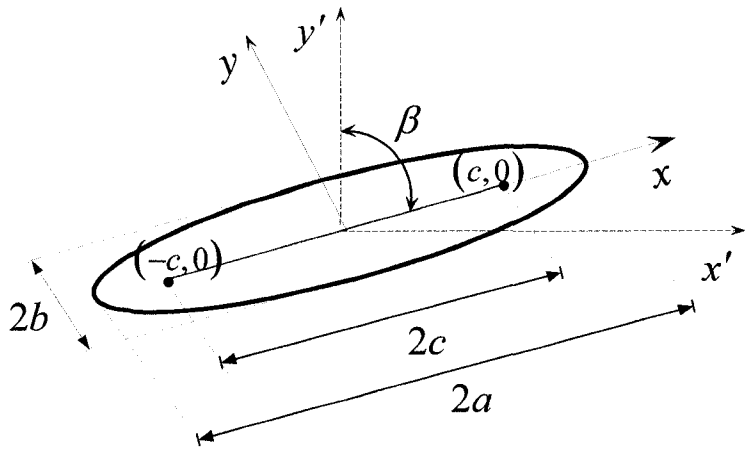


**Fig. 2-7** Geometry of elliptical hole

### 2.3.1 Elliptical coordinates and stresses

Elliptical coordinates are convenient for the solution of this problem. Fig. 2-8, shows the elliptical coordinates, with the coordinate transformation between the elliptical and cartesian coordinates, given by following equations

$$x = c\cosh(\xi)\cos(\eta)$$
$$y = c\sinh(\xi)\sin(\eta) \qquad (2.10)$$

where, $c>0$, $\xi \geq 0$, and $0 \leq \eta \leq 360$. The elliptical hole is defined by $\xi = \xi_0$ and the semi-major and semi-minor axes are $a = c\cosh(\xi_0)$, $b = c\sinh(\xi_0)$ respectively. The ellipse equation in terms of the coordinate $\xi$ becomes

$$\frac{1}{c^2\cosh^2(\xi)}+\frac{1}{c^2\sinh^2(\xi)}=1 \tag{2.11}$$

The summation and difference of the normalized stresses $\sigma_\xi/\sigma_0$ and $\sigma_\eta/\sigma_0$ in terms of elliptical coordinates are given by [20]

$$\frac{\sigma_\xi+\sigma_\eta}{\sigma}=B+\lambda\left(A\sinh(2\xi)-C\sin(2\eta)\right) \tag{2.12}$$

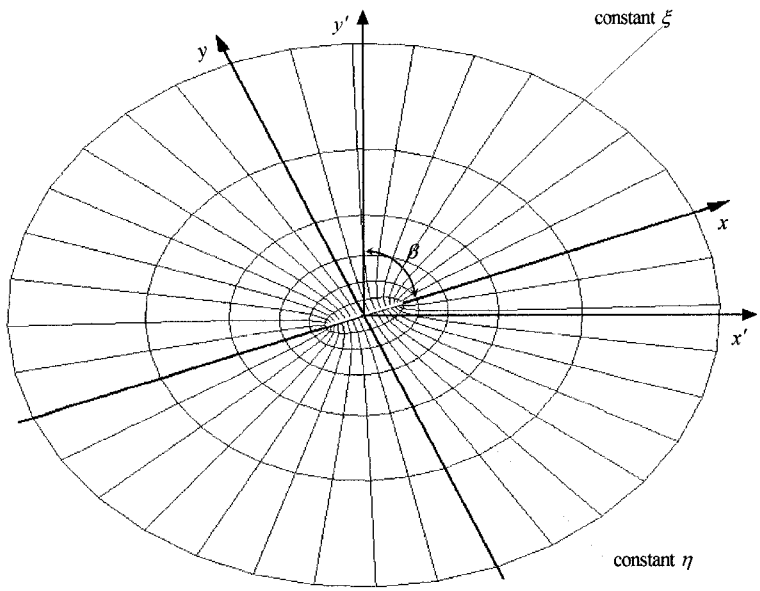


**Fig. 2-8** Elliptical coordinates for the analysis of a plate with an inclined elliptical hole

$$\frac{\sigma_\xi-\sigma_\eta}{\sigma}=-\lambda\left[\cosh\left(2(\xi-\xi_0)\right)-1\right]\left(B\cos(2\eta)+C\sin(2\eta)\right)+$$
$$\lambda\left(\cosh(2\xi_0)-\cos(2\eta)\right)\left[B+\lambda\left(\sinh(2\xi)-C\sin(2\eta)\right)\right] \tag{2.13}$$

The normalized shear stress is

$$\frac{2\tau_{\xi\eta}}{\sigma} = -\left[C + \lambda B \sinh(2\eta)\right]\sinh\left(2(\xi - \xi_0)\right) +$$
$$\lambda C \sinh(2\xi)\left[\cosh\left(2(\xi - \xi_0)\right) - 1\right] +$$
$$\lambda^2\left(\cosh(2\xi) - \cosh(2\xi_0)\right)\left(A\sin(2\eta) + C\sinh(2\xi)\right) \tag{2.14}$$

where, $k$ is the coefficient for the stress component in the transverse direction and $\lambda$ is

$$\lambda = \frac{1}{\cosh(2\xi) - \cos(2\eta)} \tag{2.15}$$

The constants $A$, $B$, and $C$ in equations (2.12), (2.13) and (2.14) are terms which contain the effects of ellipse eccentricity and the inclination angle $\beta$

$$A = m - ne^{2\xi_0}\cos(2\beta), \tag{2.16}$$

$$B = ne^{2\xi_0}\cos(2\beta), \tag{2.17}$$

$$C = ne^{2\xi_0}\sin(2\beta), \tag{2.18}$$

where, $m = 1 + k$, $n = 1 - k$. When $\xi_0 \approx 0$, the ellipse approximates a crack. In the stress calculations for subsequent plots, cracks are approximated by taking a very small semi-minor axis length ($b = 10^{-9}$) and unit length for the semi-major axis ($a = 1$). In this case, the initial elliptic coordinate $\xi_0$ becomes $\xi_0 = \arccos h(a/c) \approx 2.1x10^{-8}$. Based on the relations given above, the first principal stress values are calculated from

$$\sigma_1 = \frac{\sigma_\xi + \sigma_\eta}{2} + \sqrt{\left(\frac{\sigma_\xi - \sigma_\eta}{2}\right)^2 + \tau_{\xi\eta}^2} \tag{2.19}$$

The second principal stress is

$$\sigma_2 = \frac{\sigma_\xi + \sigma_\eta}{2} - \sqrt{\left(\frac{\sigma_\xi - \sigma_\eta}{2}\right)^2 + \tau_{\xi\eta}^2} \tag{2.20}$$

and the maximum shear stress is

$$\tau_{\max} = \sqrt{\left(\frac{\sigma_\xi - \sigma_\eta}{2}\right)^2 + \tau_{\xi\eta}^2} \tag{2.21}$$

The stress in the out of plane (z-direction), for the plane strain case, is

$$\sigma_z = \nu\left(\sigma_\xi + \sigma_\eta\right) \tag{2.22}$$

### 2.3.2 Stress distribution around straight and inclined cracks

Fig. 2-9 shows normalized first principal stress $S_1 = \sigma_1 / \sigma_0$ contours around the crack surface. The normalized stresses are defined as the ratio of the stress to the applied stress. The dark thick contour represents a 1.0 normalized stress contour. This contour divides the stress distribution into two main regions. Inside this contour, the stress contour levels are less than 1.0, and outside the region, they are greater than 1.0. The stress asymptotically approaches zero along the crack's free surfaces.

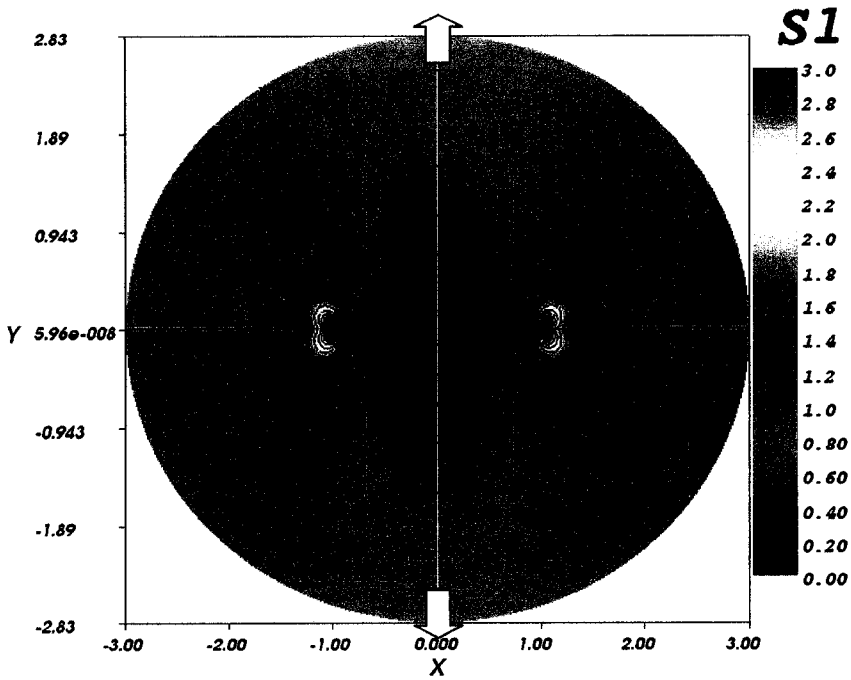


**Fig. 2-9** The normalized first principal stress $S_1 = \sigma_1 / \sigma_0$ contours

The second principal normalized stress $S_2 = \sigma_2 / \sigma_0$ contours are shown in Fig. 2-10. The stresses around the crack's free surface are compressive and rapidly decrease from -1.0 to 0.0 along the Y-axis. When the stress contour levels are divided into compressive and tension zones, a more distinct and qualitative stress distribution can be seen (Fig. 2-11). Gilabert, et.al [14] named this compressive area the "Maltese Cross". This pattern is also common for inclined cracks and holes, but the inclination rotates the cross feature. The regions with blue and red colors in Fig. 2-11 depict the compressive and tension stress zones respectively. The second principal contour level of 0.0 intersects $Y$-axis at $Y = y/a = \mp 0.81$. Although, the compressive zone is continuous, except across the crack's free surface, the tension zone is divided into four

distinct regions and these regions are symmetric with respect to the $X$- and $Y$-axes. Since the crack surface is stress-free, it is evident that the second principal stress parallel to the crack free surface is compressive and perpendicular to the applied stress direction. The thick contour lines represent 0.0 contours of the second principal stress in Fig. 2-10. For completeness, Fig. 2-12 also shows the normalized maximum shear stress ( $S_3 = \tau_{max}/\sigma_0$ ) contours

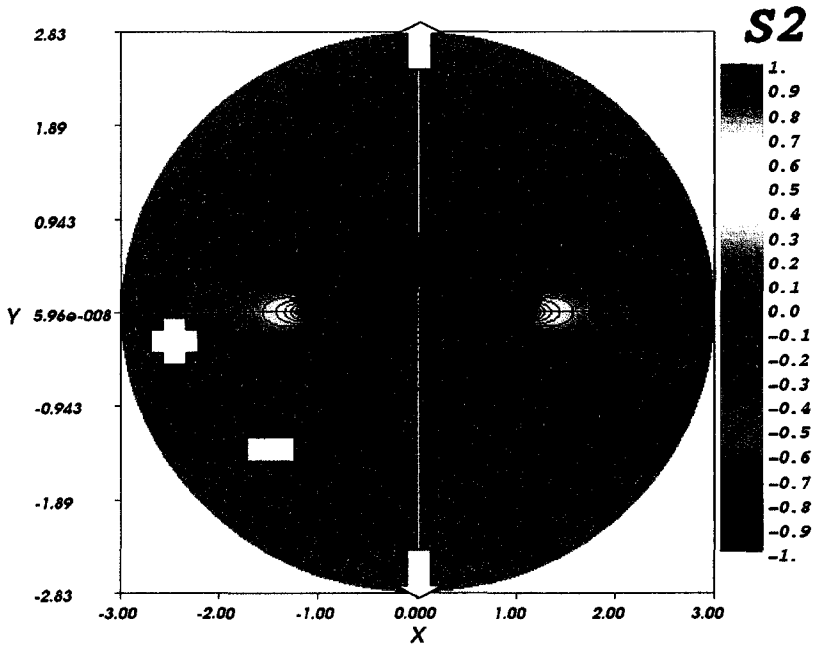


**Fig. 2-10** The normalized second principal stress $S_2 = \sigma_2 / \sigma_0$ contours around the crack

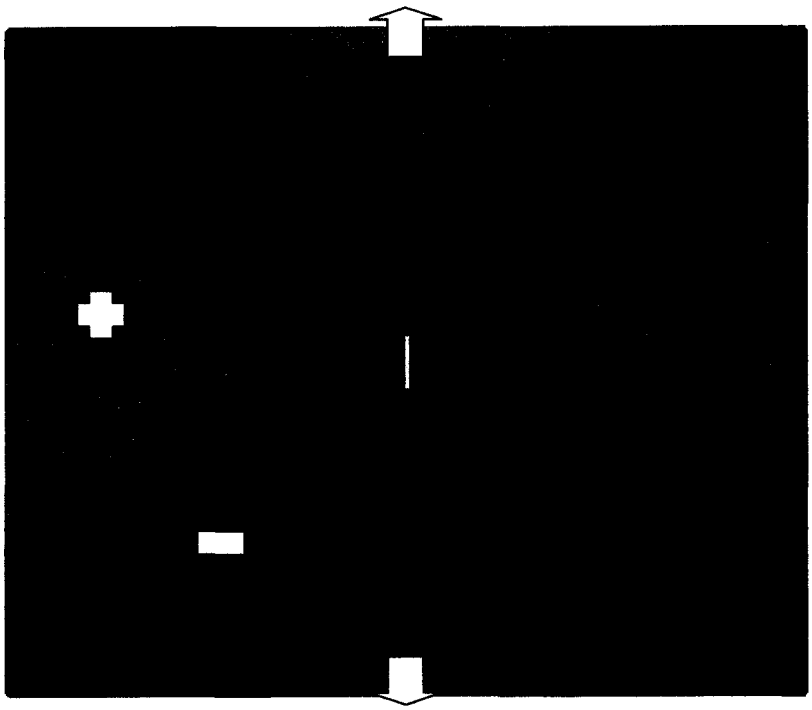

**Fig. 2-11** Distinctive stress regions for the second principal stresses. The blue area is compressive and the red area is in tension

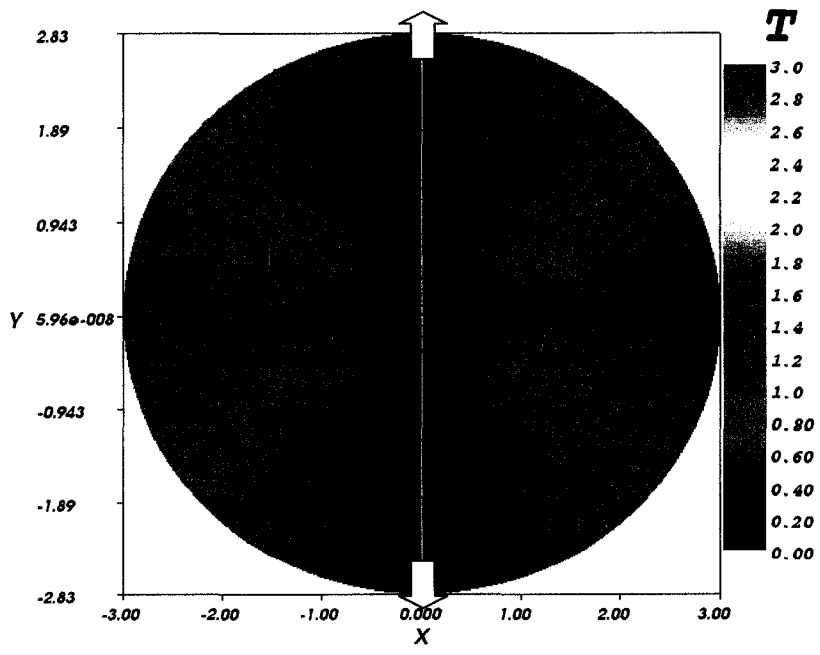


**Fig. 2-12** The normalized maximum shear stress $(\tau_{max}/\sigma_0)$ contours

In the case of an inclined crack, the stress distribution is similar to the previously described behavior, but is inclined with respect to the boundary and somewhat distorted. Anti-symmetry for the inclined crack principal stress contours intensifies more on one half of the crack free surface and less on the other half surface with increasing inclination angle. Because of anti-symmetry in the compressive second principal stress distributions, with respect to the axis along the crack, it can be shown that the inclined crack can also buckle in an anti-symmetric manner. It is also interesting that the crack's free surface around the crack tips shows almost zero second principal stress on one surface and -1.0 on the opposite surface.

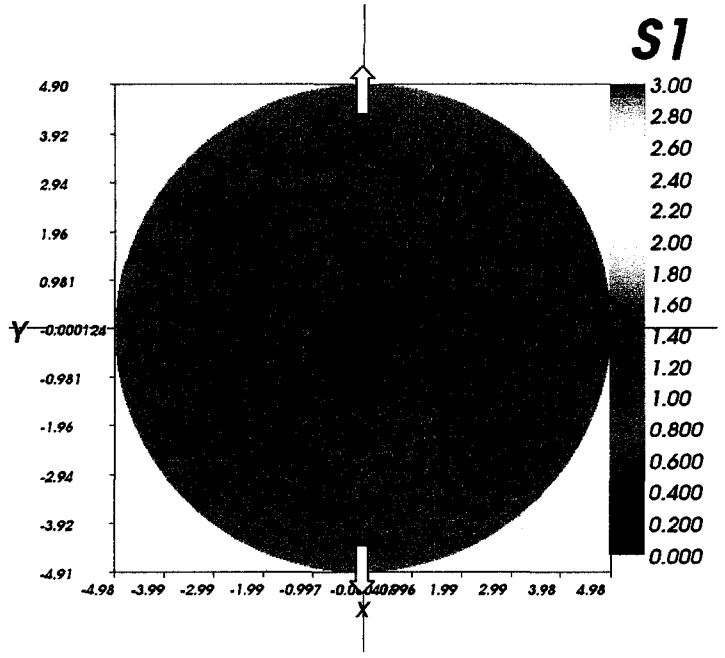


**Fig. 2-13** The normalized first principal stress $S_1 = \sigma_1 / \sigma_0$ contours for an inclined crack $\left(\beta = 70^0\right)$

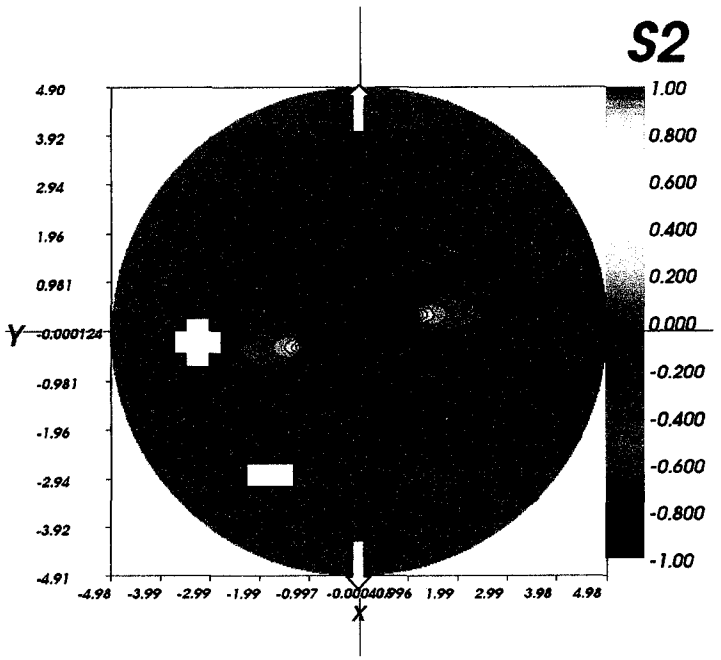


**Fig. 2-14** The normalized second principal stress $S_2 = \sigma_2 / \sigma_0$ contours for an inclined crack $(\beta = 70^o)$

### 2.3.3 Stress distributions around straight and inclined elliptical holes

Elliptic holes show essentially the same behavior as the cracks in terms of the principal stresses, except that there is no crack tip stress singularity at the end of ellipse. Fig. 2-15 and Fig. 2-16 show the first and second normalized principal stress contours for a horizontally aligned central elliptical hole. Similarly, Fig. 2-17 and Fig. 2-18 show the stress contours for an inclined elliptical hole. The dark thick contour lines represents the value of 1.0 and 0.0 for the first and second normalized principal stress contours in Fig. 2-15 respectively. As the eccentricity of the elliptical hole, $e = \sqrt{1-(b/a)^2}$ , increases, the compressive stress distribution spreads over the entire free surface oriented roughly perpendicular to the applied load. Inclination of

the ellipse results in the same behavior as discussed in the previous subsection for a crack.

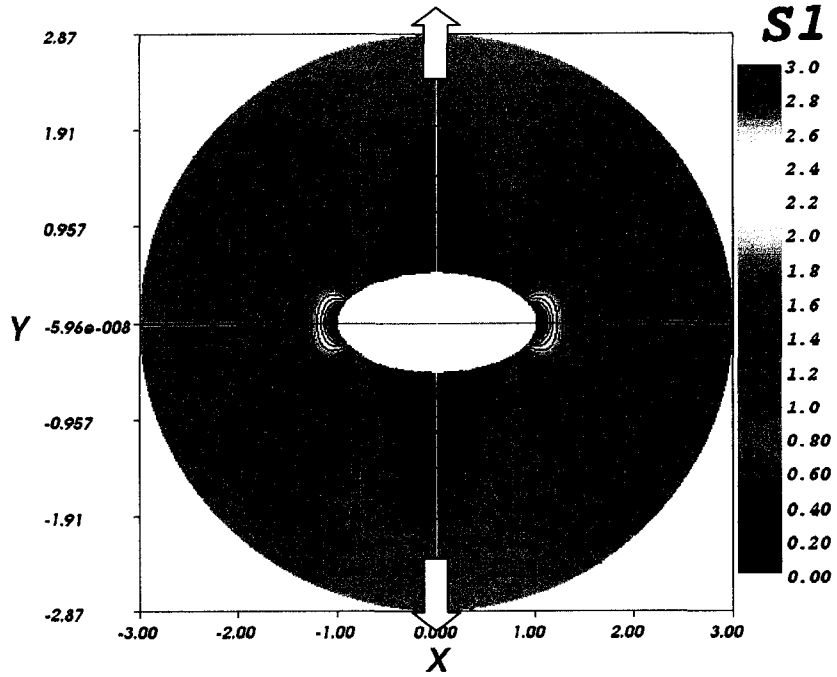


**Fig. 2-15** The normalized first principal stress $S_1 = \sigma_1 / \sigma_0$ contours for an elliptical hole $(a/b = 2)$

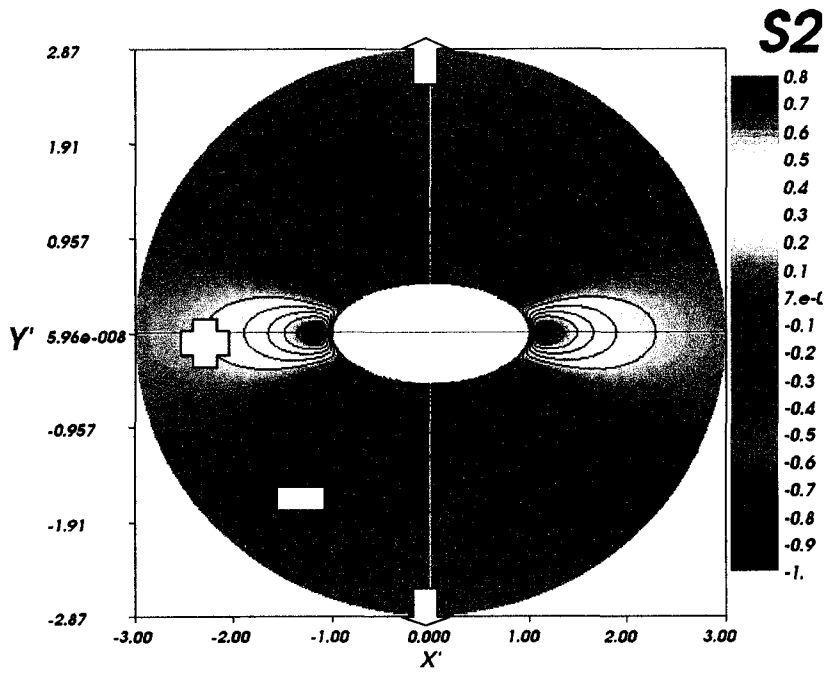


**Fig. 2-16** Second principal stress $S_2 = \sigma_2 / \sigma_0$ contours for an elliptical hole $(a/b = 2)$

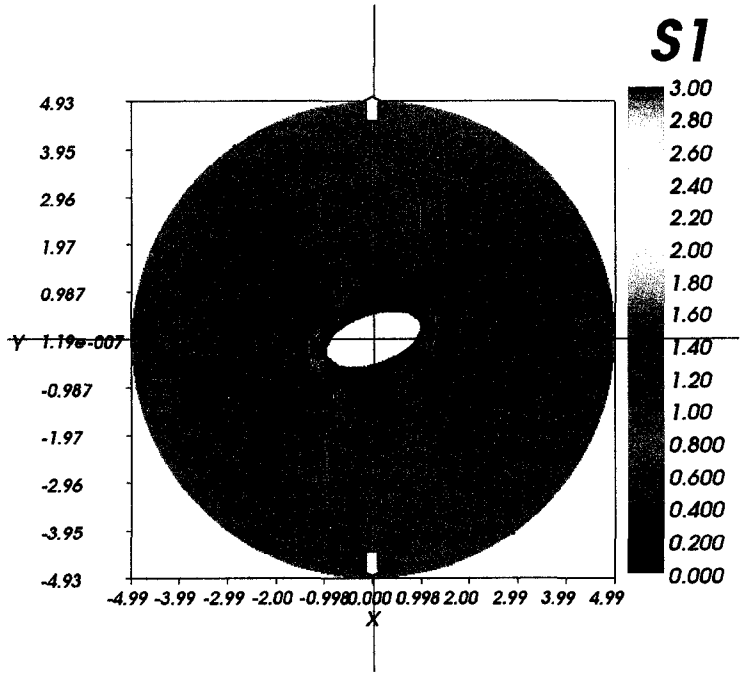


**Fig. 2-17** The normalized first principal stress $S_1 = \sigma_1 / \sigma_0$ contours for an inclined elliptical hole $(a/b = 2, \beta = 70)$

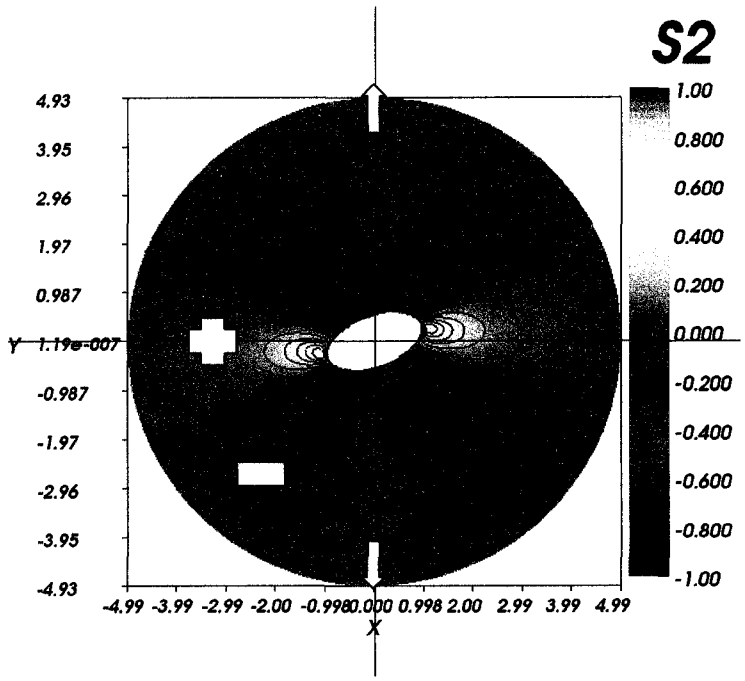


**Fig. 2-18** The normalized second principal stress $S_2 = \sigma_2 / \sigma_0$ contours for an inclined elliptical hole $(a/b = 2, \beta = 70)$

## 2.4 A semi-closed form solution to predict the critical local buckling loads for plates with central cracks

As seen in the figures (Fig. 2-10, Fig. 2-14) that depict the second normalized principal stress distributions, the largest compressive stress zone is parallel to the crack's free surface. The stress contours around the crack surfaces change rapidly in the perpendicular direction. This narrow area with high compressive stresses can be considered as a column strip with uniformly distributed axial compressive loads. Assume that a strip parallel to the crack surface is isolated as a column (Fig. 2.19) and the second principal stress distribution on the crack surface, which is negative of the

applied tensile stress, is applied as a uniformly distributed load. Then, we can derive an approximate critical buckling stress value using Euler column theory.

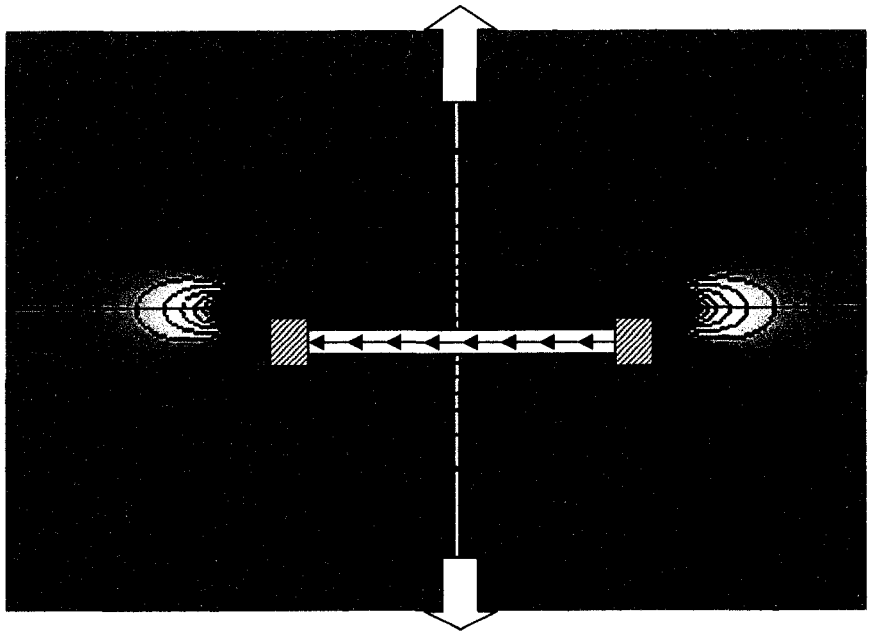

**Fig. 2-19** Column idealization in the neighbourhood of crack's free surface

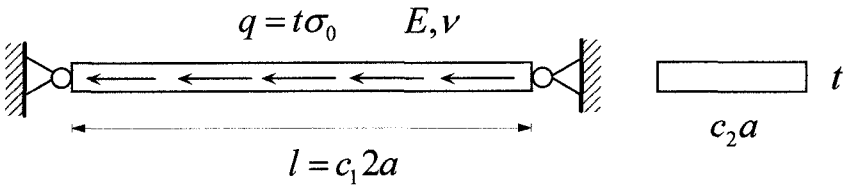


**Fig. 2-20** A fixed-fixed column model with a uniformly distributed axial load

The critical distributed load for a column with a uniformly distributed axial load is given as [21]

$$lq_{cr} = K\frac{\pi^2 EI}{l^2} \tag{2.23}$$

where $K$ is a coefficient which depends on the boundary conditions and the length of the zone subjected to the distributed axial force. The length of the zone carrying the distributed axial load can be taken as the full length of the crack as a first approximation. To assign an effective column length and column width, experimental constants $c_1$ and $c_2$ have to be assigned respectively. Then, the approximate critical buckling stress level can be calculated as follows.

$$I = c_1\frac{at^3}{12}, \quad l = c_2 2a \tag{2.24}$$

where, $I$ is the effective moment of inertia, and $l$ is the effective length

$$tc_1 2a = Kc_2 a\frac{\pi^2 Et^3}{c_1^2 48a^2} \tag{2.25}$$

$$\sigma_{cr} = 0.2K\frac{c_1}{c_2^3}E\left(\frac{t}{a}\right)^2 \tag{2.26}$$

As shown in Fig. 2-19, the length of the idealized column can be taken to lie 0.5-0.8 of the crack length. Similarly, the effective width of the column can be taken as a percentage of the half crack length, e.g. 0.15-0.3$a$. Using these approximations, the approximate equation for the critical condition can be reduced to

$$\sigma_{cr} = cE\left(\frac{t}{a}\right)^2 \tag{2.27}$$

where $c$ is constant that can be determined from experimental observations and/or numerical calculations. It is important to note that because, the idealized column boundary conditions are neither fixed nor pinned, there must be some bending and axial stiffness which should be incorporated into the boundary conditions. Dixon and Strannigan [12] proposed similar approximations to calculate the critical buckling stress.

Dyshel [22] suggested an alternative approximate formula to predict the local buckling load for thin plates. He assumed a semi-infinite plane bounded on one side by the crack's free surface and derived buckling equations using the collocation method. Dyshel's approximate formula is given by

$$\sigma_{cr} = E\frac{\lambda_*(\nu)}{6\left(1-\nu^2\right)}\left(\frac{t}{a}\right)^2 \tag{2.28}$$

where $\lambda_*$ is the smallest eigenvalue obtained using the collocation method, $\nu$ is Poisson's ratio, $t$ is thickness, and $a$ is half crack length. Because of the semi-infinite plate assumption, he concluded that $\lambda_*(\nu)$ is only dependent on Poisson's ratio, and not the geometry of the plate. The term $K$ is the flexure coefficient and is given by

$$K = \frac{\lambda_*(\nu)}{6\left(1-\nu^2\right)} \tag{29}$$

Finally, Dyshel simplified Equation (2.28) for $\nu = 0.3$, yielding

$$\sigma_{cr} = 1.12E\left(\frac{t}{E}\right)^2 \tag{30}$$

For all the crack cases, straight or inclined, there are compressive stress regions where the stresses asymptotically attain a maximum at the free surface of the crack and its magnitude is $-\sigma_o$.

# CHAPTER THREE: NONLINEAR LARGE DEFORMATION OF STRUCTURES

## 3.1 Introduction

Structural instability is an inherently geometric nonlinear problem, due to sudden or rapid change in the structural deformation state. Buckling equations of systems can be derived from classical equilibrium equations obtained from an infinitesimal element and the boundary conditions. Large complex systems require more advanced numerical techniques, such as finite element, boundary element, finite difference methods. For sufficiently stiff structures where the deformation is small until buckling occurs, the eigen-value problem needed to predict the critical load can be reduced to linear form. This assumption is generally reasonable and a common assumption for most post-buckling analyses of structures which exhibit bifurcation type buckling. In bifurcation type buckling, the postbuckling can follow more than one alternative path. For classical bifurcation type of buckling, the buckling is very sudden and it is necessary to predict the critical buckling load in order to predict the post-buckling path correctly. Postbuckling behavior is inherently nonlinear because of the large displacements that occur in the structure. The large deformations that occur after initial buckling, in addition, may or may not cause material nonlinearity, depending on the material properties. Thus, an accurate buckling and postbuckling analysis requires a geometrically nonlinear formulation. In the following sections,

deformation, stress definitions and equilibrium equations for geometrically nonlinear structures will be derived. The derived formulations were implemented into the finite element code (FRAC3D) which will be examined in more detail in the next chapter.

Since the fracture mechanics model assumes asymptotic elastic linear behavior for the crack problems, a special formulation for the analysis of geometrically nonlinear structures with cracks must be considered. The FRAC3D finite element code uses special transition elements to ensure compatibility between the linear elastic enriched crack tip elements and the regular geometrically nonlinear element (see Appendix A). The transition is accomplished by suitably modifying the element interpolation function. A more detailed explanation and formulation of the enriched and transition elements can be found in the references [3], [8].

For statically determinate beams, columns, or plates, the geometric stiffness can be easily calculated. However, for complicated structures, the geometric stiffness is unknown prior to the analysis. So, evaluation of the stress distribution in the structure is the first step for a linearized buckling analysis of a particular structure. In postbuckling analysis the calculation requires pre- and post-buckling phases. There are computational difficulties associated with the transition from the pre-buckled state to the beginning of post-buckled state. To overcome the transition from buckling initiation to the post-buckled state, the buckling mode shapes can be used for numerical perturbation (imperfection) of the system. However, the post-buckling behavior of the imperfect systems deviates slightly from the true path that a perfect system normally would follow. This deviation is highly sensitive to the magnitude of the perturbation and it may be required to perform analyses with perturbations of

different magnitudes to determine sensitivity of the structure to the initial perturbation. Thus, linear buckling analysis not only enables one to predict the initial shape of the buckled configuration, but also can be used to perturbate the structure to overcome computational difficulties related to progressing into the postbuckling analysis of the structure.

## 3.2 Pertinent aspects of nonlinear continuum mechanics

There are two approaches in continuum mechanics to describe motion of the continuum system [23, 24]. Namely, the Lagrangian and Eulerian description. In the Lagrangian description, the coordinates of moving points are defined by a system of coordinates that do not vary with time, in other words, deformed (spatial) coordinates are defined in terms of undeformed (material) coordinates, which are fixed. When the Eulerian description is used, the coordinates of the undeformed coordinates are given in terms of the deformed coordinates. The Eulerian description is commonly used in fluid mechanics. However, in solid mechanics, the Lagrangian description is more commonly used, because of the convenience inherent in tracking the displacement of individual particles. In this numerical treatment, the Lagrangian description will be used.

### 3.2.1 Lagrangian description of deformation

Consider a continuum at time $t = t_0$ in the undeformed state (Fig. 3-1). When a point in the continuum is displaced to a new point at time $t = t$, the position vector a point in the deformed (spatial) configuration is given in terms of undeformed (material) coordinates as $\mathbf{x} = \mathbf{X} + \mathbf{u}$, where

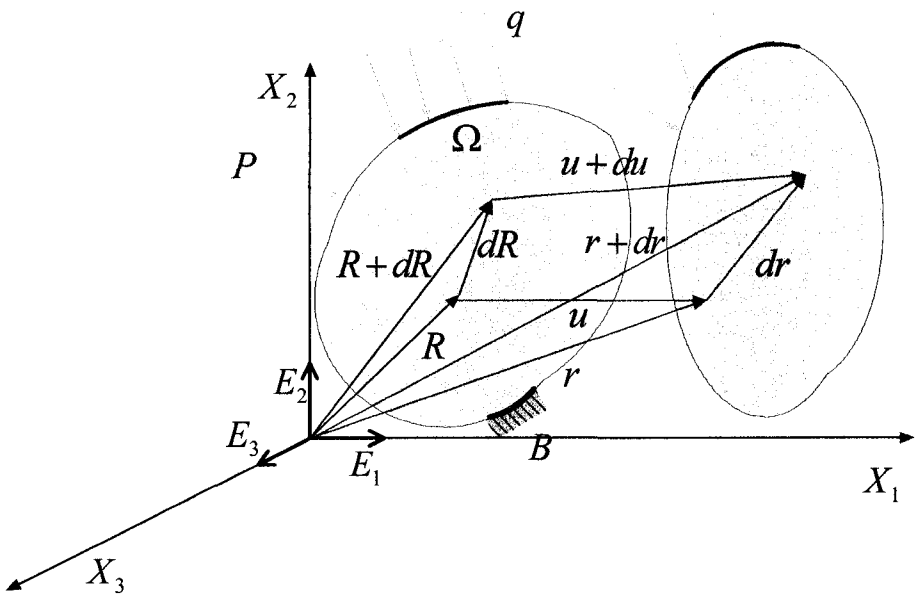


**Fig. 3-1** Deformation geometry in a continuum

$$\underline{\mathbf{x}} = \begin{bmatrix} x_1(X_1,X_2,X_3) \\ x_2(X_1,X_2,X_3) \\ x_3(X_1,X_2,X_3) \end{bmatrix}, \quad \underline{\mathbf{u}} = \begin{bmatrix} u_1(X_1,X_2,X_3) \\ u_2(X_1,X_2,X_3) \\ u_3(X_1,X_2,X_3) \end{bmatrix}, \quad \underline{\mathbf{X}} = \begin{bmatrix} X_1 \\ X_2 \\ X_3 \end{bmatrix} \tag{3.1}$$

Note that the vectors are shown with underlined boldface letters and matrices are shown with boldface letters only. The differential deformed vector is given as

$$d\underline{\mathbf{x}} = \frac{\partial \underline{\mathbf{x}}}{\partial \underline{\mathbf{X}}} d\underline{\mathbf{X}} = \mathbf{F} d\underline{\mathbf{X}} \tag{3.2}$$

where, **F** is the deformation gradient, which is the Jacobian matrix of the deformed coordinates.

$$\mathbf{F} = \frac{\partial \underline{\mathbf{x}}}{\partial \underline{\mathbf{X}}} = \frac{\partial (x_1, x_2, x_3)}{\partial (X_1, X_2, X_3)} = \begin{bmatrix} \frac{\partial x_1}{\partial X_1} & \frac{\partial x_1}{\partial X_2} & \frac{\partial x_1}{\partial X_3} \\ \frac{\partial x_2}{\partial X_1} & \frac{\partial x_2}{\partial X_2} & \frac{\partial x_2}{\partial X_3} \\ \frac{\partial x_3}{\partial X_1} & \frac{\partial x_3}{\partial X_2} & \frac{\partial x_3}{\partial X_3} \end{bmatrix} \tag{3.3}$$

The displacement gradient is given as

$$\mathbf{D} = \frac{\partial \underline{\mathbf{u}}}{\partial \underline{\mathbf{X}}} = \frac{\partial (u_1, u_2, u_3)}{\partial (X_1, X_2, X_3)} = \begin{bmatrix} \frac{\partial u_1}{\partial X_1} & \frac{\partial u_1}{\partial X_2} & \frac{\partial u_1}{\partial X_3} \\ \frac{\partial u_2}{\partial X_1} & \frac{\partial u_2}{\partial X_2} & \frac{\partial u_2}{\partial X_3} \\ \frac{\partial u_3}{\partial X_1} & \frac{\partial u_3}{\partial X_2} & \frac{\partial u_3}{\partial X_3} \end{bmatrix} \tag{3.4}$$

The deformation gradient and displacement gradient can be related as

$$\mathbf{F} = \frac{\partial \underline{\mathbf{x}}}{\partial \underline{\mathbf{X}}} = \left( \frac{\partial \underline{\mathbf{u}}}{\partial \underline{\mathbf{X}}} + \frac{\partial \underline{\mathbf{X}}}{\partial \underline{\mathbf{X}}} \right) = [\mathbf{D} + \mathbf{I}] \tag{3.5}$$

where, **I** is a 3 by 3 unit matrix. For the treatment of the Total Lagrangian description it may be convenient to arrange the displacement gradients as a 9-component vector in finite element calculations, i.e.,

$$\underline{\mathbf{D}}^T = \begin{bmatrix} \frac{\partial u_1}{\partial X_1} & \frac{\partial u_1}{\partial X_2} & \frac{\partial u_1}{\partial X_3} & \frac{\partial u_2}{\partial X_1} & \frac{\partial u_2}{\partial X_2} & \frac{\partial u_2}{\partial X_3} & \frac{\partial u_3}{\partial X_1} & \frac{\partial u_3}{\partial X_2} & \frac{\partial u_3}{\partial X_3} \end{bmatrix} \tag{3.6}$$

### 3.2.2 Finite strain measures

There are mainly four strain measures that are commonly used in computational codes. These are the engineering strain, logarithmic strain, Green-Lagrange strain, and Eulerian (Almansi) strain measures. For the Lagrangian description, the Green-Lagrange strain measure will be used throughout the following sections. Engineering and Green-Lagrangian strain measures (in one dimensional form) are defined respectively by

$$\varepsilon_E = \frac{ds - dS}{dS} \tag{3.7}$$

$$E = \frac{ds^2 - dS^2}{2dS^2} \tag{3.8}$$

where, $ds$ and $dS$ are the final and initial lengths of the line element under consideration respectively. A simple Taylor series analysis shows that for the case where $ds \approx dS$, the Green-Lagrange strain converges to the small strain definition as stated by equation (3.7). This approximation also enables us to use conventional engineering stress-strain constitutive relationships in a nonlinear analysis with small strains but large rotations. The Green-Lagrange strain measure characterizes the deformation in the neighborhood of a point and is given in general form as

$$E = \frac{ds^2 - dS^2}{2dS^2} = \frac{d\underline{\mathbf{x}}^T d\underline{\mathbf{x}} - d\underline{\mathbf{X}}^T d\underline{\mathbf{X}}}{2d\underline{\mathbf{X}}^T d\underline{\mathbf{X}}} \tag{3.9}$$

Its 3-D form in Cartesian coordinates, can be expressed in the term of the difference between the squares of deformed and undeformed differential line elements.

$$d\underline{\mathbf{x}}^T d\underline{\mathbf{x}} - d\underline{\mathbf{X}}^T d\underline{\mathbf{X}} = 2d\underline{\mathbf{X}}^T \mathbf{E} d\underline{\mathbf{X}} \tag{3.10}$$

Or, it can be expressed in terms of the deformation or displacement gradients [25]

$$\mathbf{E} = \begin{bmatrix} E_{11} & E_{12} & E_{13} \\ E_{21} & E_{22} & E_{23} \\ E_{31} & E_{32} & E_{33} \end{bmatrix} = \frac{1}{2}\left[\mathbf{F}^T\mathbf{F} - \mathbf{I}\right] = \frac{1}{2}\left[\mathbf{D} + \mathbf{D}^T\right] + \frac{1}{2}\mathbf{D}^T\mathbf{D} \tag{3.11}$$

The Green-Lagrange strain tensor is symmetric so it can be written in vector form as [25]

$$\underline{\mathbf{E}} = \begin{bmatrix} E_{11} \\ E_{22} \\ E_{33} \\ E_{12} \\ E_{23} \\ E_{13} \end{bmatrix} = \frac{1}{2}\begin{bmatrix} 2\dfrac{\partial u_1}{\partial X_1} \\ 2\dfrac{\partial u_2}{\partial X_2} \\ 2\dfrac{\partial u_3}{\partial X_3} \\ \dfrac{\partial u_1}{\partial X_2} + \dfrac{\partial u_2}{\partial X_1} \\ \dfrac{\partial u_2}{\partial X_3} + \dfrac{\partial u_3}{\partial X_2} \\ \dfrac{\partial u_1}{\partial X_3} + \dfrac{\partial u_3}{\partial X_1} \end{bmatrix} + \frac{1}{2}\begin{bmatrix} \left[\left(\dfrac{\partial u_1}{\partial X_1}\right)^2 + \left(\dfrac{\partial u_1}{\partial X_2}\right)^2 + \left(\dfrac{\partial u_1}{\partial X_3}\right)^2\right] \\ \left[\left(\dfrac{\partial u_2}{\partial X_1}\right)^2 + \left(\dfrac{\partial u_2}{\partial X_2}\right)^2 + \left(\dfrac{\partial u_2}{\partial X_3}\right)^2\right] \\ \left[\left(\dfrac{\partial u_3}{\partial X_1}\right)^2 + \left(\dfrac{\partial u_3}{\partial X_2}\right)^2 + \left(\dfrac{\partial u_3}{\partial X_3}\right)^2\right] \\ \dfrac{\partial u_1}{\partial X_1}\dfrac{\partial u_1}{\partial X_2} + \dfrac{\partial u_2}{\partial X_1}\dfrac{\partial u_2}{\partial X_2} + \dfrac{\partial u_3}{\partial X_1}\dfrac{\partial u_3}{\partial X_2} \\ \dfrac{\partial u_1}{\partial X_2}\dfrac{\partial u_1}{\partial X_3} + \dfrac{\partial u_2}{\partial X_2}\dfrac{\partial u_2}{\partial X_3} + \dfrac{\partial u_3}{\partial X_2}\dfrac{\partial u_3}{\partial X_3} \\ \dfrac{\partial u_1}{\partial X_1}\dfrac{\partial u_1}{\partial X_3} + \dfrac{\partial u_2}{\partial X_1}\dfrac{\partial u_2}{\partial X_3} + \dfrac{\partial u_3}{\partial X_1}\dfrac{\partial u_3}{\partial X_3} \end{bmatrix} \tag{3.12}$$

The strains $E_{11}, E_{22}$, and $E_{33}$ are referred to as the extensional components of the strains and $E_{12}, E_{23}$, and $E_{13}$ are the nonlinear shear strain components.

### 3.2.3 Area and volume change

Relations between infinitesimal undeformed area and corresponding deformed area are given as,

$$d\mathbf{A} = |\mathbf{F}|^{-1}\,\mathbf{F}^{T} d\mathbf{a} \tag{3.13}$$

Inverse of (3.13) gives the deformed area in terms of reference coordinates as

$$d\mathbf{a} = |\mathbf{F}|\mathbf{F}^{-T} d\mathbf{A} \tag{3.14}$$

The relation between undeformed and deformed volumes are given as

$$dV = |\mathbf{F}|^{-1}\, dv \tag{3.15}$$

Similarly, the inverse relation gives the deformed infinitesimal volume as

$$dv = |\mathbf{F}|\, dV \tag{3.16}$$

If an incompressible material is assumed, then, the volume of the undeformed and deformed infinitesimal volume can be derived from the conservation of mass principle as

$$\rho_0 dV = \rho dv \tag{3.17}$$

$$\frac{\rho_0}{\rho} = \frac{dv}{dV} = |\mathbf{F}| \tag{3.18}$$

## 3.3 Stress definitions and their relationship with each other

In this section, several definitions of stresses such as the Cauchy, first Piola-Kirchhoff (FPK), and second Piola-Kirchhoff (SPK) will be described in the Cartesian coordinate frame and their relations with each other will be listed in a tabular form. These stresses are important in the subsequent development of large-displacement and large-deformation formulations.

### 3.3.1 Cauchy stress tensor

Cauchy stress tensor (or the Eulerian stress tensor) $\sigma_{ij}$ is defined as the stress acting on the cubic element of the deformed body and is expressed as the limit of a force on the infinitesimal area,

$$\lim_{da\to 0} \frac{d\underline{\mathbf{P}}}{da} = \boldsymbol{\sigma}\underline{\mathbf{n}} \tag{3.19}$$

The force components is given as

$$dP_j = da\sigma_{ij}n_i \tag{3.20}$$

Physically, eq. (3.19) implies the usual definition of force per unit deformed area. The force components can be written in matrix format as

$$\begin{bmatrix} dP_1 \\ dP_2 \\ dP_3 \end{bmatrix} = da \begin{bmatrix} \sigma_{11} & \sigma_{21} & \sigma_{31} \\ \sigma_{12} & \sigma_{22} & \sigma_{32} \\ \sigma_{13} & \sigma_{23} & \sigma_{33} \end{bmatrix} \begin{bmatrix} n_1 \\ n_2 \\ n_3 \end{bmatrix} \tag{3.21}$$

$$d\underline{\mathbf{a}} = \begin{Bmatrix} da_1 \\ da_2 \\ da_3 \end{Bmatrix} = da \begin{Bmatrix} n_1 \\ n_2 \\ n_3 \end{Bmatrix} \tag{3.22}$$

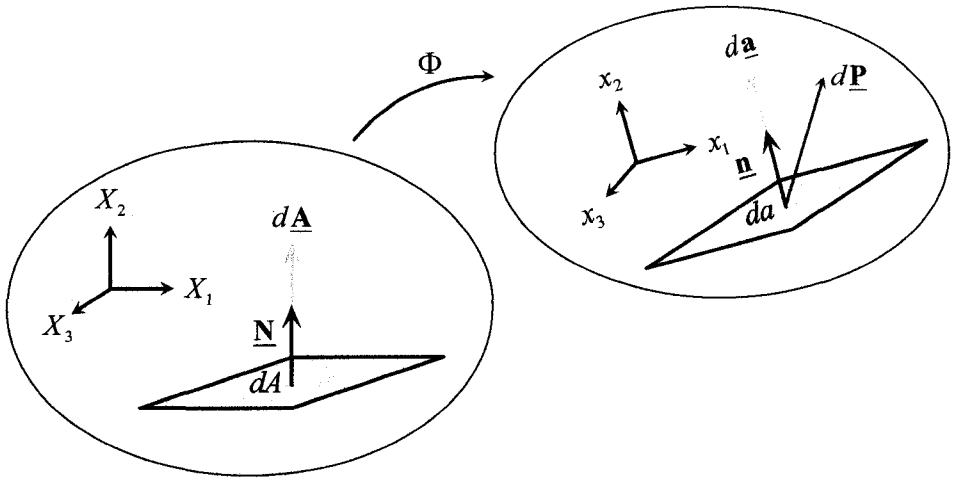


**Fig. 3-2** Area representations in material and spatial coordinates

$$d\underline{\mathbf{P}} = \boldsymbol{\sigma}^T d\underline{\mathbf{a}} \tag{3.23}$$

where $\sigma_{ij}$ are components of a symmetric Cauchy stress tensor ($\sigma_{ij} = \sigma_{ji}$) and $n_j$ are unit vector components in $j$ direction on the cube. Note that the Cauchy stress tensor is symmetric since equilibrium is maintained in the deformed configuration.

$$d\underline{\mathbf{P}} = \boldsymbol{\sigma} d\underline{\mathbf{a}} = |\mathbf{F}| \boldsymbol{\sigma} \mathbf{F}^{-T} d\underline{\mathbf{A}} \tag{3.24}$$

### 3.3.2 First Piola-Kirchhoff stress tensor

The First Piola-Kirchhoff (FPK) tensor is also called the Lagrangian stress tensor $T_{ij}$ and is defined as the force acting on the deformed configuration per unit area of the undeformed body

$$\lim_{dA\to 0}\frac{d\underline{\mathbf{P}}}{dA} = \mathbf{T}^T\underline{\mathbf{N}} \tag{3.25}$$

$$dP_i = T_{ji}dA_j \tag{3.26}$$

$$dA_j = dAN_j \tag{3.27}$$

where, $dA$ is the area on the undeformed (reference) body, $N_j$ is the normal unit vector component in the $j$ direction, and $dP_i$ is the force acting on the area in the deformed body. The force vector, in matrix form, is,

$$d\underline{\mathbf{P}} = \mathbf{T}^T d\underline{\mathbf{A}} \tag{3.28}$$

The FPK stress tensor is non-symmetric and is sometimes called a *pseudo* stress since it is defined with respect to the force per unit area of the undeformed (reference) body [24]. The relationship between the Cauchy and FPK stresses can be obtained by equilibrium conditions and is,

$$d\underline{\mathbf{P}} = \boldsymbol{\sigma}^T d\underline{\mathbf{a}} = d\underline{\mathbf{P}} = \mathbf{T}^T d\underline{\mathbf{A}} = |\mathbf{F}|\boldsymbol{\sigma}^T\mathbf{F}^{-T}d\underline{\mathbf{A}} \tag{3.29}$$

$$\mathbf{T} = |\mathbf{F}|\mathbf{F}^{-1}\boldsymbol{\sigma} \tag{3.30}$$

### 3.3.3 Second Piola-Kirchhoff stress tensor

The Second Piola-Kirchhoff (SPK) stress tensor components $S_{ij}$ are also defined on the deformed surface of a parallelepiped and measured per unit undeformed area [24]. The direction $j$ of $S_{ij}$ acting on the surface element $dA_i$ is identical to the base vector $m_j$ in the deformed state.

$$\lim_{dA\to 0} \frac{\mathbf{F}^{-1} d\underline{\mathbf{P}}}{dA} = \mathbf{S}\underline{\mathbf{N}} \tag{3.31}$$

The base vector $\mathbf{m}$ can be written as

$$\underline{\mathbf{m}} = \mathbf{F}^T \underline{\mathbf{I}} \tag{3.32}$$

where, $\underline{\mathbf{m}}$ is a vector in the deformed state and $\underline{\mathbf{I}}$ is unit base vector in the undeformed state. The force vector in terms of SPK stress and $d\underline{\mathbf{A}}$ is given as

$$d\underline{\mathbf{P}} = \mathbf{F}\mathbf{S}^T d\underline{\mathbf{A}} \tag{3.33}$$

The relationship between the Cauchy and (SPK) stresses can be obtained by equating the force vectors as

$$d\mathbf{P} = \mathbf{F}\mathbf{S}^T d\mathbf{A} = \boldsymbol{\sigma}^T d\mathbf{a} = |\mathbf{F}| \boldsymbol{\sigma}^T \mathbf{F}^{-T} d\mathbf{A} \tag{3.34}$$

The relationship between the Cauchy and SPK stresses are

$$\boldsymbol{\sigma} = |\mathbf{F}|^{-1} \mathbf{F}\mathbf{S}\mathbf{F}^T \tag{3.35}$$

$$\mathbf{S} = |\mathbf{F}| \mathbf{F}^{-1} \boldsymbol{\sigma} \mathbf{F}^{-T} \tag{3.36}$$

The relationship between and FPK and SPK stresses can be obtained using the previous equations

$$d\underline{\mathbf{P}} = \mathbf{T}^T d\underline{\mathbf{A}} = \mathbf{F}\mathbf{S}^T d\underline{\mathbf{A}} \tag{3.37}$$

$$\mathbf{T} = \mathbf{S}\mathbf{F}^T \tag{3.38}$$

$$\mathbf{S} = \mathbf{T}\mathbf{F}^{-T} \tag{3.39}$$

The Table 3-1 shows the relations between the stress definitions as explained previously.

**Table 3-1** The relationships between stress definitions

| Stress | Cauchy | F-P-K | S-P-K |
|---|---|---|---|
| Cauchy | $\boldsymbol{\sigma}$ | $\lvert\mathbf{F}\rvert^{-1}\mathbf{F}\mathbf{T}$ | $\lvert\mathbf{F}\rvert^{-1}\mathbf{F}\mathbf{S}\mathbf{F}^T$ |
| F-P-K | $\lvert\mathbf{F}\rvert\mathbf{F}^{-1}\boldsymbol{\sigma}$ | T | $\mathbf{S}\mathbf{F}^T$ |
| S-P-K | $\lvert\mathbf{F}\rvert\mathbf{F}^{-1}\boldsymbol{\sigma}\mathbf{F}^{-T}$ | $\mathbf{T}\mathbf{F}^{-T}$ | S |

## 3.4 Virtual work equation

Consider a deformed unit area, $da = 1$ and surface traction vector $\underline{\mathbf{T}}$. Virtual work done on the body using the Eulerian description is

$$\delta W_{ext} = \int_a T_i \delta u_i da + \int_v \rho f_i \delta u_i dv \tag{3.40}$$

where, $a$ and $v$ are deformed area and volume respectively. The relationship between

tractions on the surface and the stress components can be expressed using the following relation

$$\underline{\mathbf{T}} = \begin{bmatrix} T_1 \\ T_2 \\ T_3 \end{bmatrix} = \boldsymbol{\sigma}^T \mathbf{n} = \begin{bmatrix} \sigma_{11} & \sigma_{12} & \sigma_{13} \\ \sigma_{21} & \sigma_{22} & \sigma_{23} \\ \sigma_{31} & \sigma_{32} & \sigma_{33} \end{bmatrix}^T \begin{bmatrix} n_1 \\ n_2 \\ n_3 \end{bmatrix} \tag{3.41}$$

In tensor notation

$$T_i = \sigma_{ji} n_j \tag{3.42}$$

$$\delta W_{ext} = \int_a \sigma_{ji} n_j \delta u_i da + \int_v \rho f_i \delta u_i dv \tag{3.43}$$

where $\sigma_{ji}$ is the Cauchy stress tensor, $n_j$ is the components of the direction normal of the area vector, $\rho$ is the mass density in the deformed state, $f_j$ is the body force component . Using the divergence theorem for the virtual work equation, the following equation is obtained.

$$\delta W_{ext} = \int_v \left[ \frac{\partial \sigma_{ji}}{\partial x_j} \delta u_i + \sigma_{ji} \frac{\partial \delta u_i}{\partial x_j} + \rho f_i \delta u_i \right] dv = \int_v \left[ \sigma_{ji} \frac{\partial \delta u_i}{\partial x_j} + \left( \frac{\partial \sigma_{ji}}{\partial x_j} + \rho f_i \right) \delta u_i \right] dv \tag{3.44}$$

Note that the expression in the parentheses is static equilibrium equation, i.e.,

$$\left( \frac{\partial \sigma_{ji}}{\partial x_j} + \rho f_i \right) = 0 \tag{3.45}$$

Thus, the virtual work equation reduces to

$$\delta W_{ext} = \int_V \sigma_{ji} \frac{\partial (\delta u_i)}{\partial x_j} dV = \int_V \sigma_{ji} \left[ \delta \varepsilon_{ij} + \delta \Omega_{ij} \right] dV \tag{3.46}$$

where $\delta \varepsilon_{ij}$ and $\delta \Omega_{ij}$ are virtual strain and virtual rotation respectively.

$$\varepsilon_{ij} = \frac{1}{2}\left[u_{i,j} + u_{j,i}\right] = \frac{1}{2}\left[\frac{\partial u_i}{\partial x_j} + \frac{\partial u_j}{\partial x_i}\right] \tag{3.47}$$

$$\Omega_{ij} = \frac{1}{2}\left[u_{i,j} - u_{j,i}\right] = \frac{1}{2}\left[\frac{\partial u_i}{\partial x_j} - \frac{\partial u_j}{\partial x_i}\right] \tag{3.48}$$

$$\delta\left(\frac{\partial u_i}{\partial x_j}\right) = \delta\varepsilon_{ij} + \delta\Omega_{ij} \tag{3.49}$$

Since $\sigma_{ji}\delta\Omega_{ij} = 0$, then

$$\delta W_{ext} = \int_V \sigma_{ji}\delta\varepsilon_{ij}dV = \int_V \sigma_{ij}\delta\varepsilon_{ij}dV \tag{3.50}$$

The equation (3.50) is virtual work equation in the Eulerian variables. The virtual work equation is valid for any given time t. During the course of loading and deformation, the equilibrium equation at the time ($t + dt$) is

$$\delta W_{ext} = \int_v \sigma_{ij}^{t+dt}\delta\varepsilon_{ij}dv^{t+dt} = R^{t+dt} = \int_a T_i^{t+dt}\delta u_i da^{t+dt} + \int_a \rho^{t+dt} f_i^{t+dt}\delta u_i dv^{t+dt} \tag{3.51}$$

The configuration at ($t + dt$) is not known, but, we know that the equilibrium condition must be satisfied in the deformed state. There are two approaches to solve this equation, these are so called total and updated Lagrangian formulations. In the total Lagrangian formulation, all stresses and deformations refer to the reference configuration at time $t = 0$. However, in the updated Lagrangian formulation, all stresses and deformations refer to the current configuration at time $t$. In the current formulation, the total Lagrangian formulation will be used.

The virtual work equation using variables in the reference (material) coordinate system is can be obtained by rewriting equation(3.40)

$$\delta W_{ext} = \int_{area} T_i \delta u_i da + \int_{volume} \rho F_i \delta u_i dv \tag{3.52}$$

and using the following relations for the displacement vector, traction forces vector, and deformed area, to define the equilibrium equations in material coordinates.

$$\begin{aligned} u_i &= x_i - X_i \\ \delta u_i &= \delta x_i \end{aligned} \tag{3.53}$$

$$T_i da = \sigma_{ji} n_j da = T_{ji} N_j dA \tag{3.54}$$

We assume that body force component does not change during loading.

$$f_i = F_i \tag{3.55}$$

Using the volume relation before and after deformation, i.e.,

$$\rho dv = \rho_0 dV \tag{3.56}$$

and rewriting the virtual work equation in terms of material coordinates we obtain,

$$\delta W_{ext} = \int_A T_{ji} N_j \delta x_i dA + \int_V \rho_0 F_i \delta x_i dV \tag{3.57}$$

Where $T_{ji}$ is Lagrangian (First P-K) stress tensor, and using divergence theorem

$$\delta W_{ext} = \int_{V^0} \left( T_{ji} \frac{\partial(\delta x_i)}{\partial X_j} + \frac{\partial T_{ji}}{\partial X_j} \delta x_i \right) dV + \int_{V^0} \rho_0 F_i \delta x_i dV \tag{3.58}$$

$$\delta W_{ext} = \int_{V^0} \left[ T_{ji} \frac{\partial(\delta x_i)}{\partial X_j} + \left( \rho_0 F_i + \frac{\partial T_{ji}}{\partial X_j} \right) \delta x_i \right] dV \tag{3.59}$$

Note that second term in the last equation is static equilibrium and vanishes, i.e.,

$$\rho_0 F_{0i} + \frac{\partial T_{ji}}{\partial X_j} = 0 \tag{3.60}$$

The virtual work equation then becomes

$$\delta W_{ext} = \int_{V^0} T_{ji} \frac{\partial(\delta x_i)}{\partial X_j} dV = \int_{V^0} T_{ji} \delta\left(\frac{\partial x_i}{\partial X_j}\right) dV \tag{3.61}$$

Using the relation between the FPK and SPK stresses,

$$T_{ji} = S_{jk} \frac{\partial x_i}{\partial X_k} \tag{3.62}$$

and substitution into the virtual work equation yields,

$$\delta W_{ext} = \int_{V^0} T_{ji} \frac{\partial(\delta x_i)}{\partial X_j} dV = \int_{V^0} T_{ji} \delta\left(\frac{\partial x_i}{\partial X_j}\right) dV = \int_{V^0} S_{jk} \frac{\partial x_i}{\partial X_k} \delta\left(\frac{\partial x_i}{\partial X_j}\right) dV \tag{3.63}$$

Expanding the following relation

$$\frac{1}{2}\delta\left(\frac{\partial x_i}{\partial X_k}\frac{\partial x_i}{\partial X_j}\right) = \frac{1}{2}\left[\delta\left(\frac{\partial x_i}{\partial X_k}\right)\frac{\partial x_i}{\partial X_j} + \frac{\partial x_i}{\partial X_k}\delta\left(\frac{\partial x_i}{\partial X_j}\right)\right] = \delta\left(\frac{\partial x_i}{\partial X_k}\right)\frac{\partial x_i}{\partial X_j}$$

(3.64)

and substitution into the virtual work equation gives

$$\delta W_{ext} = \int_{V^0} S_{jk} \frac{\partial x_i}{\partial X_k} \delta\left(\frac{\partial x_i}{\partial X_j}\right) dV = \int_{V^0} S_{jk} \delta\left(\frac{1}{2}\frac{\partial x_i}{\partial X_j}\frac{\partial x_i}{\partial X_k}\right) dV \tag{3.65}$$

Using the Green-Lagrange strain tensor definition

$$E_{kj} = \frac{1}{2}\left[\frac{\partial x_i}{\partial X_k}\frac{\partial x_i}{\partial X_j} - \delta_{kj}\right] \tag{3.66}$$

and taking the variation of it gives

$$\delta E_{kj} = \delta\left[\frac{1}{2}\frac{\partial x_i}{\partial X_k}\frac{\partial x_i}{\partial X_j}\right] = \delta\left(\frac{\partial x_i}{\partial X_k}\right)\frac{\partial x_i}{\partial X_j} \tag{3.67}$$

The final form of the virtual work equation in index notation becomes

$$\delta W_{ext} = \int_V S_{jk}\delta\left(\frac{1}{2}\frac{\partial x_i}{\partial X_k}\frac{\partial x_i}{\partial X_j}\right)dV = \int_V S_{jk}\delta E_{kj}dV = \int_V S_{jk}\delta E_{jk}dV \tag{3.68}$$

Alternatively, in tensor form [25], eqn.(3.68) is

$$\delta W_{ext} = \int_V \mathbf{S} : \delta\mathbf{E}dV = \int_V \mathbf{S} : \delta\mathbf{E}dV \tag{3.69}$$

Note that sign ":" represents the contraction operation, i.e., the sum of multiplication of SPK stress and the corresponding variation of Green-Lagrangian strain.

$$\mathbf{S} : \delta\mathbf{E} = \underline{\mathbf{S}}^T\delta\underline{\mathbf{E}} = \delta\underline{\mathbf{E}}^T\underline{\mathbf{S}} = \begin{bmatrix} S_{11} & S_{22} & S_{33} & S_{12} & S_{23} & S_{13} \end{bmatrix}\begin{bmatrix} \delta E_{11} \\ \delta E_{22} \\ \delta E_{33} \\ \delta E_{12} \\ \delta E_{23} \\ \delta E_{13} \end{bmatrix} \tag{3.70}$$

In summary, the virtual work equation can be expressed in the following forms:

$$\delta W_{ext} = \int_v \sigma_{ij}\delta\varepsilon_{ij}dv = \int_V T_{ji}\delta\left(\frac{\partial x_i}{\partial X_j}\right)dV = \int_V S_{ij}\delta E_{ij}dV \tag{3.71}$$

$$\delta W_{ext} = \int_v \boldsymbol{\sigma} : \delta\boldsymbol{\varepsilon}dv = \int_V \mathbf{S} : \delta\mathbf{E}dV \tag{3.72}$$

$$\delta W_{ext} = \int_v \underline{\boldsymbol{\sigma}}^T\delta\boldsymbol{\varepsilon}dv = \int_V \underline{\mathbf{S}}^T\delta\mathbf{E}dV \tag{3.73}$$

$$\delta W_{ext} = \int_v \delta\underline{\boldsymbol{\varepsilon}}^T\underline{\boldsymbol{\sigma}}dv = \int_V \delta\underline{\mathbf{E}}^T\underline{\mathbf{S}}dV \tag{3.74}$$

where $\underline{\mathbf{S}}$ is SPK stress vector and $\underline{\mathbf{E}}$ is the Lagrangian strain vector

# CHAPTER FOUR: FINITE ELEMENT FORMULATION OF NONLINEAR PROBLEMS

## 4.1 Introduction

In the previous chapter, strain and stress definitions in a geometrically nonlinear continuum were reviewed and the equilibrium equation based on the principle of the virtual work was derived. In this chapter, we will apply the continuum mechanics developed in Chapter 3 to the development of finite element formulations for three dimensional continua. The total Lagrangian method will be used in the formulation. This formulation is appropriate for large rotations and small strains but may also be applied to large elastic strains, such as occur in rubber, if an appropriate hyperelastic material model is used [25]. The method can also be used for elastic-plastic problems with small strains but large rotations. The Green strains and second Piola-Kirchhoff stresses will be used in the method.

In large deformations, the strain-displacement relations are nonlinear and consequently the analysis requires nonlinear solution methods. A Newton-Raphson method for the solution of the nonlinear finite element equations was used for the incremental solution of the nonlinear system of equations.

## 4.2 Green strains and geometric nonlinearity

In isoparametric elements, the coordinate and displacement fields are defined with the same shape functions and can be defined in matrix form as

$$\underline{\mathbf{X}} = \begin{Bmatrix} X_1 \\ X_2 \\ X_3 \end{Bmatrix} = \mathbf{N}\underline{\mathbf{X}}_n \tag{4.1}$$

$$\underline{\mathbf{u}} = \begin{Bmatrix} u_1 \\ u_2 \\ u_3 \end{Bmatrix} = \mathbf{N}\underline{\mathbf{u}}_n \tag{4.2}$$

where **N** is 3x3$n$ matrix containing shape functions and is

$$\mathbf{N} = \begin{bmatrix} N_1 & 0 & 0 & N_2 & 0 & 0 & .. & .. & .. & N_n & 0 & 0 \\ 0 & N_1 & 0 & 0 & N_2 & 0 & .. & .. & .. & 0 & N_n & 0 \\ 0 & 0 & N_1 & 0 & 0 & N_3 & .. & .. & .. & 0 & 0 & N_n \end{bmatrix}_{3X3n} \tag{4.3}$$

and $n$ is the number of nodes in the element. $\underline{\mathbf{X}}$ and $\underline{\mathbf{u}}$ are the coordinate and displacement vectors respectively. $\underline{\mathbf{X}}_n$ is the vector of nodal undeformed (material) coordinates and $\underline{\mathbf{u}}_n$ is nodal displacements vector.

$$\underline{\mathbf{X}}_n = \{X_1 \quad X_2 \quad X_3 \quad X_4 \quad X_5 \quad X_6 \quad .. \quad .. \quad .. \quad X_{3n-2} \quad X_{3n-1} \quad X_{3n}\}^T \tag{4.4}$$

$$\underline{\mathbf{u}}_n = \{U_1 \quad U_2 \quad U_3 \quad U_4 \quad U_5 \quad U_6 \quad .. \quad .. \quad .. \quad U_{3n-2} \quad U_{3n-1} \quad U_{3n}\}^T \tag{4.5}$$

Green-Lagrange strains can be divided into linear and nonlinear parts, i.e.,

$$\underline{\mathbf{E}} = \underline{\mathbf{E}}_L + \underline{\mathbf{E}}_{NL} \tag{4.6}$$

which can be represented in vector form as

$$\underline{\mathbf{E}}_L = \left\{ \frac{\partial u_1}{\partial X_1} \quad \frac{\partial u_2}{\partial X_2} \quad \frac{\partial u_3}{\partial X_3} \quad \frac{\partial u_1}{\partial X_2} + \frac{\partial u_2}{\partial X_1} \quad \frac{\partial u_2}{\partial X_3} + \frac{\partial u_3}{\partial X_2} \quad \frac{\partial u_1}{\partial X_3} + \frac{\partial u_3}{\partial X_1} \right\}^T \tag{4.7}$$

$$\underline{\mathbf{E}}_{NL} = \begin{Bmatrix} \frac{1}{2}\left[ \left(\frac{\partial u_1}{\partial X_1}\right)^2 + \left(\frac{\partial u_1}{\partial X_2}\right)^2 + \left(\frac{\partial u_1}{\partial X_3}\right)^2 \right] \\ \frac{1}{2}\left[ \left(\frac{\partial u_2}{\partial X_1}\right)^2 + \left(\frac{\partial u_2}{\partial X_2}\right)^2 + \left(\frac{\partial u_2}{\partial X_3}\right)^2 \right] \\ \frac{1}{2}\left[ \left(\frac{\partial u_3}{\partial X_1}\right)^2 + \left(\frac{\partial u_3}{\partial X_2}\right)^2 + \left(\frac{\partial u_3}{\partial X_3}\right)^2 \right] \\ \frac{\partial u_1}{\partial X_1}\frac{\partial u_1}{\partial X_2} + \frac{\partial u_2}{\partial X_1}\frac{\partial u_2}{\partial X_2} + \frac{\partial u_3}{\partial X_1}\frac{\partial u_3}{\partial X_2} \\ \frac{\partial u_1}{\partial X_2}\frac{\partial u_1}{\partial X_3} + \frac{\partial u_2}{\partial X_2}\frac{\partial u_2}{\partial X_3} + \frac{\partial u_3}{\partial X_2}\frac{\partial u_3}{\partial X_3} \\ \frac{\partial u_1}{\partial X_1}\frac{\partial u_1}{\partial X_3} + \frac{\partial u_2}{\partial X_1}\frac{\partial u_2}{\partial X_3} + \frac{\partial u_3}{\partial X_1}\frac{\partial u_3}{\partial X_3} \end{Bmatrix} \tag{4.8}$$

We can write the strains in an alternative form

$$\underline{\mathbf{E}} = \underline{\mathbf{E}}_L + \underline{\mathbf{E}}_{NL} = \left[ \mathbf{H} + \frac{1}{2}\mathbf{A}(\theta) \right] \underline{\boldsymbol{\theta}} \tag{4.9}$$

where **H** is a matrix containing ones,

$$\mathbf{H} = \begin{bmatrix} 1 & 0 & 0 & 0 & 0 & 0 & 0 & 0 & 0 \\ 0 & 0 & 0 & 0 & 1 & 0 & 0 & 0 & 0 \\ 0 & 0 & 0 & 0 & 0 & 0 & 0 & 0 & 1 \\ 0 & 1 & 0 & 1 & 0 & 0 & 0 & 0 & 0 \\ 0 & 0 & 0 & 0 & 0 & 1 & 0 & 1 & 0 \\ 0 & 0 & 1 & 0 & 0 & 0 & 1 & 0 & 0 \end{bmatrix}_{6X9} \tag{4.10}$$

and the vector $\boldsymbol{\theta}$ contains derivatives of the displacement vector components related to the nodal displacements by

$$\underline{\boldsymbol{\theta}} = \mathbf{G}\underline{\mathbf{u}}_n \tag{4.11}$$

where

$$\underline{\boldsymbol{\theta}} = \left\{ \frac{\partial u_1}{\partial X_1} \quad \frac{\partial u_1}{\partial X_2} \quad \frac{\partial u_1}{\partial X_3} \quad \frac{\partial u_2}{\partial X_1} \quad \frac{\partial u_2}{\partial X_2} \quad \frac{\partial u_2}{\partial X_3} \quad \frac{\partial u_3}{\partial X_1} \quad \frac{\partial u_3}{\partial X_2} \quad \frac{\partial u_3}{\partial X_3} \right\}^T \tag{4.12}$$

and

$$\mathbf{G} = \begin{bmatrix} \frac{\partial N_1}{\partial X_1} & 0 & 0 & \frac{\partial N_2}{\partial X_1} & 0 & 0 & .. & .. & \frac{\partial N_n}{\partial X_1} & 0 & 0 \\ \frac{\partial N_1}{\partial X_2} & 0 & 0 & \frac{\partial N_2}{\partial X_2} & 0 & 0 & .. & .. & \frac{\partial N_n}{\partial X_2} & 0 & 0 \\ \frac{\partial N_1}{\partial X_3} & 0 & 0 & \frac{\partial N_2}{\partial X_3} & 0 & 0 & .. & .. & \frac{\partial N_n}{\partial X_3} & 0 & 0 \\ 0 & \frac{\partial N_1}{\partial X_1} & 0 & 0 & \frac{\partial N_2}{\partial X_1} & 0 & .. & .. & 0 & \frac{\partial N_n}{\partial X_1} & 0 \\ 0 & \frac{\partial N_1}{\partial X_2} & 0 & 0 & \frac{\partial N_2}{\partial X_2} & 0 & .. & .. & 0 & \frac{\partial N_n}{\partial X_2} & 0 \\ 0 & \frac{\partial N_1}{\partial X_3} & 0 & 0 & \frac{\partial N_2}{\partial X_3} & 0 & .. & .. & 0 & \frac{\partial N_n}{\partial X_3} & 0 \\ 0 & 0 & \frac{\partial N_1}{\partial X_1} & 0 & 0 & \frac{\partial N_2}{\partial X_1} & .. & .. & 0 & 0 & \frac{\partial N_n}{\partial X_1} \\ 0 & 0 & \frac{\partial N_1}{\partial X_2} & 0 & 0 & \frac{\partial N_2}{\partial X_2} & .. & .. & 0 & 0 & \frac{\partial N_n}{\partial X_2} \\ 0 & 0 & \frac{\partial N_1}{\partial X_3} & 0 & 0 & \frac{\partial N_2}{\partial X_3} & .. & .. & 0 & 0 & \frac{\partial N_n}{\partial X_3} \end{bmatrix}_{9X3n} \tag{4.13}$$

The matrix $\mathbf{A}(\underline{\boldsymbol{\theta}})$ is a nonlinear function of displacements and given by

$$\mathbf{A}(\underline{\boldsymbol{\theta}}) = \begin{bmatrix} \frac{\partial u_1}{\partial X_1} & 0 & 0 & \frac{\partial u_2}{\partial X_1} & 0 & 0 & \frac{\partial u_3}{\partial X_1} & 0 & 0 \\ 0 & \frac{\partial u_1}{\partial X_2} & 0 & 0 & \frac{\partial u_2}{\partial X_2} & 0 & 0 & \frac{\partial u_2}{\partial X_2} & 0 \\ 0 & 0 & \frac{\partial u_1}{\partial X_3} & 0 & 0 & \frac{\partial u_2}{\partial X_3} & 0 & 0 & \frac{\partial u_3}{\partial X_3} \\ \frac{\partial u_1}{\partial X_2} & \frac{\partial u_1}{\partial X_1} & 0 & \frac{\partial u_2}{\partial X_2} & \frac{\partial u_2}{\partial X_1} & 0 & \frac{\partial u_3}{\partial X_2} & \frac{\partial u_3}{\partial X_1} & 0 \\ 0 & \frac{\partial u_1}{\partial X_3} & \frac{\partial u_1}{\partial X_2} & 0 & \frac{\partial u_2}{\partial X_3} & \frac{\partial u_2}{\partial X_2} & 0 & \frac{\partial u_3}{\partial X_3} & \frac{\partial u_3}{\partial X_2} \\ \frac{\partial u_1}{\partial X_3} & 0 & \frac{\partial u_1}{\partial X_1} & \frac{\partial u_2}{\partial X_3} & 0 & \frac{\partial u_2}{\partial X_1} & \frac{\partial u_3}{\partial X_3} & 0 & \frac{\partial u_3}{\partial X_1} \end{bmatrix}_{6X9} \tag{4.14}$$

Green-Lagrange strain in terms of **H** and **A** becomes

$$\underline{\mathbf{E}} = \underline{\mathbf{E}}_L + \underline{\mathbf{E}}_{NL} = \left[\mathbf{H} + \frac{1}{2}\mathbf{A}(\underline{\boldsymbol{\theta}})\right]\mathbf{G}\underline{\mathbf{u}}_n = \left[\mathbf{HG} + \frac{1}{2}\mathbf{A}(\underline{\boldsymbol{\theta}})\mathbf{G}\right]\underline{\mathbf{u}}_n \tag{4.15}$$

The linear and nonlinear parts can be defined in terms of the linear and nonlinear **B** matrices as

$$\underline{\mathbf{E}}_L = \mathbf{HG}\underline{\mathbf{u}}_n = \mathbf{B}_L\underline{\mathbf{u}}_n \tag{4.16}$$

$$\underline{\mathbf{E}}_{NL} = \frac{1}{2}\mathbf{A}(\underline{\boldsymbol{\theta}})\mathbf{G}\underline{\mathbf{u}}_n = \frac{1}{2}\mathbf{B}_{NL}\underline{\mathbf{u}}_n \tag{4.17}$$

$$\mathbf{B}_{NL} = \mathbf{A}(\underline{\boldsymbol{\theta}})\mathbf{G} \tag{4.18}$$

$$\underline{\mathbf{E}} = \underline{\mathbf{E}}_L + \underline{\mathbf{E}}_{NL} = \left[\mathbf{B}_L + \frac{1}{2}\mathbf{B}_{NL}\right]\underline{\mathbf{u}}_n \tag{4.19}$$

The variation of the Green-Lagrange strains is given as

$$\delta\mathbf{E} = \mathbf{B}_L\delta\underline{\mathbf{u}} + \delta\left(\frac{1}{2}\mathbf{A}(\underline{\boldsymbol{\theta}})\underline{\boldsymbol{\theta}}\right) = \mathbf{B}_L\delta\underline{\mathbf{u}} + \mathbf{A}(\underline{\boldsymbol{\theta}})\mathbf{G}\delta\underline{\mathbf{u}} = \mathbf{B}_L\delta\underline{\mathbf{u}} + \mathbf{B}_{NL}\delta\underline{\mathbf{u}} \tag{4.20}$$

Substituting the variational form of the Green-Lagrange strains into the virtual work equations (3.74) gives

$$\delta W_{ext} = \int_V \delta \mathbf{E}^T \underline{\mathbf{S}} dV \tag{4.21}$$

$$\delta W_{ext} = \delta \underline{\mathbf{u}}^T \int_V [\mathbf{B}_L + \mathbf{B}_{NL}] \underline{\mathbf{S}} dV \tag{4.22}$$

where, $\underline{\mathbf{S}}$ is the second Piola-Kirchhoff (SPK) stress vector

$$\underline{\mathbf{S}} = \{S_{11}, S_{22}, S_{33}, S_{12}, S_{23}, S_{13}\}^T \tag{4.23}$$

The constitutive relationship between the SPK stress and Green-Lagrange strain can be expressed as

$$\underline{\mathbf{S}} = \mathbf{C}\underline{\mathbf{E}} \tag{4.24}$$

where, $\mathbf{C}$ is the elasticity matrix for isotropic material given by

$$\mathbf{C} = \frac{E}{(1+\nu)(1-2\nu)} \begin{bmatrix} (1-\nu) & \nu & \nu & 0 & 0 & 0 \\ \nu & (1-\nu) & \nu & 0 & 0 & 0 \\ \nu & \nu & (1-\nu) & 0 & 0 & 0 \\ 0 & 0 & 0 & \frac{1}{2}(1-2\nu) & 0 & 0 \\ 0 & 0 & 0 & 0 & \frac{1}{2}(1-2\nu) & 0 \\ 0 & 0 & 0 & 0 & 0 & \frac{1}{2}(1-2\nu) \end{bmatrix} \tag{4.25}$$

After the elimination of $\delta \mathbf{u}^T$ from the virtual work equation, the final form of the virtual work equation in matrix from is reduced to an equilibrium equation,

$$\int_V \mathbf{B}^T \underline{\mathbf{S}} dV + \underline{\mathbf{f}} = \underline{\mathbf{0}} \tag{4.26}$$

The integral term in (4.26) represents the internal force vector and the second term represents the external force vector. The internal force vector depends on the deformation, which is unknown. If the external force vector also depends on the deformation then, the equilibrium equation includes additional nonlinear terms. For example, an external follower force depends on the deformation. The Newton-Raphson method is widely used for the solution of nonlinear finite element equations. In the following subsection, this method will be examined.

## 4.3 Newton-Raphson method for solution of nonlinear equations in finite flement method

The governing equilibrium equation representing the internal and external forces equilibrium is given by

$$\underline{\Psi}(\underline{\mathbf{u}}_n) = \int_V \left[\mathbf{B}_L^T + \mathbf{B}_{NL}^T\right] \underline{\mathbf{S}} dV + \underline{\mathbf{f}} = \underline{\mathbf{0}} \tag{4.27}$$

where, $\underline{\Psi}(\underline{\mathbf{u}}_n)$ represents the sum of internal and external generalized forces. The matrices $\mathbf{B}_L$ and $\mathbf{B}_{NL}$ represent linear and nonlinear parts of the strain coefficient matrices respectively. It is clear that equation (4.27) must be solved iteratively. If the Newton Newton-Raphson method is adopted, we have to find the relationship between $d\underline{\Psi}(\underline{\mathbf{u}}_n)$ and $d\underline{\mathbf{u}}_n$. Thus, taking appropriate variations of the equation (4.27) with respect to $d\underline{\mathbf{u}}_n$ we obtain

$$d\underline{\Psi}(\underline{\mathbf{u}}_n) = \int_V d\mathbf{B}_{NL}^T \underline{\mathbf{S}} dV + \int_V \mathbf{B}^T d\underline{\mathbf{S}} dV = \mathbf{K}_T d\underline{\mathbf{u}}_n \tag{4.28}$$

If only geometric nonlinearity is considered and material nonlinearity is omitted, then the second integral term in equation (4.28) becomes

$$\int_V \mathbf{B}^T d\underline{\mathbf{S}} dV = \int_V \mathbf{B}^T \mathbf{C}\mathbf{B} dV = \mathbf{K}_L + \mathbf{K}_{NL} \tag{4.29}$$

Note, that in the equation(4.29), the differential of the **S** matrix can be written as

$$d\mathbf{S} = \mathbf{C}d\mathbf{E} = \mathbf{C}\mathbf{B}d\mathbf{a} \tag{4.30}$$

The linear stiffness matrix $\mathbf{K}_L$ and the large displacement matrix $\mathbf{K}_{NL}$ are given as

$$\mathbf{K}_L = \int_V \mathbf{B}_L^T \mathbf{C}\mathbf{B} dV \tag{4.31}$$

$$\mathbf{K}_{NL} = \int_V \mathbf{B}_L^T \mathbf{C}\mathbf{B}_{NL} dV + \int_V \mathbf{B}_{NL}^T \mathbf{C}\mathbf{B}_{NL} dV + \int_V \mathbf{B}_{NL}^T \mathbf{C}\mathbf{B}_L dV \tag{4.32}$$

The differential of the nonlinear matrix $\mathbf{B}_{NL}$ can be written as

$$d\mathbf{B}_{NL} = d\mathbf{A}(\underline{\boldsymbol{\theta}})\mathbf{G} \tag{4.33}$$

$$\int_V d\mathbf{B}_{NL}^T \underline{\mathbf{S}} dV = \int_V \mathbf{G}^T d\mathbf{A}^T \underline{\mathbf{S}} dV \tag{4.34}$$

The matrix multiplication $d\mathbf{A}^T \underline{\mathbf{S}}$ is given by

$$d\mathbf{A}^T \underline{\mathbf{S}} = \begin{bmatrix} \mathbf{S} & \mathbf{0} & \mathbf{0} \\ \mathbf{0} & \mathbf{S} & \mathbf{0} \\ \mathbf{0} & \mathbf{0} & \mathbf{S} \end{bmatrix} d\underline{\boldsymbol{\theta}} \tag{4.35}$$

where the **S** matrix is the 3x3 second Piola-Kirchhoff stress matrix

$$\mathbf{S} = \begin{bmatrix} S_{11} & S_{12} & S_{13} \\ S_{12} & S_{22} & S_{23} \\ S_{13} & S_{23} & S_{33} \end{bmatrix} \tag{4.36}$$

Simplifying eqn. (4.35),

$$d\mathbf{A}^T \underline{\mathbf{S}} = \begin{bmatrix} \mathbf{S} & \mathbf{0} & \mathbf{0} \\ \mathbf{0} & \mathbf{S} & \mathbf{0} \\ \mathbf{0} & \mathbf{0} & \mathbf{S} \end{bmatrix} d\underline{\boldsymbol{\theta}} = \begin{bmatrix} \mathbf{S} & \mathbf{0} & \mathbf{0} \\ \mathbf{0} & \mathbf{S} & \mathbf{0} \\ \mathbf{0} & \mathbf{0} & \mathbf{S} \end{bmatrix} \mathbf{G} d\underline{\mathbf{u}}_n \tag{4.37}$$

Finally, after making all the necessary substitutions, we obtain

$$\int_V d\mathbf{B}_{NL}^T \underline{\mathbf{S}} dV = \int_V \mathbf{G}^T d\mathbf{A}^T \underline{\mathbf{S}} dV = \int_V \mathbf{G}^T \begin{bmatrix} \mathbf{S} & \mathbf{0} & \mathbf{0} \\ \mathbf{0} & \mathbf{S} & \mathbf{0} \\ \mathbf{0} & \mathbf{0} & \mathbf{S} \end{bmatrix} \mathbf{G} dV = \mathbf{K}_\sigma d\underline{\mathbf{u}}_n \tag{4.38}$$

The geometric stiffness matrix $\mathbf{K}_\sigma$ is given by

$$\mathbf{K}_\sigma = \int_V \mathbf{G}^T \begin{bmatrix} \mathbf{S} & \mathbf{0} & \mathbf{0} \\ \mathbf{0} & \mathbf{S} & \mathbf{0} \\ \mathbf{0} & \mathbf{0} & \mathbf{S} \end{bmatrix} \mathbf{G} dV \tag{4.39}$$

The final form of the Newton-Raphson method becomes

$$d\underline{\boldsymbol{\Psi}} = \left(\mathbf{K}_\mathrm{L} + \mathbf{K}_\mathrm{NL} + \mathbf{K}_\sigma\right) d\underline{\mathbf{u}}_n = \mathbf{K}_\mathrm{T} d\mathbf{u}_n \tag{4.40}$$

where $\mathbf{K}_T$ is the total tangential stiffness matrix and $d\underline{\boldsymbol{\Psi}}$ represents the unbalanced force vector. In one step loading, after the solution of equation (4.40), the iteratively obtained matrix $d\underline{\mathbf{u}}_n$ is added to the displacement vector and the residual force $d\underline{\boldsymbol{\Psi}}$ vector is calculated. This iterative process continues until the residual force vector becomes sufficiently small or vanishes. To summarize:

1. A first approximation $\underline{\mathbf{u}}_{n,0}$ is obtained from linear elastic solution.

2. The residual $\underline{\Psi}_0$ force vector is found using equation (4.27) with the calculated **B** and **S** matrices which are functions of $\underline{\mathbf{u}}_{n,0}$.

3. The tangential stiffness matrix $\mathbf{K}_T$ is assembled.

4. The new correction $d\underline{\mathbf{u}}_n$ is computed using

$$\mathbf{K}_T d\underline{\mathbf{u}}_n = d\underline{\Psi} \tag{4.41}$$

5. The norm of the residual vector $d\underline{\Psi}$ is computed

6. The process steps, 2, 3, 4, and 5 are repeated until $\underline{\Psi}$ is sufficiently small.

The tangential stiffness matrix $\mathbf{K}_T$ can be updated at every iteration or it can be taken constant throughout the iteration. The latter case is known as the modified Newton-Raphson method and is computationally less expensive and even more stable for some kinds of nonlinear problems. But the convergence is sometimes slower for the modified Newton-Raphson method.

A one-step solution for a nonlinear problem is usually not appropriate and may give inaccurate result. It is better to proceed by incrementing the load and obtaining the corresponding incremental displacement. This process is also computationally cheaper because the effects of nonlinearity at each step are reduced. However, it is important to check the total equilibrium error at every increment by using equation (4.27). In the incremental method, the load is incremented and corresponding incremental displacement is found by iteration. This can be summarized using index notation as

$$\underline{\mathbf{u}}_j^i = \underline{\mathbf{u}}_{j-1}^i + \Delta\underline{\mathbf{u}}_j^i \tag{4.42}$$

where, i and j are increment numbers of the loading and iteration number respectively. Incremental-iterative displacement $\Delta\underline{\mathbf{u}}^i_j$ is obtained using the following equation

$$-\mathbf{K}^i_{j-1}\Delta\underline{\mathbf{u}}^i_j = \underline{\boldsymbol{\Psi}}\left(\underline{\mathbf{u}}^i_{j-1}\right) = \left[\mathbf{K}_L + \mathbf{K}_{NL}\left(\underline{\mathbf{u}}^i_{j-1}\right) + \mathbf{K}_\sigma\left(\underline{\mathbf{u}}^i_{j-1}\right)\right]\underline{\mathbf{u}}^i_{j-1} + \mathbf{f}^i_{j-1} \tag{4.43}$$

where, $\mathbf{K}^i_{j-1}$ is the tangential stiffness matrix of the structure evaluated at the beginning of the *i*th iteration. The updated displacements $\underline{\mathbf{u}}^i_j$ obtained from Eq. (4.42) are used to evaluate the current stresses.

## 4.4 Benchmark examples for nonlinear large deformation analysis

The governing equations for the nonlinear finite element formulation described in the previous sections were implemented into the FRAC3D [3] finite element code. In an effort to check the implementation, some benchmark examples were run. One example, which shows geometric nonlinearity and has a closed form solution, is the well known "elastica" problem. This problem is a good example with small strains and large rotations, and is suitable for the finite element formulations developed in the previous sections. The closed form solution of the "elastica" can be found in the literature [26, 27]. For the benchmark test, a cantilever beam subjected to a vertical load at the free end was considered (Fig. 4-1). The length of the beam is 10 units and the cross-section is one-unit square.

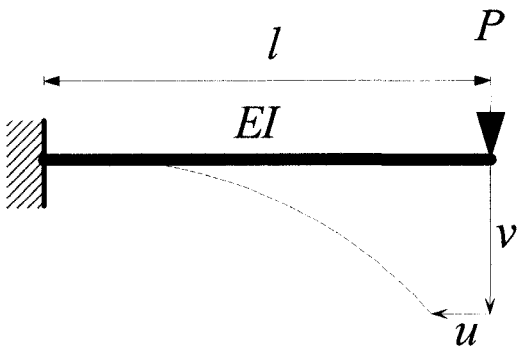


**Fig. 4-1** The elastica problem considered in the benchmark test

Fig. 4-2 shows the theoretical and FRAC3D tip displacement results in the vertical and horizontal directions. The Newton-Raphson method was used and the global tangent stiffness matrix was updated on every increment. As can be seen in the plot, the FRAC3D results match quite well with the analytical predictions [26-28]. At the initial phase of the incremental loading, there is less than one-percent difference in the horizontal and vertical displacements as compared to analytical results. However, at later increments, the differences in the analytical and the FRAC3D results are slightly less than 3-4 percent. This difference can be attributed to the inextensible beam and plane-stress assumption in the analytical solution. Fig. 4-3 and Fig. 4-4 show the front and perspective views of the undeformed and the final deformed shape from the FRAC3D computation. Overall, the benchmark comparisons are in very good agreement.

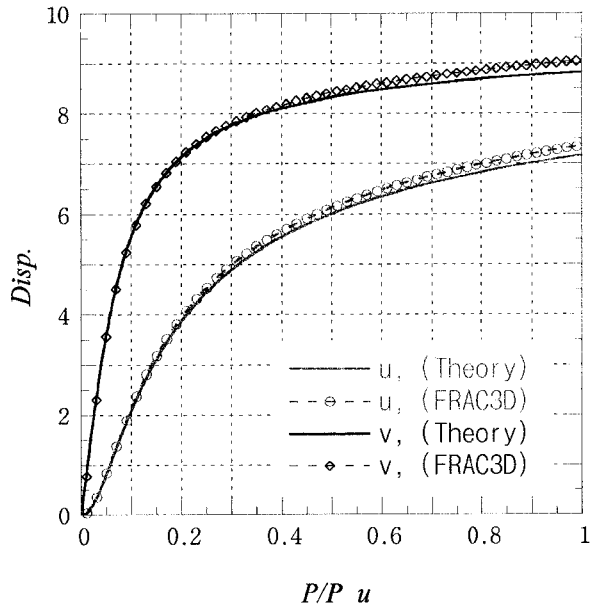


**Fig. 4-2** Cantilever beam tip displacements for elastica problem

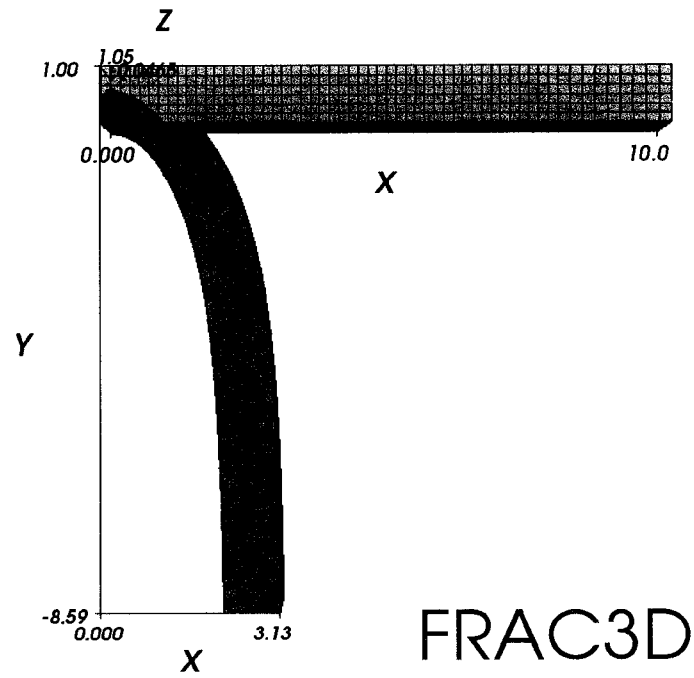


**Fig. 4-3** Front view from FRAC3D results. Undeformed and final deformed configurations

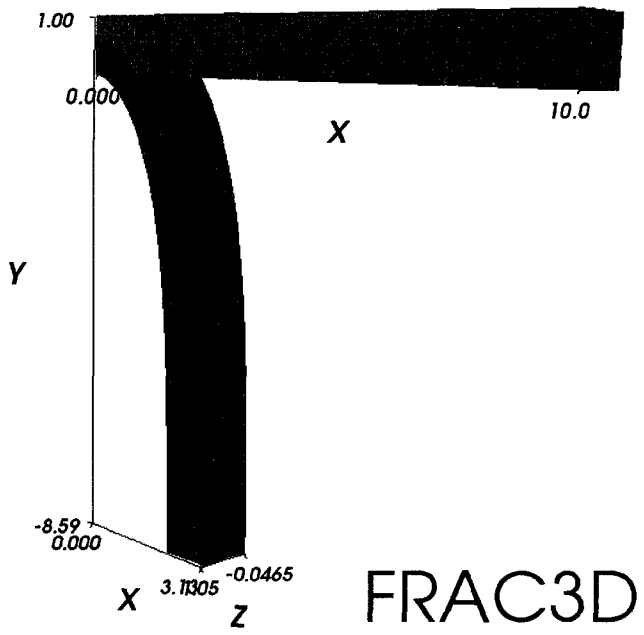


**Fig. 4-4** The FRAC3D results. Undeformed, and final deformed configurations

# CHAPTER FIVE: FINITE ELEMENT BUCKLING ANALYSIS

## 5.1 Introduction

In the previous chapter, the finite element formulation for the geometrically nonlinear behavior was presented. Strain and stress definitions in a geometrically nonlinear continuum were reviewed and the equilibrium equation, based on the principle of the virtual work, was derived in a manner suitable for the finite element implementation. In this section the finite element formulation for initial buckling (eigen) analysis of three dimensional structures will be examined in detail.

## 5.2 Preliminaries

Buckling is a well known failure mode related to the loss of the stability from an equilibrium configuration. However, the occurrences of local buckling may not cause global failure. The external loads that may result in local buckling can be compressive, tensile, thermal, etc. There are various classical forms of buckling that are classified according to the postbuckling behavior. These include bifurcation, snap-through, and snap-back buckling modes. In bifurcation buckling, there are two (or more) equilibrium solutions, thus the actual solution path depends on small

perturbations in geometry or loading. A classical example of bifurcation buckling is column buckling, e.g. a column can buckle in two possible directions in a plane. In snap-through or snap-back buckling, there is a sudden displacement or force change. Because of the problems of interest in this study, bifurcation buckling will be examined in detail.

Bifurcation buckling occurs when a structure itself converts membrane strain energy into bending strain energy, without a corresponding change in the externally applied load. Once the geometry starts to deform, it can no longer withstand even a small fraction of the initially applied force. In slender structures, such as columns, thin plates, and shells, the membrane stiffness is usually much greater than the bending stiffness, and a large amount of membrane energy can be stored for correspondingly small deformations. When buckling occurs, comparatively large deformations result from the release of the stored membrane strain energy.

The effect of membrane stresses on the lateral deflection are accounted for by the geometric matrix $\mathbf{K}_\sigma$ which contributes to the tangential stiffness matrix $\mathbf{K}_T$ in the finite element method. The geometric stiffness matrix $\mathbf{K}_\sigma$ is a function of the structure geometry, displacement field, and the state of the membrane stress. This matrix is also called the "initial stress stiffness matrix". In a finite element formulation, the global geometric stiffness $\mathbf{K}_\sigma$ matrix is assembled in the same way that the conventional global stiffness matrix, $\mathbf{K}_L$, is assembled. Initiation of bifurcation buckling can be reduced to the solution of an eigenvalue problem. The solution has the same form as in vibration problems, but with the mass matrix $\mathbf{M}$ replaced by the geometric stiffness matrix $\mathbf{K}_\sigma$, in a buckling analysis.

## 5.3 Linearized buckling analysis

The buckling problem can be formulated either directly using energy principles or using the incremental nonlinear formulation of the internal and external finite element force balance formulation as explained in the previous chapter. In this section the force balance method will be used.

In the incremental nonlinear analysis of structures, the incremental force deformation relation is given by

$$\left(\mathbf{K}_{\mathrm{L}}+\mathbf{K}_{\mathrm{NL}}+\mathbf{K}_{\sigma}\right) d\underline{\mathbf{u}}_{n}=\mathbf{K}_{\mathrm{T}} d\mathbf{u}_{n} \tag{5.1}$$

where $\mathbf{K}_T$ is the nonlinear tangential stiffness matrix which consist of three stiffness matrices

$$\mathbf{K}_{\mathrm{T}}=\mathbf{K}_{\mathrm{L}}+\mathbf{K}_{\mathrm{NL}}+\mathbf{K}_{\sigma} \tag{5.1}$$

These three matrices are the linear stiffness $\mathbf{K}_L$, nonlinear stiffness, $\mathbf{K}_{NL}$, and the geometric stiffness, $\mathbf{K}_\sigma$, matrices respectively. The nonlinear stiffness and geometric stiffness matrices are nonlinear functions of the displacements. The incremental solution requires successive iterations to converge to the correct displacements. If the structure is sufficiently stiff, it will only exhibit small geometry changes before buckling. In this situation, the nonlinear stiffness matrix can be omitted and geometric stiffness matrix becomes a linear function of the displacements. Based on these assumptions, Equation (5.1) can be linearized as

$$\left(\mathbf{K}_{\mathrm{L}}+\mathbf{K}_{\sigma}\right) d\underline{\mathbf{u}}_{n}=\mathbf{0} \tag{5.2}$$

where $\mathbf{K}_\sigma$ is the geometric stiffness matrix consisting of the previous step's stress values which are linear function of displacements. Linearized buckling analysis searches the stress level at which the instability occurs without any significant load increment. If we quantify that level using a coefficient $\lambda$, then the governing equation becomes

$$\left(\mathbf{K}_L + \lambda \mathbf{K}_\sigma\right)\underline{\mathbf{u}}_n = \mathbf{0} \tag{5.3}$$

This is the eigen-analysis problem to be solved. The $\lambda$'s are the eigenvalues or simply the coefficient of the external loads which cause buckling. The eigen-vectors $\underline{\mathbf{u}}_n$ are the deflected shapes of the structure at the critical magnitude of the load when buckling occurs. The computational procedure can be summarized as follows. First, a linear elastic solution for full loading is obtained and the stress values at the nodes are obtained. Next, the geometric stiffness matrix $\mathbf{K}_\sigma$ is formed. Then, equation (5.3) is solved for the eigenvalues $\lambda$ and eigenvector $\underline{\mathbf{u}}_n$.

There are various methods to solve the eigenvalue problem given by equation (5.3). Because of the large number of equations in the formulation of eigen-problem in finite element analysis, it is required that an efficient matrix storage format be utilized. Storage of global stiffness matrices in a finite element analysis requires large memory allocations during full global matrix assembly. Global stiffness matrices are generally very sparse matrices, typically 80-90% sparse. Because of the sparseness of the matrices, they must be stored efficiently using special sparse matrix storage techniques. There are various sparse matrix storage formats and schemes. The FRAC3D program currently uses the Yale sparse matrix format [29] to store the global

stiffness matrix. Efficient and economical solution methods for large scale eigen-problems are important topic in finite element research. In this study, the subspace iteration method [30] was used to find critical buckling load and eigen-modes. This method is especially suitable for the problems requiring a few smallest eigenvalues and corresponding eigenmodes [30].

For buckling analysis, the FRAC3D three-dimensional finite element code was modified to compute eigenvalues and eigenvectors. The code was originally developed to handle linear and nonlinear three-dimensional fracture analyses. For fracture analysis, the program uses special enriched crack tip elements to embed the "correct" crack tip stress singularity into the formulation. In addition, the program contains transition elements to force compatibility between the enriched elements and regular elements around the crack tip (see, Appendix A). The detailed formulation can be found in the [4]. The code was extended to handle eigen-analysis for buckling problems using the subspace iteration method. The subspace iteration method is a more generalized form of the inverse iteration method, in which a single eigen-pair is calculated. Optionally, a Sturm sequence check can be applied to check the sequence order of the eigenvalues [30].

## 5.4 Subspace iteration method

Subspace iteration is one of the most widely used methods in finite element eigen-analysis for computing the eigenvalues associated with sparse matrices. The

subspace iteration method was developed and named by K. J Bathe [30] and mainly includes three steps. The main concept in the subspace iteration method is to find the lowest $p$ eigenvalues and corresponding eigenvectors which satisfy the following equation.

$$\mathbf{K}_L\mathbf{\Phi} = \mathbf{K}_\sigma\mathbf{\Phi}\mathbf{\Lambda} \tag{5.4}$$

$\Lambda$ is a diagonal matrix containing $p$ eigenvalues on the diagonals and $\Phi$ is a matrix containing $p$ eigenvectors in column format. The eigenvectors are normalized with respect to geometric stiffness matrix $\mathbf{K}_\sigma$, which satisfies the orthanormality condition, i.e.

$$\mathbf{\Phi}^T\mathbf{K}_\sigma\mathbf{\Phi} = \mathbf{I} \tag{5.5}$$

The matrix $\mathbf{I}$ is a unit matrix of order $p$ and $\Phi$ stores only $p$ eigenvectors. The method starts by establishing $q$ iteration vectors which are greater than the number of eigenvectors (eigenmodes) $p$, to be calculated, $q>p$.

- Simultaneous inverse iterations are performed on the $q$ vectors and the Ritz method is used to obtain the eigenvalues and eigenmodes until convergence for the eigenvalues occurs
- A Sturm sequence check is performed to make sure that the required eigenvalues and eigenvectors calculated are in ascending order.

The name for the method is attributed to using q-dimensional subspace. The method should not be regarded as a simultaneous iteration with q individual iteration vectors. Instead the solution space is assumed to span on $q$-dimensional space. The

Sturm sequence check and establishing the $q$ iteration vectors are very important parts of the method.

## 5.5 Numerical benchmark tests

In order to test the accuracy of the eigen-solver implemented into the FRAC3D finite element program, some benchmark problems were tested and the results are compared with 2-D analytical results.

### 5.5.1 Benchmark Test-1: fixed-fixed Column heated with uniform temperature

The first benchmark problem is a heated beam with both the end surfaces are restrained in all directions. The results were compared with known theoretical results, showing good agreement.

For a column with one end free and the other end restrained in $x$-direction, the elastic thermal strain at the free end is given as

$$\varepsilon = \alpha(\Delta T) \tag{5.6}$$

where $\alpha$ is the coefficient of thermal expansion and $\Delta T$ is the change in temperature. When the free end is restrained in the both $x$- and $y$-axis, then the thermally induced force in the beam becomes

$$P = E\varepsilon A = E\alpha(\Delta T)A \tag{5.7}$$

If we substitute this force into the Euler buckling formula for a fixed-fixed column, the $n^{th}$ mode buckling force is

$$P_{cr,n} = \left(\frac{2n\pi}{L}\right)^2 EI = E\alpha(\Delta T_n)A \tag{5.8}$$

where $I$ is the moment of inertia, $L$ is length, and $E$ is Young's modulus of the column. From equation (5.8), the temperature causing buckling can be obtained as

$$\Delta T_n = \left(\frac{2n\pi}{L}\right)^2 \frac{I}{A\alpha} \tag{5.9}$$

For the benchmark example, a beam with a square section of 1x1 cm and 10 cm length was considered. Young's modulus and Poisson's ratio are 70 GPa and 0.3 respectively.

Table 5-1 shows both the theoretical and numerical (FRAC3D) results.

**Table 5-1** Theoretical and numerical buckling temperatures for the fixed-fixed column

| | First | Second | Third |
|---|---|---|---|
| Theory | 3290 | 4935 | 8225 |
| FRAC3D | 2866 | 5172 | 8660 |

The differences between the theoretical and FRAC3D results can be attributed to the three-dimensional modeling, Poison's ratio effect and likely numerical errors. However, the buckling modes closely match the 2-D analytical results. Thus, we can

conclude that the numerical critical stress values match quite reasonably for this benchmark example.

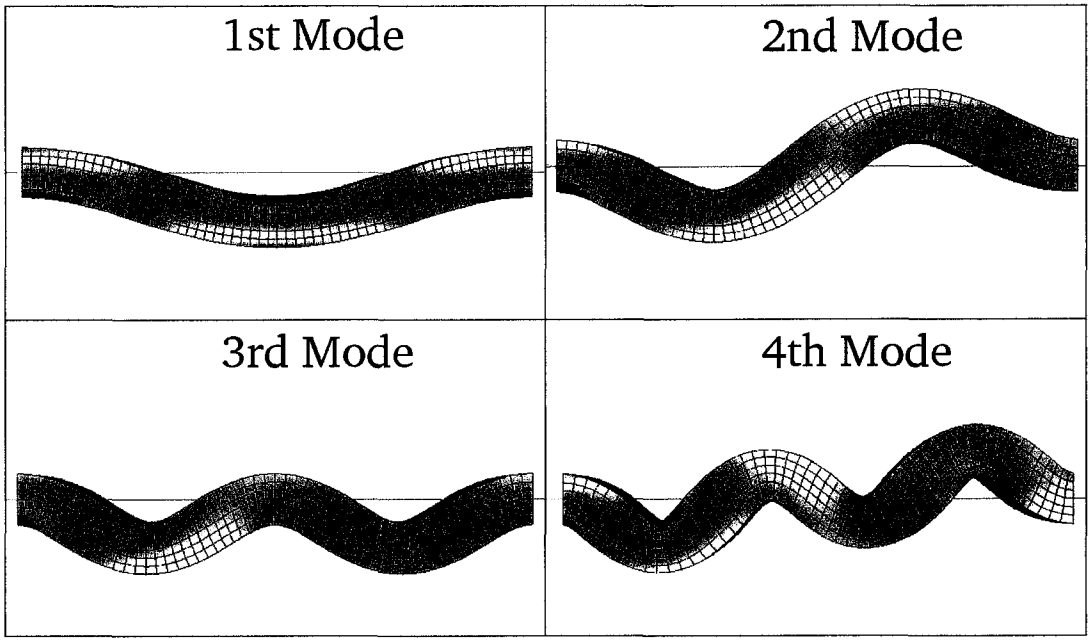


**Fig. 5-1** The first 4 buckling modes for fixed-fixed column under uniform thermal heating

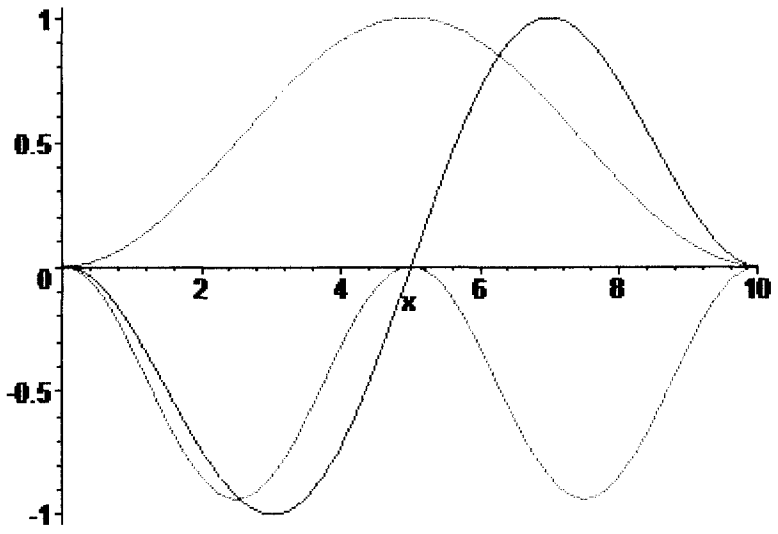


**Fig. 5-2** The theoretical mode shapes for buckling of fixed-fixed column

### 5.5.2 Benchmark Test-2: Buckling of Fixed-Free column under compressive load

A second 3-D benchmark test is the buckling analysis of a fixed-free column under compression. The first critical buckling load is almost the same as the theoretical 2-D result, but the second and third buckling loads exhibit some differences which are most likely attributed to 3-D effects and the inextensible assumption in the 2-D analysis.

**Table 5-2** Theoretical and numerical buckling loads for the fixed-free column

| | First | Second | Third |
|---|---|---|---|
| Euler Theory | 9.8696 | 88.8264 | 246.7401 |
| FRAC3D | 9.8667 | 83.3085 | 207.3315 |

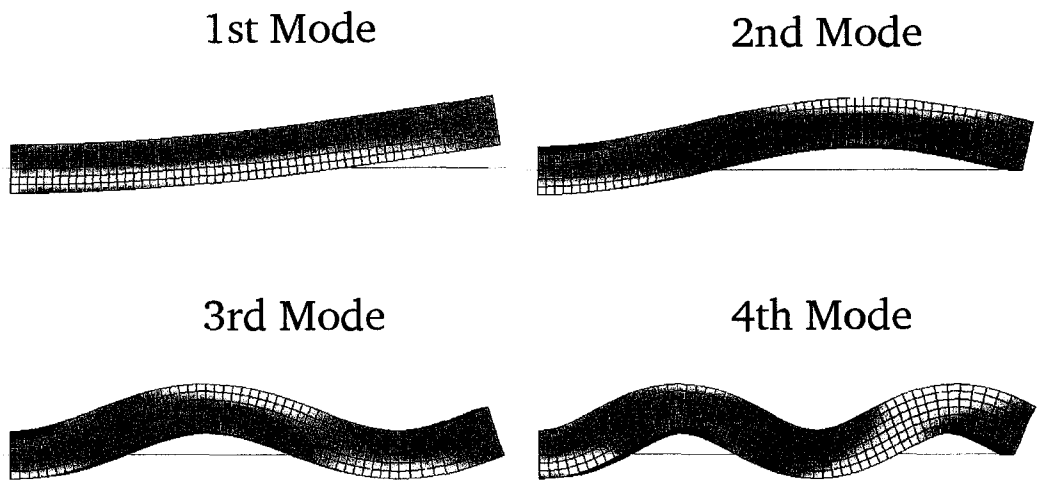


**Fig. 5-3** First four buckling modes shapes of a fixed-free column

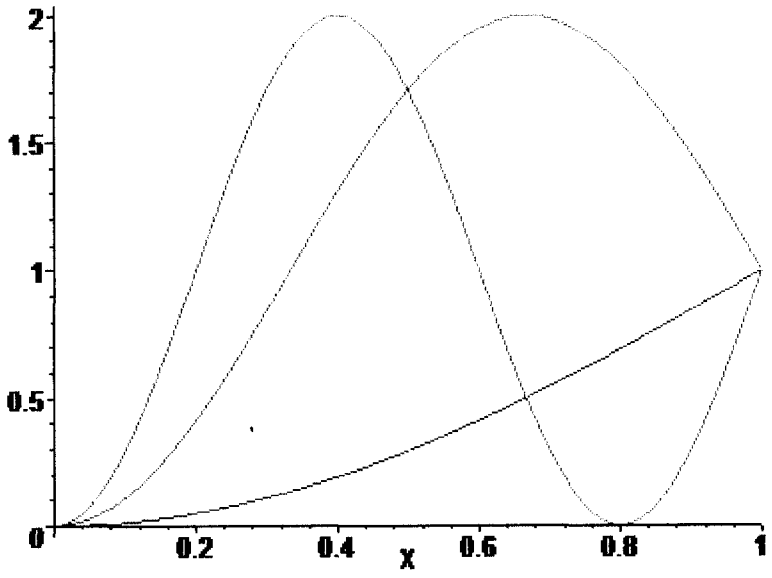


**Fig. 5-4** The theoretical mode shapes for buckling of fixed-free column

# CHAPTER SIX: LOCAL BUCKLING OF THIN PLATES SUBJECTED TO TENSILE LOADS

## 6.1 Introduction

Thin plates with cracks or cutouts, subjected to global tensile loads, can exhibit local buckling due to local compressive stresses around the crack or cutout. The level of axial load causing the buckling is called the critical local buckling load. The stress distribution for an infinite plate with a central crack was examined in the Chapter 2. In linear elastic fracture mechanics, it is well known that the second principal stress distribution parallel to the crack surface is compressive in nature. This stress reaches a local maximum on the crack surface and is equal to the negative of the global applied axial stress. Thus, the crack surface region is where the localized buckling would occur. Since the crack surface is relatively unconstrained, qualitatively a wavy out-of-plane buckling behavior can occur.

## 6.2 Plate model for the buckling analysis

Consider a thin plate with uniform loading in the axial direction with traction free boundary conditions on the edges $y= 0$, $y= L$, $0<x<L$, (Fig. 6-1). The plate support (side-A) is constrained from displacing in all directions ($x$-$y$-$z$). The loading

end (side-B) is unspecified in $y$ and $z$ directions and is free in the loading direction, i.e. $u_y = 0$, $w_z = 0$, $\sigma_x = \sigma_o$ for $x = L$. The uniform stress $\sigma_o$ is in the $x$-direction. The aspect ratio $a/b$ is defined as the ratio of half crack length to half plate width. This is the same plate model described in reference [31] and will be used for the comparison with the finite element results. The plate length and width are $L$ =800 mm, and $2b$ = 400 mm respectively. The elastic modulus and Poisson's ratio are 70 MPa and 0.3 respectively. A fine mesh was used around the crack tips to obtain smooth mode shapes especially in this region. The total number of elements used in the model, depending upon the crack inclination angle and the aspect ratio, were approximately 600-800 elements. The element types were a mix of 32 and 26 noded three dimensional solid elements [3]. In previous studies [11, 31-33], generally plate elements were used to analyze this problem. The higher order 3-D solid element used in this study is computationally more expensive, but represents the true 3-D behavior around the crack. Fig. 6-2 shows a typical meshing for the buckling analysis. The all elements are 3-D solid elements and thickness, $t$, of the elements is 1 mm

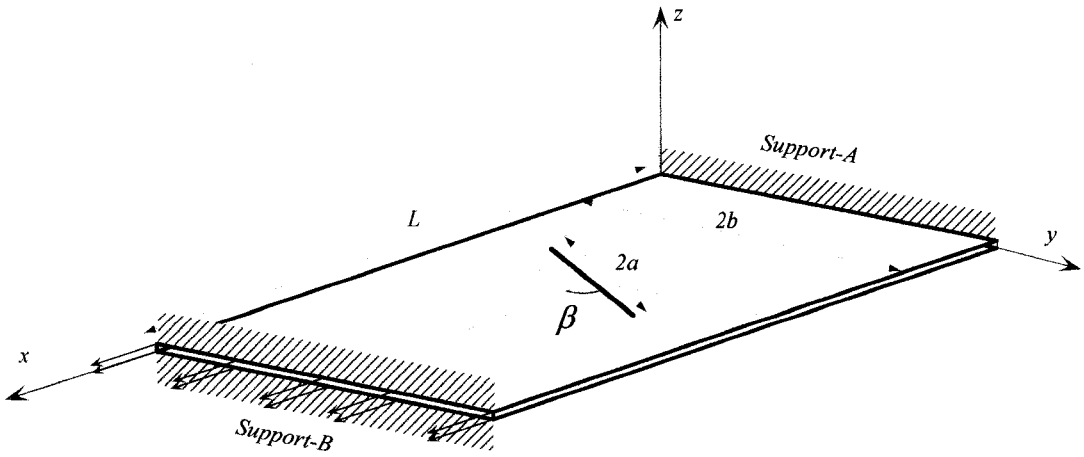


**Fig. 6-1** The finite element plate model for buckling analysis

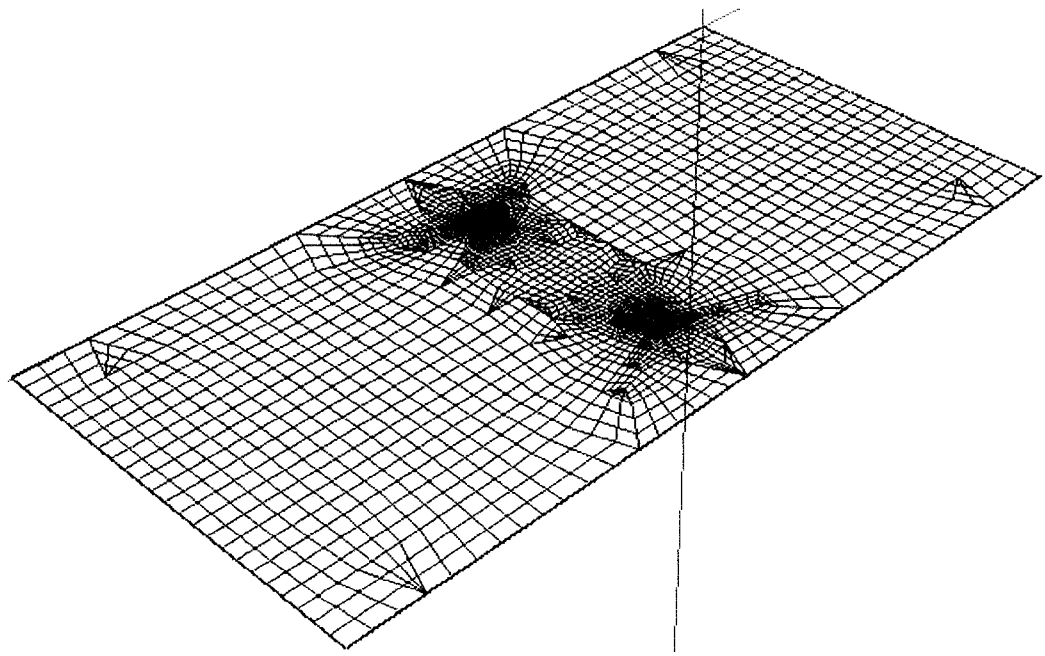

**Fig. 6-2** Typical mesh for the full 3-D finite element model

## 6.3 The critical buckling loads

The critical buckling stresses versus the aspect ratio (*a/b*) are shown in the Fig. 6-3 for the model depicted in Fig. 6.1. The critical buckling stress is approximately proportional to inverse square of the crack aspect ratio (*a/b*). The results from the modified version of FRAC3D were also compared with those obtained by Riks et al. [31] with close agreement. The very minor differences can be attributed to the modeling, meshing, and numerical solution methods (plate element versus solid 3-D element). The aspect ratio actually represents the generalized length of a column. The inverse relation between the buckling load and aspect ratio is a common characteristic of buckling problems for simple structures such as, columns, plates, etc.

In Chapter-two, an empirical relationship between the critical buckling load and the ratio of the plate thickness to half crack-length was derived using Euler column theory (Eq.(2.27)). The numerical results obtained using FRAC3D can be used to obtain the unknown coefficient in Eq.(2.27), by using the method of least squares, resulting in the following approximation

$$\sigma_{cr} = 1.38E\left(\frac{t}{a}\right)^2 \tag{6.1}$$

As it can be seen in the Fig. 6-4, this approximation gives very good results for small cracks, but there is a slight overestimation for large aspect ratios. In past research efforts, approximations for the *c* coefficient in Eq.(2.27), based on numerical and experimental tests, are published in the range of 1.01 and 2.6 [12, 13, 22].

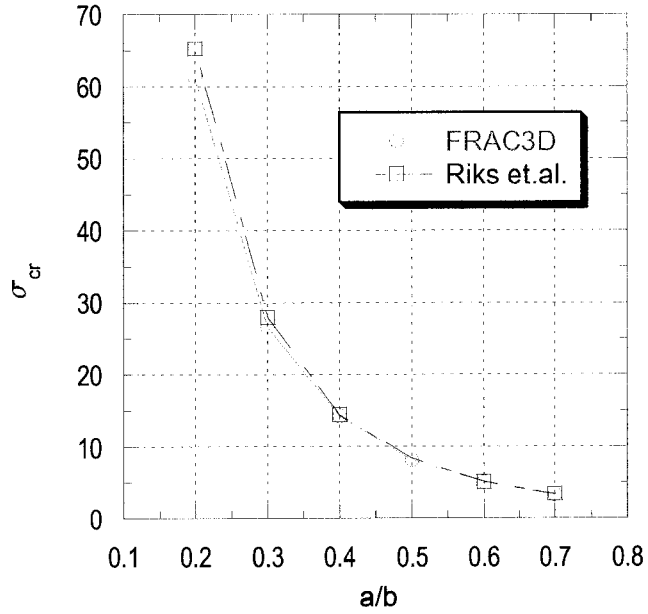


**Fig. 6-3** The critical buckling stress versus crack aspect ratios

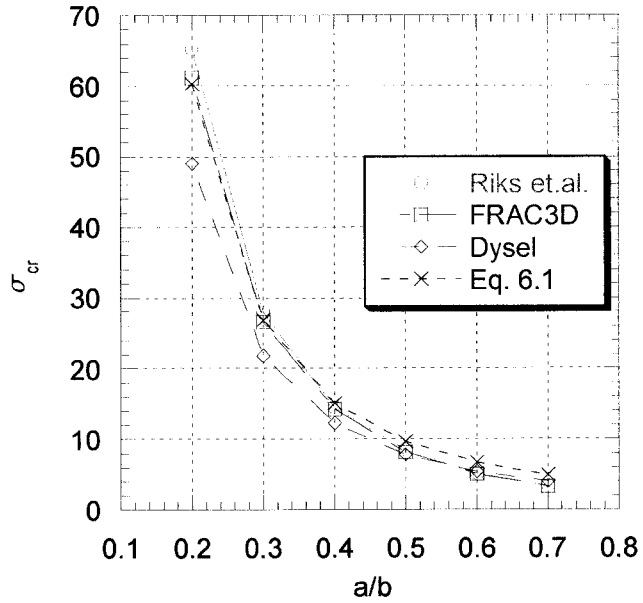


**Fig. 6-4** Comparison of the various analytical results with approximations

The second and higher buckling modes show a behavior similar to the first mode (Fig. 6-5). There is almost constant proportionality between the first and higher buckling loads for the same aspect ratio. To check the proportionality, the second and higher buckling loads were normalized with the corresponding first buckling loads Fig. 6-6. The factors of proportionality for small crack aspect ratios is 1.5, 2.0, 2.5 and so on, i.e., the second, third, and fourth buckling loads are 1.5, 2.0, and 2.5 times the corresponding first buckling load respectively. This proportionality may also be used to modify the approximate formula given in eq. (2.27), since the imaginary column assumption is still very approximate.

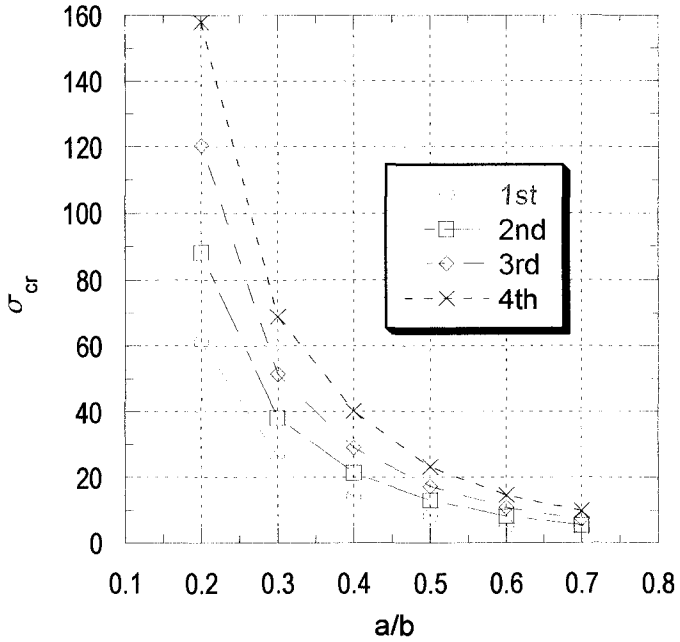


**Fig. 6-5** The first four critical buckling stress values for different crack aspect ratios under tensile load ($t$ = 1 mm)

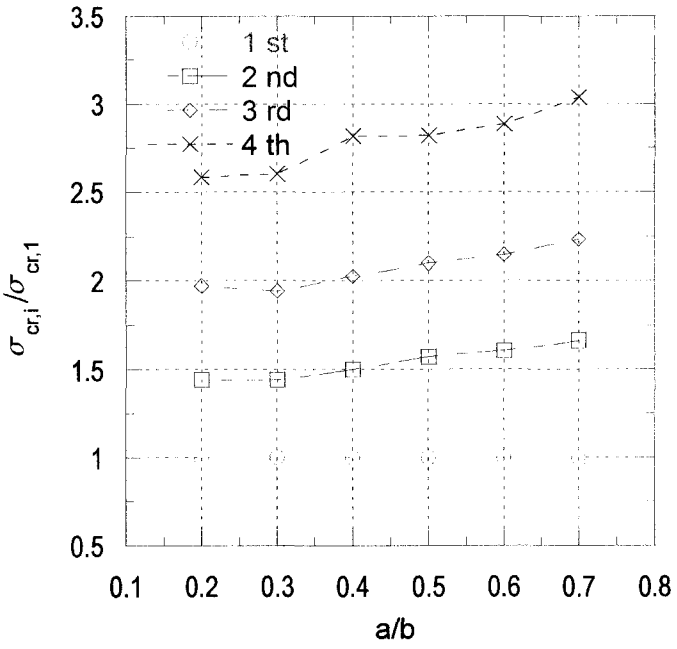


**Fig. 6-6** The normalized critical buckling stresses for different crack aspect ratios ($t$=1)

### 6.3.1 Effects of thickness and inclination angle on the critical buckling loads

As can be seen in figures Fig. 2-14-Fig. 2-18, the compressive stress distribution around the cracks can change significantly depending upon the inclination angle. When the angle of crack inclination, $\beta$, decreases the compressive stress distribution area becomes smaller. This explains why the buckling loads increase as the inclination angle decreases. This is observed in the numerical results (Fig. 6-7). These observations imply that the effective length of the compressed area parallel to the crack surface becomes shorter as the inclination decreases. In the Euler column

theory, the critical load is inversely proportional to the square of the effective column length. Thus, the 2-D stress distributions around the crack are informative about the buckling trend of thin plates with inclined cracks. To the author's knowledge, there is only one other study that examines the inclination angle effects on the buckling loads [32]. Barut et al. [32] mentioned the effects of the inclination angle for a composite cracked structure. But there is still a need for the further investigation of the inclination angle/buckling load relation.

Fig. 6-8 shows the relationship between inclination angles and normalized buckling loads for a crack aspect ratio 0.5 and thickness 1 mm. Decreasing the inclination angle causes an oscillatory behavior in the second and higher normalized buckling loads.

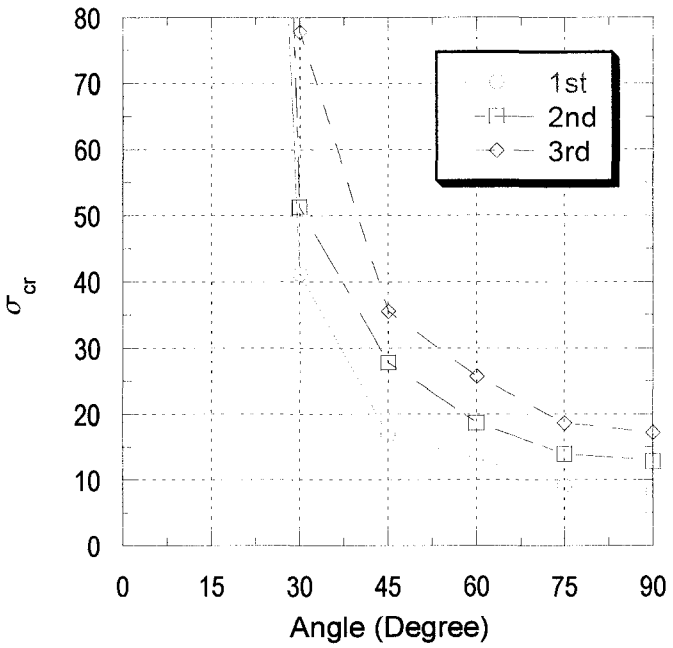


**Fig. 6-7** Critical buckling stress for different inclination angles ($a/b = 0.5$, $t = 1$ mm)

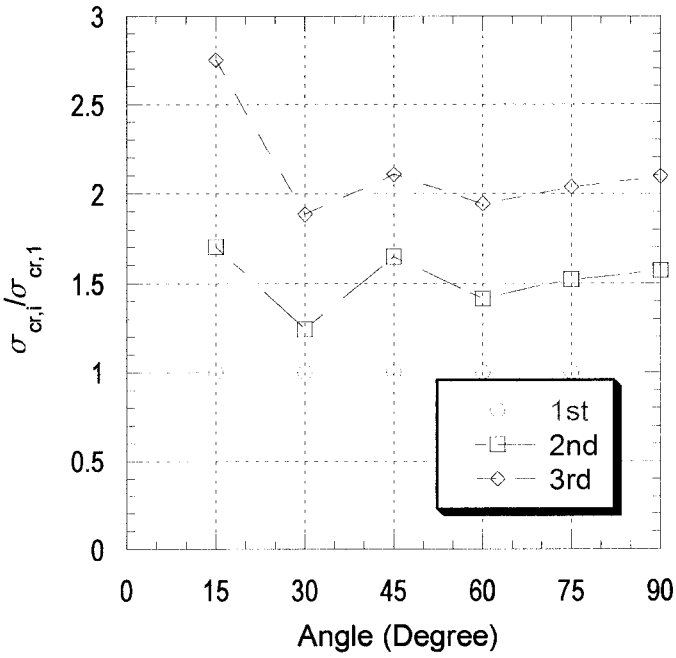


**Fig. 6-8** Normalized critical stresses at different angles (t =1 mm)

The plate thickness is another factor affecting the buckling load level. The buckling load is again approximately proportional to the square of the plate thickness. This proportionality can be seen in Fig. 6-9 and checked with the previously defined approximate buckling eq.(6.1). The approximate buckling load given by eq. (6.1) overestimates the critical buckling load.

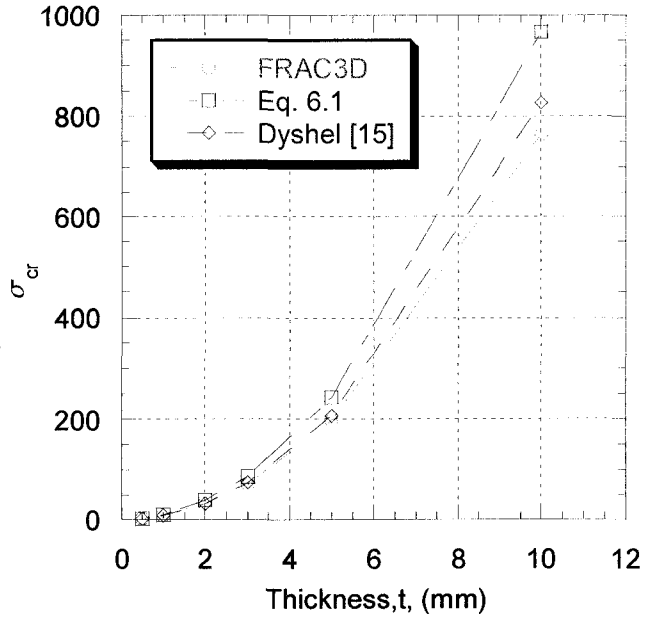


**Fig. 6-9** The effect of plate thickness on the buckling load for the crack aspect ratio of $(a/b) = 0.5$

To examine the effect of plate size on the critical buckling load, and especially plate width, three different plate models were considered. All plate models have the same length of L= 800 mm and the same aspect ratio of $a/b$=0.5. But, the widths of the plates are 400, 800, and 1600 mm as shown on the Fig. 6-10. The effect of crack length on the critical stress ($\sigma_{cr}$), for the same crack aspect ratio (a/b = 0.5), is shown in Table 6-1. It is obvious that the plate width affects the critical buckling load. Thus, the assumptions made for the empirical buckling formula are quite reasonable and sufficient for most investigations.

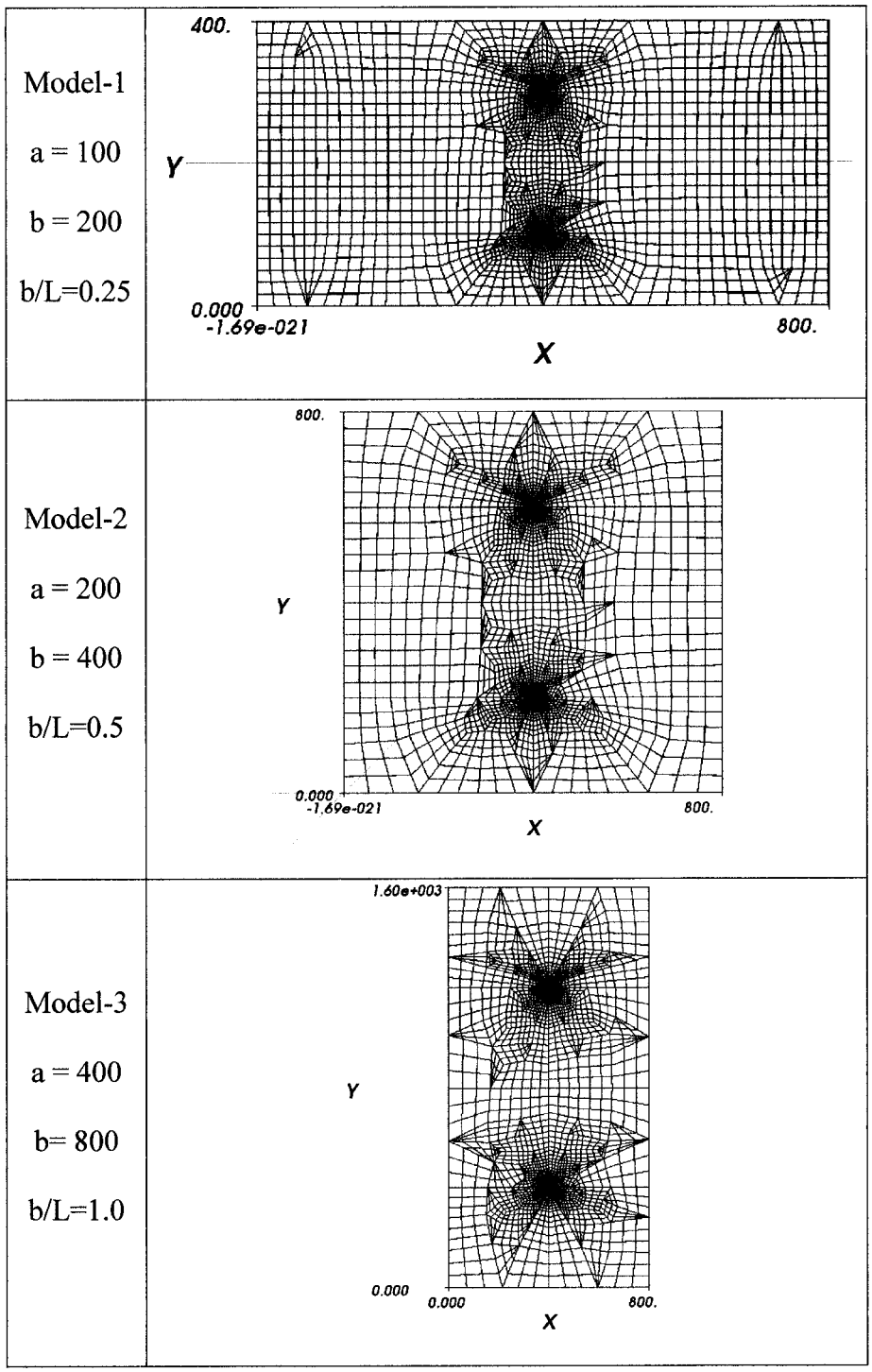


**Fig. 6-10** Three different finite element models with the same length ($L$=800), the same crack aspect ratio ($a/b$ = 0.5), and the same thickness ($t$ = 1.0 mm)

**Table 6-1** The effect of plate width on the buckling load for crack aspect ratio *a/b=0.5*, $t = 1$ mm, and $L = 800$ mm.

| | $\sigma_{cr}$ | | |
|---|---|---|---|
| *a* | FRAC3D | Eq. (6.1) | Dyshel, Ref. [15] |
| 100 (Model-1) | 8.2 | 9.66 | 8.26 |
| 200 (Model-2) | 2.67 | 2.41 | 2.06 |
| 400 (Model-3) | 0.86 | 0.60 | 0.52 |

## 6.4 The buckling modes

Although, the geometric properties, such as the crack aspect ratio, the width-length ratio, thickness, and Poisson's ratio can be any value, the pattern of the buckling modes is remarkably similar as long as the crack aspect ratio and length of the plate are sufficiently large so that the stress distribution outside the crack area is almost constant. From this observation, it can be concluded that the most significant geometric parameters controlling the buckling loads, are the crack length and the plate thickness, as long as the plate is sufficiently wide and long.

The Fig. 6-11 shows the first six buckling modes of a cracked plate subjected to axial tensile load with *a/b* =0.5 and thickness of 1 mm. These are from 3-D calculations using FRAC3D finite element program. The odd modes are symmetric and even modes are anti-symmetric with respect to either the *x* or *y* axis. The first mode shows a "pop-up" behavior in the same out-of-plane direction. The "pop-up"

can affect in-plane axial stresses in the plate. This means that, mode-II cracking is influenced by this buckling behavior.

Buckling modes of thin plates with inclined cracks are quite similar to those of thin plates with straight central cracks (Fig. 6-12). The boundary conditions are exactly the same as those for the plate with a central straight crack described previously. For the even modes, the crack surfaces are misaligned as a result of buckling, because of the inclination. This misalignment increases as the inclination angle increases.

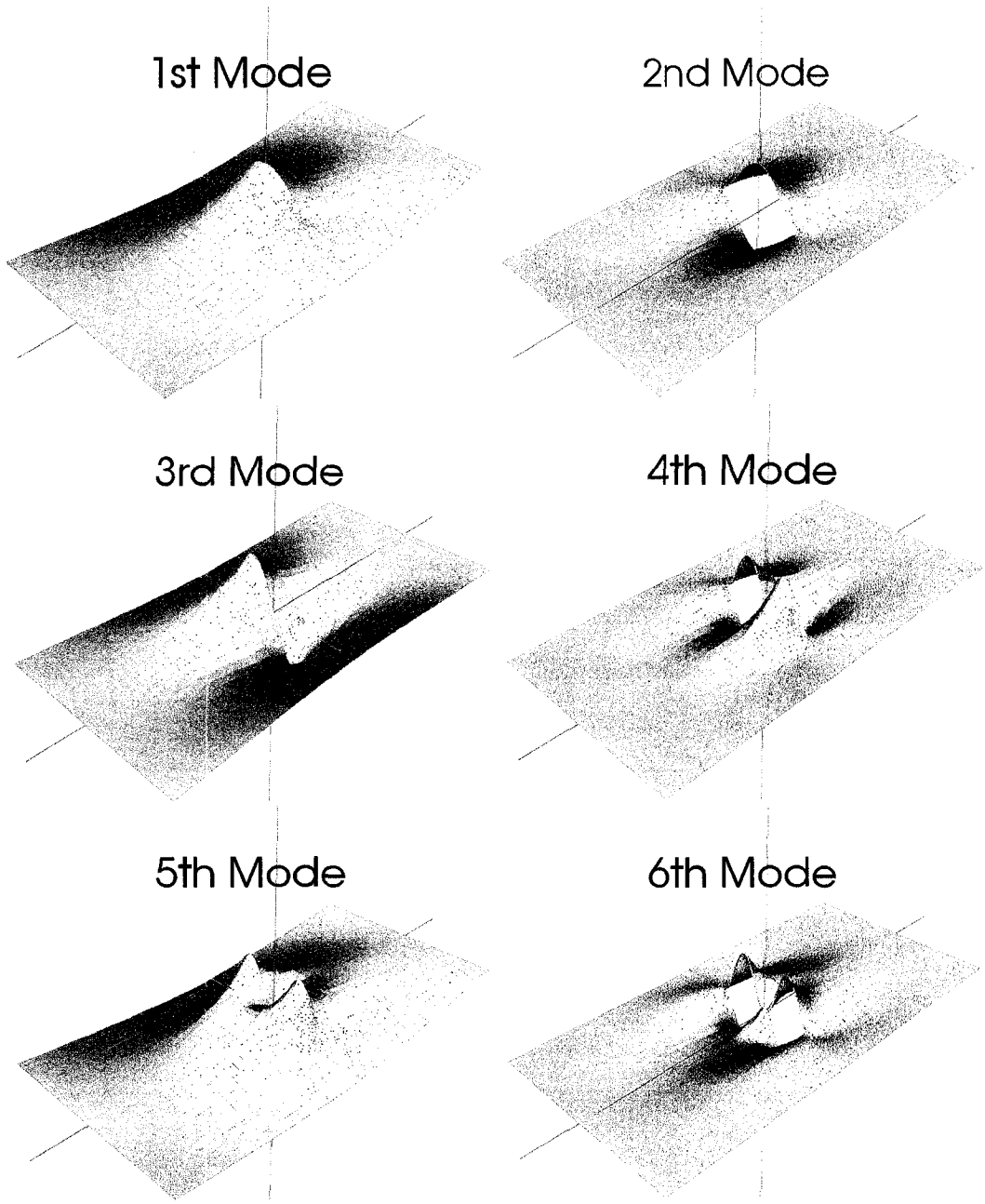


**Fig. 6-11** The first 6 buckling modes for a centrally cracked thin plate ( a/b = 0.5, $L$ =800 mm, $2b$ = 400 mm, $t$ = 1 mm)

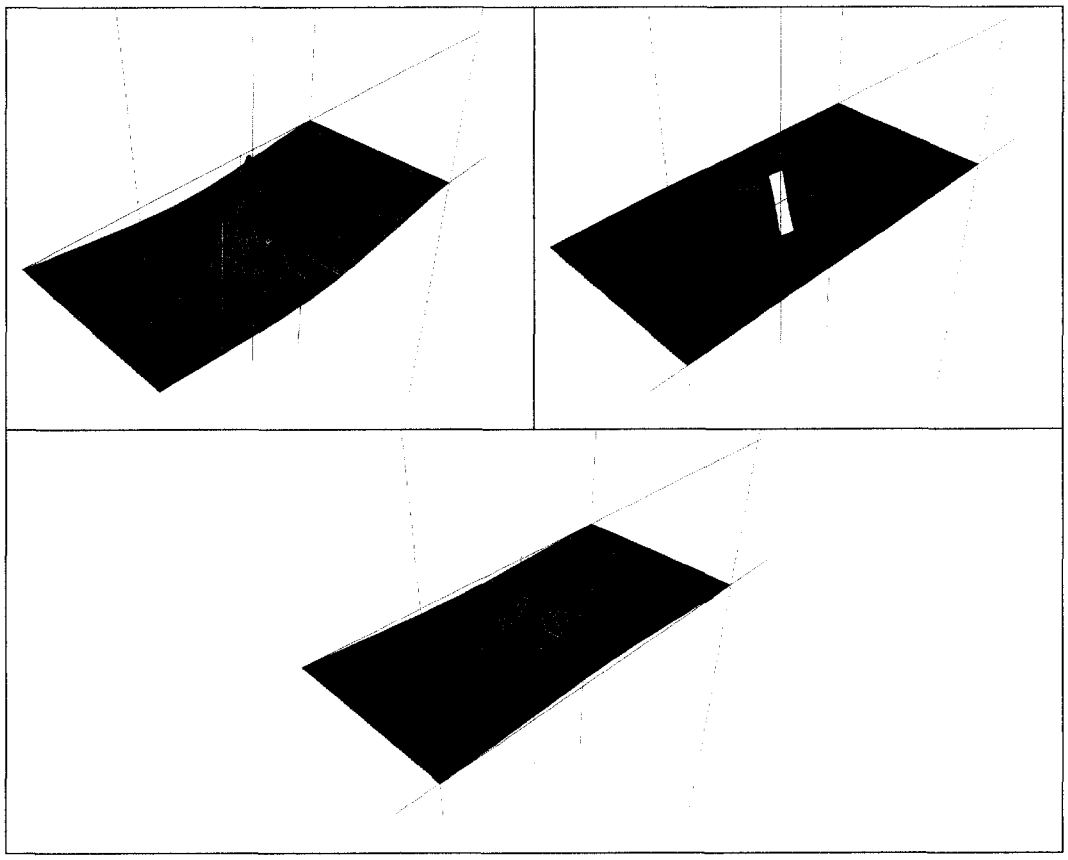

**Fig. 6-12** The first three buckling modes of a cracked plate with $\beta = 70$ inclination angle ($a/b = 0.5$, $L = 800$ mm, $2b = 400$ mm, $t = 1$ mm)

As described previously, the boundary conditions along the non-free edges are not symmetric with respect to plate center. If the crack center is not sufficiently far away from boundaries, the boundary conditions affect the buckling mode shape (Fig. 6-13 and Fig. 6-14). This can be attributed to non-symmetric boundary conditions. Because, in the finite element model (Fig. 6-1), one end of the model (end-A) is kept all-fixed for displacements and the other end (end-B) is free of displacements in loading direction. The plate shown in these figures has a length-width ratio of $L/2b$ =

0.5. The fixed end constrains the displacements at the crack free surface because of its close distance.

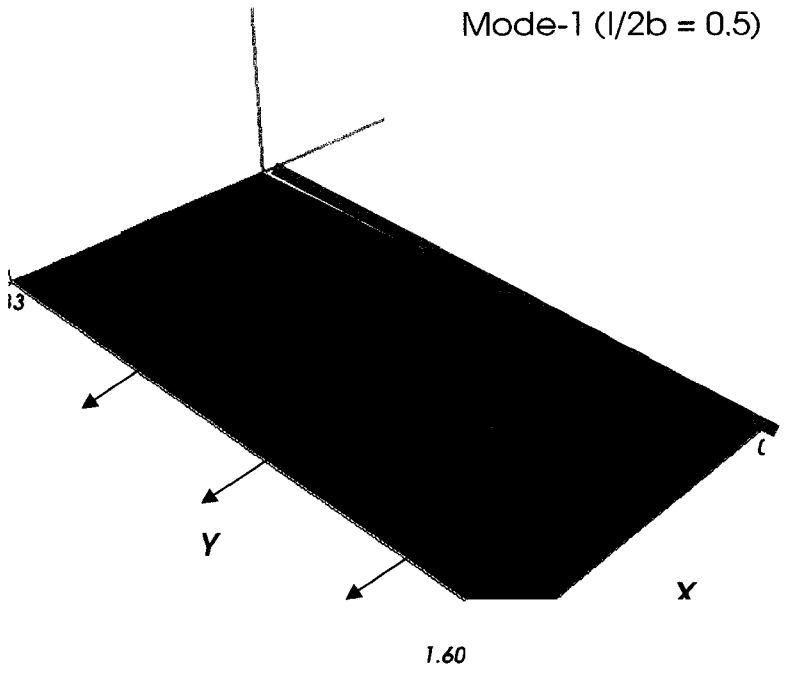


**Fig. 6-13** The first buckling mode for the l/2b=0.5 and a/b=0.5 ($L$ = 800 mm, $t$=1 mm)

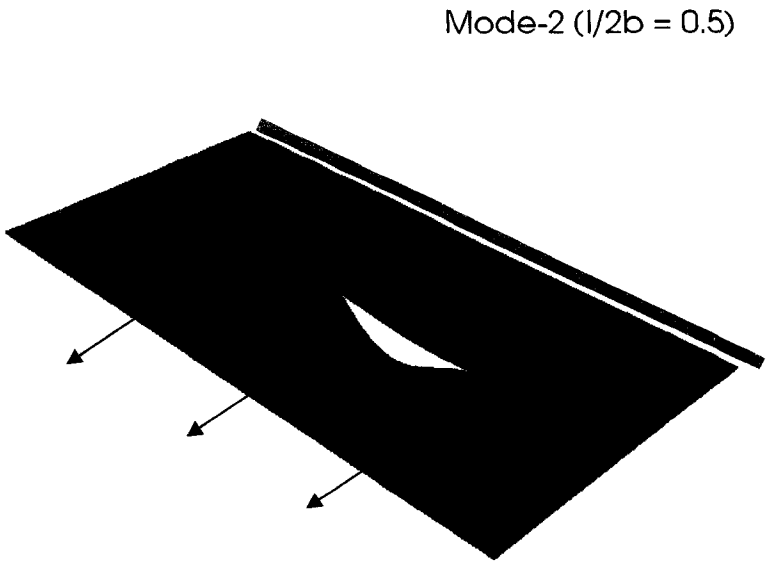


**Fig. 6-14** The 2nd buckling mode for the L/2b=0.5 and a/b=0.5 ($L$ = 800 mm, $t$=1 mm)

To a lesser extent, the same behavior is observed in a square plate (Fig. 6-15, Fig. 6-16). Since, the ratio of the half crack length to the half length of the plate reflects the closeness of the crack to the fixed boundaries, the plate named Model-3 (see-Fig. 6-10) is the model in which mode shape is most heavily affected by the non-symmetric boundary conditions.

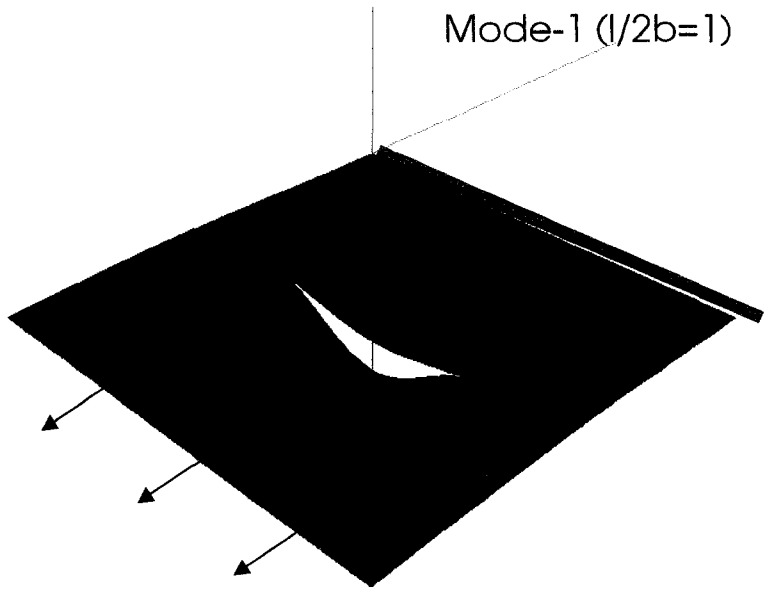


**Fig. 6-15** The first buckling mode for the L/2b=1 and a/b=0.5 ($L$=800 mm, $t$ = 1 mm)

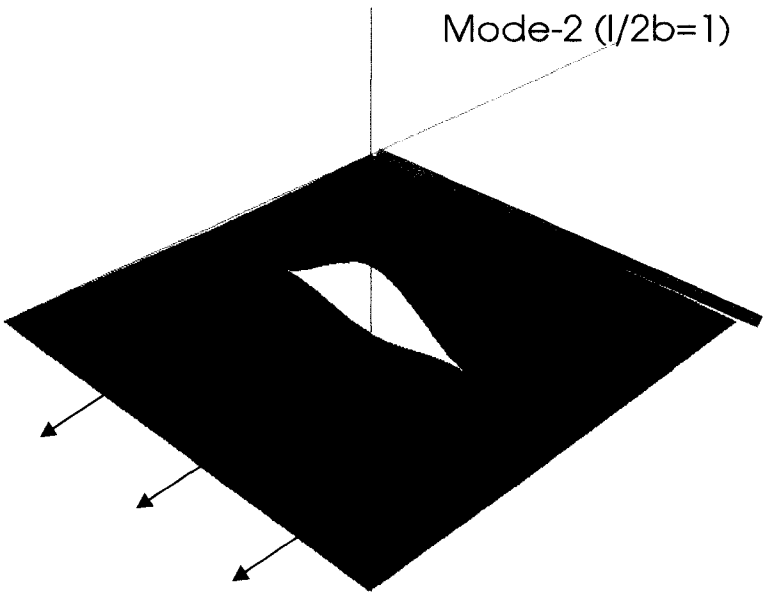


**Fig. 6-16** The second buckling mode for the L/2b=1 and a/b=0.5 ($L$=800 mm, $t$ = 1 mm)

## 6.5 Summary

In this chapter, the main parameters affecting critical buckling loads and mode shapes were investigated. They can be summarized as follows:

I. The most important geometric parameters controlling the critical buckling load level are the normalized thickness and the crack length of the plates.

II. The critical buckling load is almost directly proportional to the square of the *(t/2a)* ratio.

III. The effect of the plate length on the buckling load almost disappears provided that the length of the plate is larger than the plate width (rectangular plate with $L/2b>1.0$)

IV. The second most important parameter is the crack inclination angle, which is defined as the angle between the crack and loading direction.

V. As the inclination angle decreases, the critical buckling load increases.

VI. The normalized second and higher buckling loads are very close to 1.5, 2.0, 2.5... times the first buckling load for the corresponding plate.

VII. The pattern of the buckling mode for different crack aspect ratios (a/b) are similar to each other for rectangular plates with $l/2b>1.0$.

# CHAPTER SEVEN: POSTBUCKLING ANALYSIS OF CRACKED THIN PLATES UNDER TENSILE LOADS

## 7.1 Introduction

The local buckling of cracked thin plates may not cause global failure as soon as the buckling occurs. However, after initial buckling, stress redistribution and large deformations are the main source of possible crack propagation. Plastic deformations may result in ductile materials leading to plastic collapse mechanisms. Only thin plates under tension containinig central crack are only considered in this part of the study. Analytical and numerical solutions are useful for examining fracture behavior under various loading conditions. Together with experimental fracture information, design of structures with possible coupled buckling/fracture behavior can be based on a fracture mechanics methodology.

The simplest of cracked structures, which show local buckling, are thin plates with central cracks subjected to tensile loads. Composite materials with delaminations and electronic packages with blister formations are also common examples of buckling-fracture interaction.

There are various studies on the local buckling of cracked plates under tensile loads [9-16, 22, 31-38]. These studies have focused on the numerical and experimental determination of the critical buckling loads and modes shapes of cracked plates under tensional forces. Few studies have examined the postbuckling behavior of

the cracked thin plates [11, 31, 32]. This can be attributed to numerical difficulties in the analysis of postbuckling behavior for thin cracked plates caused by bifurcation type buckling and simultaneous modeling of fracture behavior. Computational modeling of fracture using finite element programs requires specialized numerical techniques. Petyt [11] analyzed vibration and postbuckling characteristics of plates under tension using purely regular finite elements and didn't directly consider fracture. He used a refined mesh to get a smooth stress distribution around the crack tips. To the author's best knowledge, Riks et al. [31] and Barut et al [32] are the only authors who have specifically traced fracture information in both the pre- and post-buckling state for cracked plates. They used a finite difference technique to compute energy release rate in thin plates, which is defined as

$$G = -\frac{d\Pi}{tda} \approx -\frac{\Pi(a+\Delta a)-\Pi(a)}{t\Delta a} \tag{7.1}$$

where $\Pi$ is the total potential energy of the structure. In terms of finite element formulation this is given by.

$$\Pi=\frac{1}{2}\int_V \underline{\boldsymbol{\sigma}}^T \underline{\boldsymbol{\varepsilon}} dV - \int_V \underline{\mathbf{u}}^T \underline{\mathbf{f}} dV - \int_S \underline{\mathbf{u}}^T \underline{\mathbf{T}} dS - \sum_i \underline{\mathbf{u}}_i^T \underline{\mathbf{P}}_i \tag{7.2}$$

G is defined as the difference between the elastic strain energy and the potential energy of the external loads per unit volume. In the finite difference approximation for the energy release rate, two steps are required to calculate the total potential energy of the structure; (1) Initial calculation with a crack length of $2a$, and (2) a subsequent calculation with a crack length given by $2(a + \Delta a)$. The crack differential $\Delta a$ and the fracture path have to be chosen properly to obtain a good approximation for $G$. This

method is known as the "total potential differential by node release". This approach can be computationally expensive in post-buckling analysis of cracked structures. Another commonly used method is numerical computation of the *J*-integral. In the absence of geometric and material nonlinearities, the potential energy release rate becomes equivalent to the strain energy release rate or path-independent *J*-integral. However, the definition of the *J*-integral is violated if the path begins and ends at different planes due to out-of-plane deformations [32]. Thus, for buckling of cracked structures this method may not be the most suitable. The details of the numerical J-Integral method for fracture calculations can be found in the literature [31, 39]. Barut et al. [32] examined the local buckling of thin composite plates with inclined crack and subjected to tension load. They used the "total potential differential by node release" approach in their postbuckling analysis of composite plates with inclined cracks.

The FRAC3D finite element program has enriched and transition elements to model fracture problems more conveniently than the currently available commercial finite element programs. The FRAC3D program directly computes the stress intensity factors $K_I$, $K_{II}$, and $K_{III}$ [3]. The enriched element method does not need special post-processing procedure to calculate the energy release rate, since the stress intensity factors, $K_I$, $K_{II}$, and $K_{III}$ are calculated directly and the strain energy release rate is obtained from,

$$G_I = \frac{K_I^2}{E'}, \quad G_{II} = \frac{K_{II}^2}{E'} \tag{3}$$

where

$$E' = \begin{cases} E & \text{for generalized plane stress problems} \\ \dfrac{E}{(1-\nu^2)} & \text{for generalized plane strain problems} \end{cases} \tag{4}$$

$$G_{III} = \frac{K_{III}^2}{2\mu} \tag{5}$$

$E$ are $\mu$ are Young's and shear modulus respectively. $\nu$ is Poisson's ratio. Total energy release rate is summation of the energy release rate of the each mode, which is

$$G = G_I + G_{II} + G_{III} \tag{6}$$

## 7.2 Postbuckling analysis procedure

The majority of the previous investigators of postbuckling/fracture phenomenon were occupied with the question of how to model and determine the critical state of the thin cracked plate. The plates considered by these investigators used plate elements and the governing equations were derived using Von Karman's plate theory for buckling of plates [33, 34, 36]. To the author's best knowledge, there are no published results that utilize fully three-dimensional solid elements to model the cracked plate. Although, using plate elements can be adequate for modeling thin plate buckling behavior, it is obvious that the solids elements should be better for computing mixed mode fracture behavior under these complex conditions. In the FRAC3D finite element program, 3-dimensional solid elements, e.g., 32-node hexahedrons and 26-node pentahedrons elements were used to generate results. These elements have cubic shape functions which generally do not require a highly refined

mesh to accurately model severe stress gradients. Of course, cubic elements require a extensive higher order integrations than low order elements, i.e., quadratic and linear elements, but the advantage of using these elements outweighs the disadvantage of additional cpu time required.

The buckling and postbuckling behavior of perfect and imperfect structures, with bifurcation type characteristics, is shown in the Fig. 7-1. Real structures behave as imperfect structures. Mechanical and geometrical imperfections always exist in the real structures. The magnitude and nature of the imperfection controls the deviation from the idealized "perfect" behavior, i.e., the more perfect the system, the less deviation from the theoretical ideal behavior.

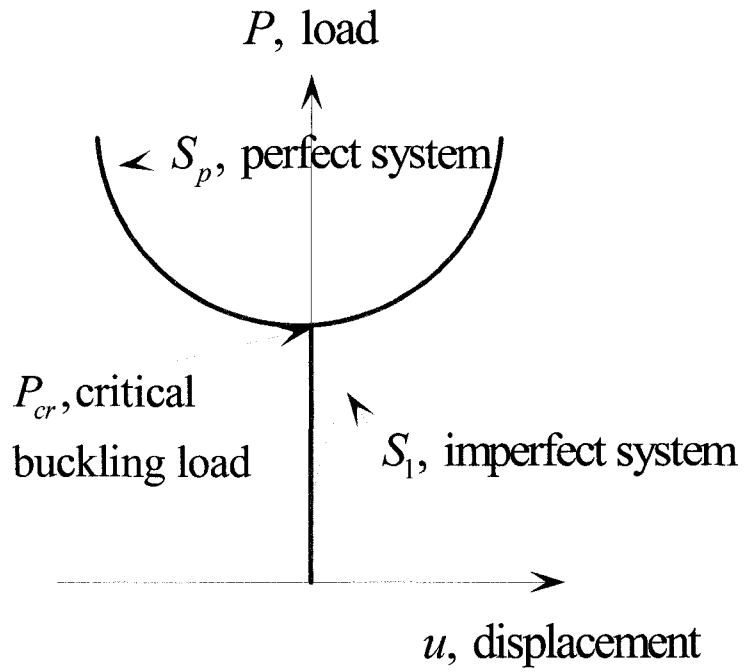


**Fig. 7-1** Typical idealized perfect and imperfect system postbuckling behavior

The numerical postbuckling analysis for perfect systems that exhibits bifurcation type buckling, requires more computational effort than needed for imperfect systems. The most important part of the postbuckling calculation for the perfect system, is the transition from the pre-buckled state to the postbuckled state. If it is assumed that the structure is sufficiently stiff before buckling, linear analysis is sufficient up to critical buckling load. The transition to the posbuckled state requires special handling for the next load and/or displacement increment. For the transition to the post-buckled the critical buckling loads and mode shapes must be used to make the first "guess" at the postbuckling displacements. Thus, the eigen-analysis described earlier is the first step for accurate postbuckling analysis. Riks et al. [31] used path following method for this transition. In the path following method, displacements and loads are incremented with iterations in such a way that both load increments and displacements are subject to some constraints. In the postbuckling analysis of the thin plates with cracks, the linear load increment can be applied after the transition to the post-buckled state, since the behavior is stable bifurcation type (Fig. 7-2). The details of this procedure can be found in the reference [31].

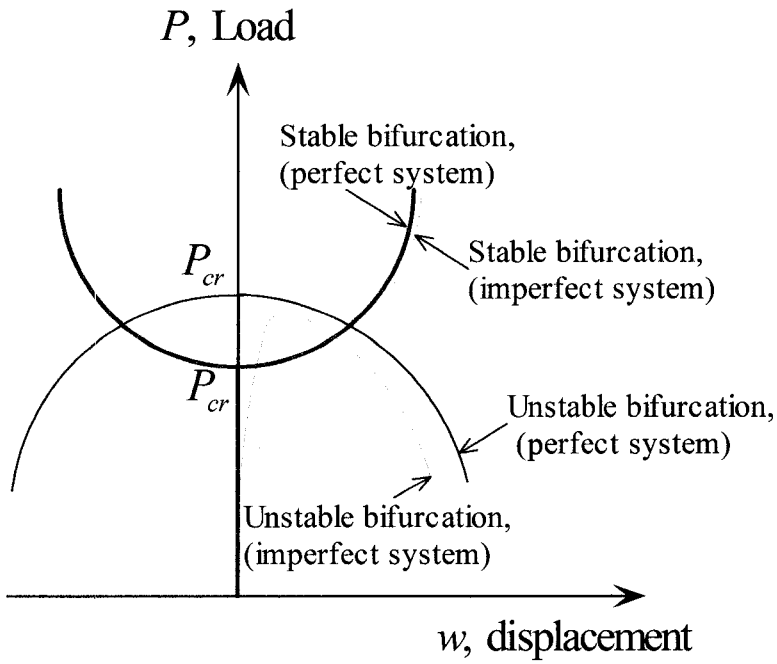


**Fig. 7-2** Stable and unstable bifurcation buckling behavior for perfect and imperfect systems

Numerical postbuckling analysis for an imperfect system in certain cases may not require a special transition procedure from the pre-buckled to the post-buckled state since imperfect systems does not show the sharp bifurcation type load-displacement relationship seen in the idealized buckling of "perfect" structures (Fig. 7-1 and Fig. 7-2). Instead, for an imperfect structure, the transition is smooth. However, the exact location of the buckling level can not be precisely computed. However, the questions, how a perfect system can be converted to an imperfect system and how the degree of imperfection can be adjusted, have to be answered. One commonly used approach involves seeding the initial geometry with imperfections,

often in the shape of one or more the buckling modes. By introducing small imperfections, the bifurcation buckling problem is modified into a snap-through problem. For example, the coordinates of the perfect system are slightly changed by adding a percentage (0.1 -10 %) of the normalized first buckled mode shape. Percentage of the higher mode shapes can also be added to the coordinates. However, if the structure is thin the coefficient for the buckling mode to seed the initial geometry can be taken as some percentage of the thickness, e.g., 5-50% of the thickness. Selection of a proper coefficient to multiply the mode shape(s) may require a number of trial runs to determine sensitivity of the structure to the perturbation coefficients for the assumed mode shapes. If the perturbation of the structure is small, then the structure may be too "stiff" and numerical instabilities may occur during the numerical solution. On the other hand, if the perturbation is too large, then the deviation from idealized behavior becomes large and may not give a good approximation to the true behavior.

The purpose of the numerical displacement perturbation is to make the system slightly imperfect, so that the analysis smoothly follows the deformation path. It should be noted that alternative surface shapes, such as double sinusoidal or co sinusoidal surface shapes, have also been used successfully for imparting a suitable imperfection [32]. Barut et al. [32] used a double cosinusoidal wave with an amplitude of 0.1% of the plate thickness to create the necessary perturbation for imperfect composite plates with inclined cracks. It is believed that, the buckling modes computed from the initial configuration eigen-analysis are more suitable, because this initial "guess" should be closer to the actual postbuckled shape. Thus,

linear eigen-analysis not only is used to calculate the buckling loads and mode shapes, but is also helpful to assign the starting shape for the imperfect system.

The procedure to obtain the imperfect system coordinates using the buckling mode shapes can be summarized as follows [40, 41]. Consider a "perfect" system with initial coordinate vector **X,** and the buckling modes $\phi_i$, obtained from the initial configuration. Then, the imperfect system can be expressed as

$$\underline{\mathbf{X}}' = \underline{\mathbf{X}} + \Delta\underline{\mathbf{X}} \tag{7.7}$$

with

$$\Delta\underline{\mathbf{X}} = \sum_{i=1}^{r} \underline{\mathbf{u}}_i = c_1\underline{\mathbf{u}}_1 + c_2\underline{\mathbf{u}}_2 + c_3\underline{\mathbf{u}}_3 + \ldots + c_n\underline{\mathbf{u}}_n \tag{7.8}$$

where, $\Delta\underline{\mathbf{X}}$ is the imperfection vector, $c_i$'s are constants, $\underline{\mathbf{u}}_i$ is the $i$th mode shape from the buckling analysis of the perfect system, and $r$ is the number of the mode shapes to be considered for the first guess of the buckled shape. Based on the structures, loading conditions, and structural sensitivity, appropriate constant coefficients $c_i$ can be identified by doing some trial analyses using different number of mode shapes and different coefficients, $c_i$'s. For example, for a thin cylindrical shell, taking $c$ as 10 percent of the thickness has been shown to give a reasonable approximation, if only the first mode is considered [40, 41]. The mode shapes $\underline{\mathbf{u}}_i$, from buckling analysis are normalized so that the largest component of the mode shapes has magnitude of 1.0. A couple of modes shapes (1-3) can be good enough for imperfect system. However, a sensitivity analysis, for the number of modes and the corresponding coefficients, $c_i$, to be considered for the imperfect system, may be required. In some cases, one mode is

sufficient, such as in the case of a thin walled cylindrical shell. But, in some cases, such as structures with very close eigen-values (critical buckling loads), it may be required to include more mode shapes in the perturbation.

## 7.3 Benchmark example

The perturbation procedure for imperfection discussed in the previous section was applied to the fixed-free column problem with a rectangular cross-section (see Fig. 7-3). The analytical solution for the postbuckling behavior of a fixed-free column is readily available [26]. For the numerical simulation, the initial (linear) buckling analysis was carried out to obtain the critical loads and corresponding mode shapes. Then, the imperfect column configuration is obtained by a perturbation of original coordinates using a scaling factor $c$ of five percent of the normalized first buckling mode shape. The first buckling mode of the fixed-free column subjected to concentrated axial load at the free end is half sine wave. The Fig. 7-5shows horizontal and vertical tip deflections of a fixed-free imperfect column subjected an axial force. A couple of trial perturbation and postbuckling simulations were conducted to determine how the magnitude of the perturbation affected numerical results. It was observed that reducing the perturbation magnitude to very small values, i.e., $c = 0.01$, may result in an overly stiff structure and cause numerical instabilities close to the theoretical buckling load. Increasing the perturbation causes a large deviation from the theoretical result. Thus, an optimal perturbation using this approach may require a

couple of runs to obtain the "optimal" result. The fixed-free column (Fig. 7-4) has the dimensions of $b$ = 2 ft, $h$ = 1 ft, and $L$ = 10 ft. Only 20-Node quadratic tetrahedron elements were used throughout the meshing. The column is fixed in all directions in one end and free in all directions in the other end. The maximum loading is more than four times of the first critical buckling loading (Fig. 7-5), but the loading was shown in the figure is up to level of 3 times of the critical load. As it can be seen in the Fig. 7-5, there is excellent agreement between the theoretical and numerical results. The initial and final form of the column is shown in Fig. 7-6

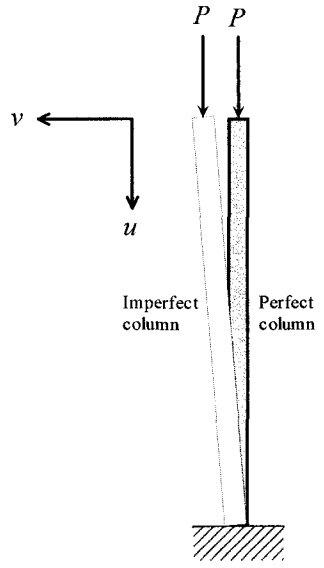


**Fig. 7-3** The fixed-free column


**Fig.** 7-4 Mesh and geometry of the fixed-free column

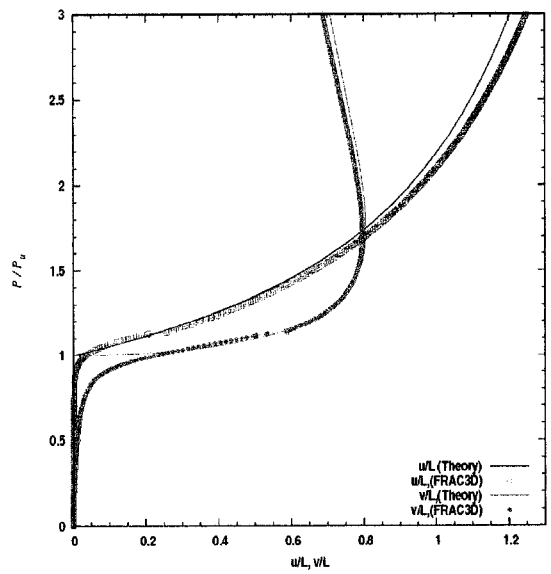


**Fig. 7-5** The benchmark test for postbuckling displacements of a fixed-free column tip

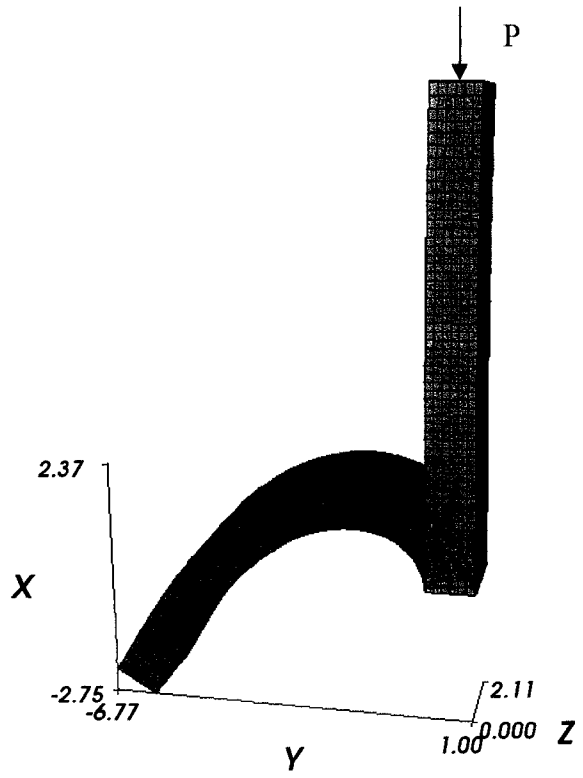


**Fig. 7-6** Postbuckling behavior of the fixed-free column, the initial and final deformed shapes

## 7.4 Coupled Postbuckling/fracture behavior

Consider a thin plate with a central straight crack and subjected to uniform axial distributed loads in a direction perpendicular to the crack (Fig. 7-7). The length, width, and thickness of the plate are *2l, 2b,* and *t* respectively. For isotropic linear elastic thin plates, the stress distributions were examined in the previous chapters and the main parameters affecting the buckling loads and modes were investigated. It was also observed that the plate geometry and relative closeness of the crack to the boundaries may affect the symmetry of the buckling modes. Based on the observations

and conclusions from the previous sections, a plate model which can represents more general coupled buckling/fracture behaviour is desirable. Under the previous results, a plate with a width-length aspect ratio (2b/l) of 0.5 was chosen for postbuckling analysis. However, with this model, the effects of boundary conditions on the stress distribution around the cracks is relatively small. In this section, the results from a finite element postbuckling analysis for a plate with length of $L$ = 800 mm and width of $2b$ = 400 mm was chosen as a more interesting model. The crack length is $2a$ =200 mm and the plate thickness is $t$ =*1* mm for the plate model. The boundary conditions are the same as those used in section-six. All displacement boundary conditions at support-A are fixed (see Fig. 7-7), $u$ = 0, $v$ = 0, and $w$ = 0. Support-B displacements in y and z directions are fixed, i.e., $v$ = 0, and $w$ = 0, but in $x$-direction, displacements is free for loading purposes. The plate is loaded at support-B in x-direction with a uniformly distributed force $P$. The edges along x-directions are free in all directions and no any load is applied.

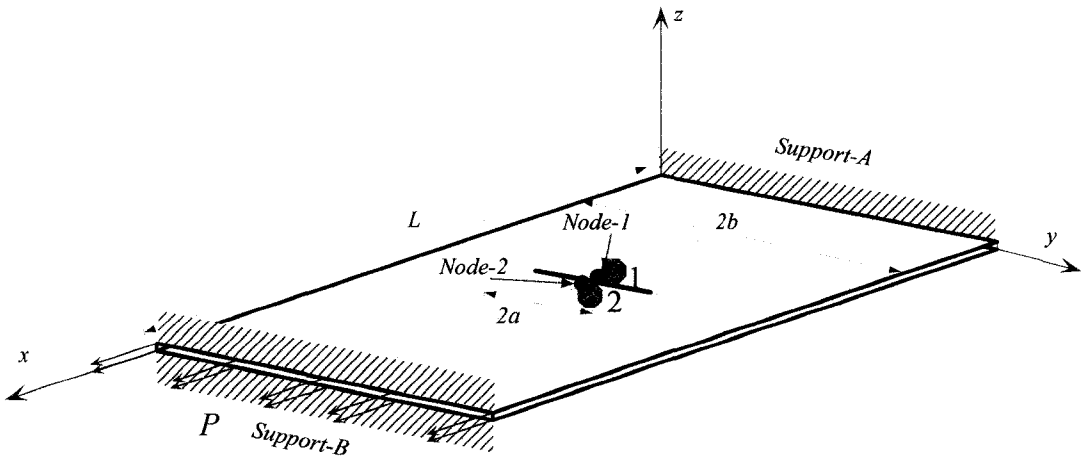


**Fig. 7-7** The geometry of centrally cracked plate

The first step in postbuckling analysis of a thin plate is to perform an eigenvalue analysis to determine the initial buckling load and mode shape. Then, the mode shape is used to perturb the plate for the postbuckling analysis purpose. In the analysis presented here, original (perfect) plate model coordinates were perturbed by five percent of the normalized buckling mode to make imperfect system.

The relative crack center displacement, in axial direction is shown in the Fig. 7-8. The load step is normalized with respect to the critical buckling load to identify the postbuckling behavior clearly. Bilinear load-displacement behavior occurs during the loading. The relative displacements of the crack centers increase linearly until the initial buckling occurs. It can be seen in the Fig. 7-8, that local buckling causes the relative crack center displacements to increase more rapidly than in the pre-buckled state. This demonstrates that linear elastic fracture analysis may not correctly predict fracture behaviour for structures that exhibits coupled buckling/fracture.

The crack center out-of-plane displacements (in the $z$-direction) is shown in the Fig. 7-9. The smooth transition from pre-buckling to postbuckling can be attributed to the imperfect system. For a perfect system, this behavior would exhibit classical bifurcation buckling. The effect of large deformation after the initiation of buckling can be seen in the Fig. 7-9.

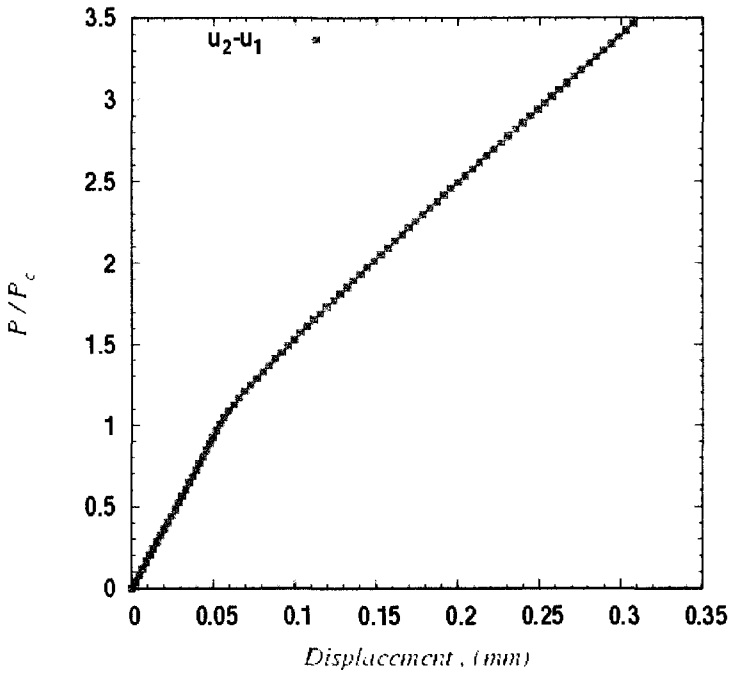


**Fig. 7-8** Crack opening displacement in x-direction

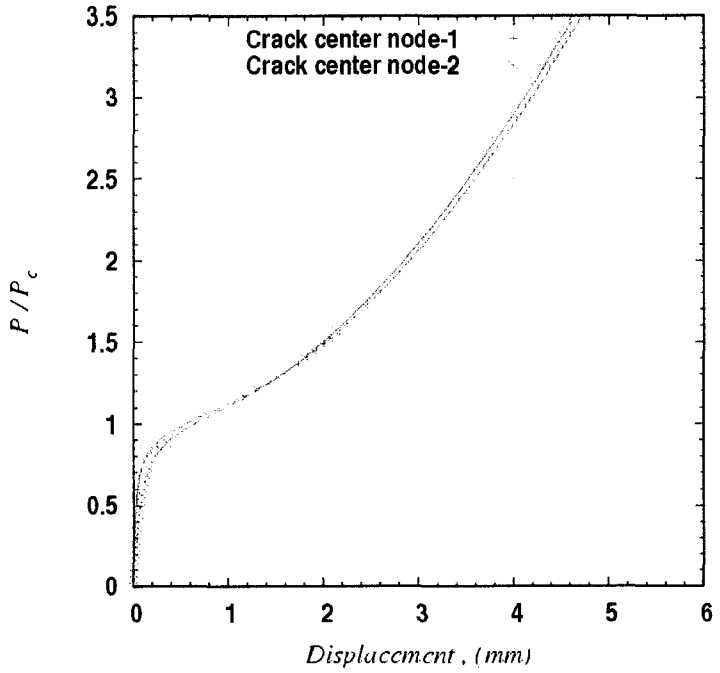


**Fig. 7-9** Displacements of crack centers in z-direction

Fig. 7-10 shows the crack center displacements in $x$-direction during the loading. Note that the crack center labelled 1 is on the side of the all-fixed boundary (Fig. 7-7) and the second crack center is on the side of the crack located close to the loading boundary. The crack center displacements in the $x$-direction increase linearly with different linear proportionalities until the buckling occurs. Then, the first crack center almost remains constant, but the second crack center increases linearly at different rate than in the pre-buckled state. This behaviour can be attributed to the non-symmetric boundary conditions. It can be concluded that the crack center displacements are quite sensitive to boundary conditions.

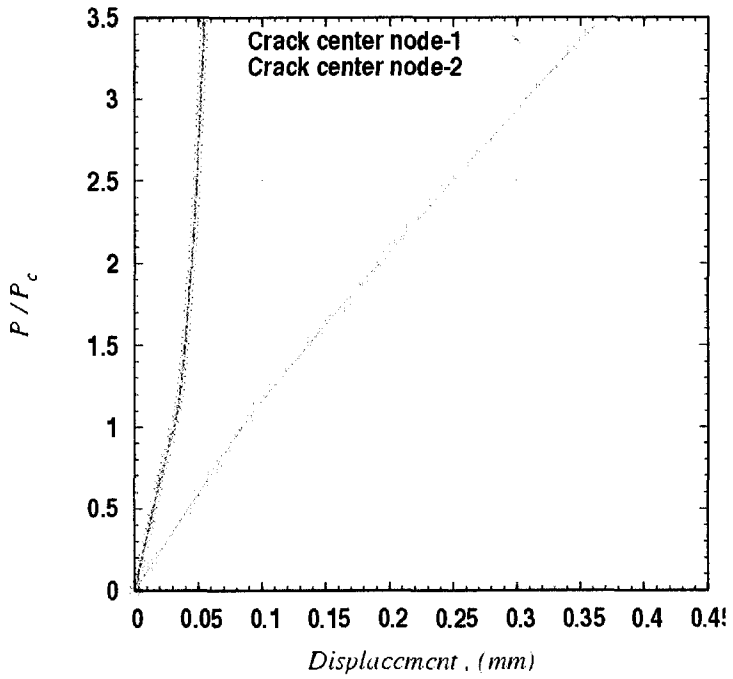


**Fig. 7-10** Displacements of crack centers in x-direction

The history of the mode-I stress intensity factor (SIF) $K_I$ for the right-hand side crack tip is shown in the Fig. 7-11. The crack tip has four nodes through the thickness of the plate (32-Node or 26-Node cubic elements) when there is only one layer of elements throughout the thickness of the plate. Node 4 is located on the surface that "pops-out" when buckling occurs. The mode-I SIF history of each of crack tip node through the thickness is slightly different than each other especially after buckling. The most significant change in the fracture behavior during the postbuckling analysis is a change in the slope of the mode-I SIF with respect to the applied load just after the buckling. The red straight line in the Fig. 7-11 shows the linear mode-I SIF history which can be obtained from the following equation [42].

$$K_I = \sigma\sqrt{\pi a}\sqrt{\sec\left(\frac{\pi a}{2b}\right)}\left[1-0.025\left(\frac{a}{b}\right)^2+0.06\left(\frac{a}{b}\right)^4\right] \tag{7.9}$$

Note that the loading is normalized with respect to the first critical buckling load $P_{cr}$ which was obtained from the buckling analysis previously. The most significant change in the $K_I$ among the crack tip nodes occurs at node-4 because of its location on the outer edge in the buckling direction. It should be noted that for a fixed load, $K_I$ is greater in the post-buckled configuration, than would be predicted from a classical linear elastic fracture mechanics analysis

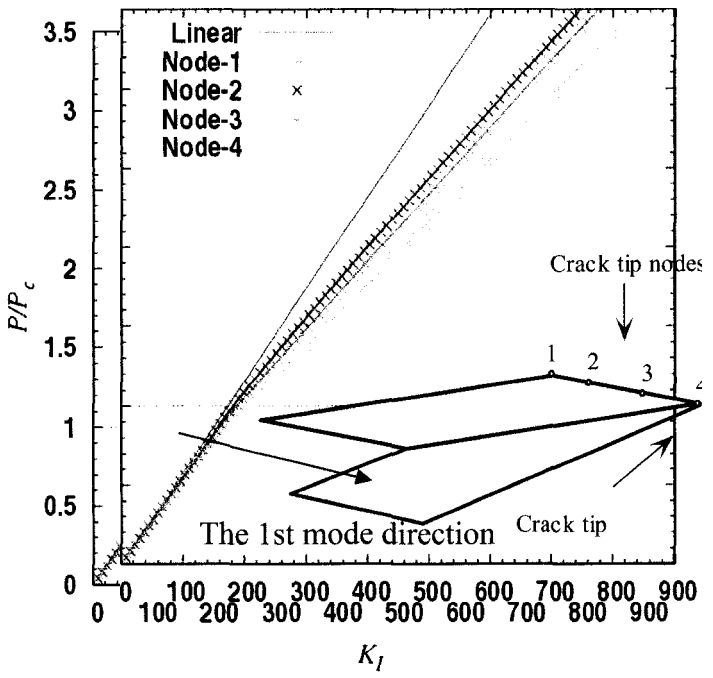


**Fig. 7-11** Load versus the stress intensity factor, $K_I$, during the postbuckling

The mode-I strain energy release rate, $G_I$, history is shown in the Fig. 7-12. $G_I$ can be given in terms of

$$G_I = \frac{K_I^2}{E} \tag{7.10}$$

The red solid curve in the Fig. 7-12 shows the $G_I$ history during the loading. It is obvious that the strain energy release rate history during postbuckling analysis is quite different than that obtained from linear analysis. This again shows the importance of accurate fracture modeling in post-buckled state, since the linear analysis underestimates the strain energy release rate for a given load.

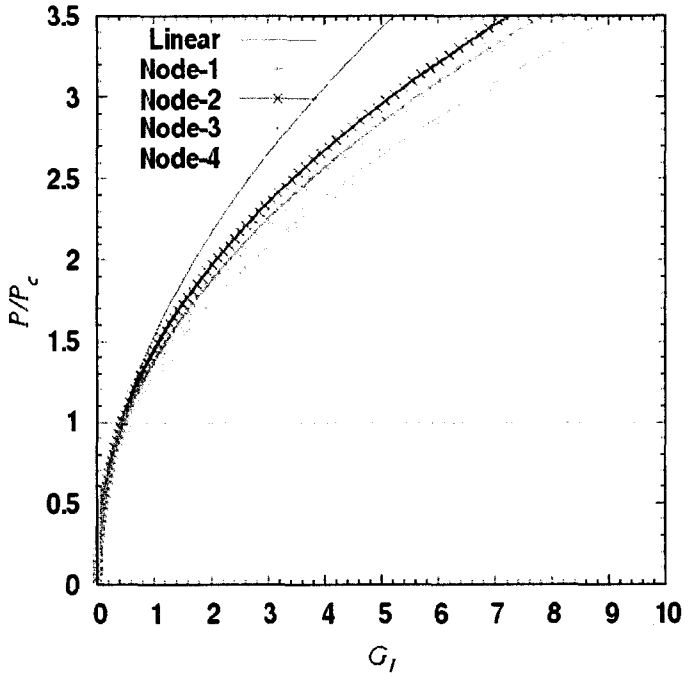


**Fig. 7-12** Load versus the energy release rate, $G_I$ , during postbuckling

When the buckling causes out-of-plane displacements in thin cracked plates, the crack tip becomes inclined in the y-z plane and introduces additional internal axial and shear stress components. As a consequence, mode-II and Mode-III ( $K_{II}$ and $K_{III}$ ) stress intensity factors enter into the solution. $K_{II}$ and $K_{III}$ are calculated directly in FRA3D. Fig. 7-13 shows the ratio of numerical and theoretical stress intensity factors $K_I$. This figure again clearly shows that linear elastic solution underestimates $K_I$ in post-buckled state. The Fig. 7-14 and Fig. 7-17 show the $K_{II}$ and $K_{III}$ history during the postbuckling analysis. It is known that the analytical $K_{II}$ and $K_{III}$ values are zero for the perfect plates with straight cracks and under uniaxial loading. The additional in-and out-of the plate-plane stresses around the crack tip can be calculated using the $K_{II}$ and $K_{III}$ [42].

The stress intensity factors $K_{II}$ and $K_{III}$ are small compared to $K_I$, for example, the maximum value of the $K_{II} / K_I$ and $K_{III} / K_I$ ratios are 0.02 and -0.01 respectively around the buckling load level $\left(P / Pcr = 1.0\right)$ (Fig. 7-15, Fig. 7-18). Thus, it appears as though the most important impact buckling has on fracture in this case, is the effect on $K_I$ and not on the introduction of small contributions from $K_{II}$ and $K_{III}$. The energy release rates for the mode-II and mode-III are shown on the figures Fig. 7-16 and Fig. 7-19. They can be calculated from the relation

$$G_i = \frac{K_i^2}{E'}, \quad i = I, II, \text{ and } III \tag{7.11}$$

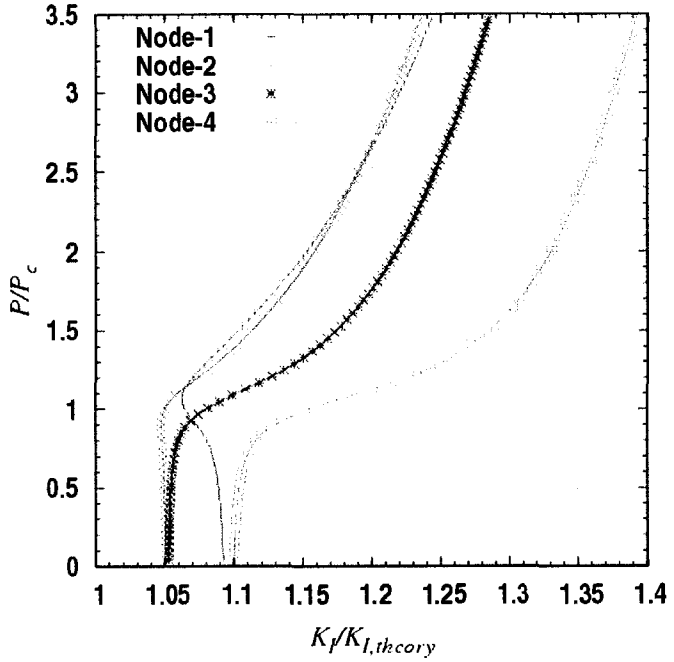


**Fig. 7-13** The ratio of numerical and theoretical $K_I$

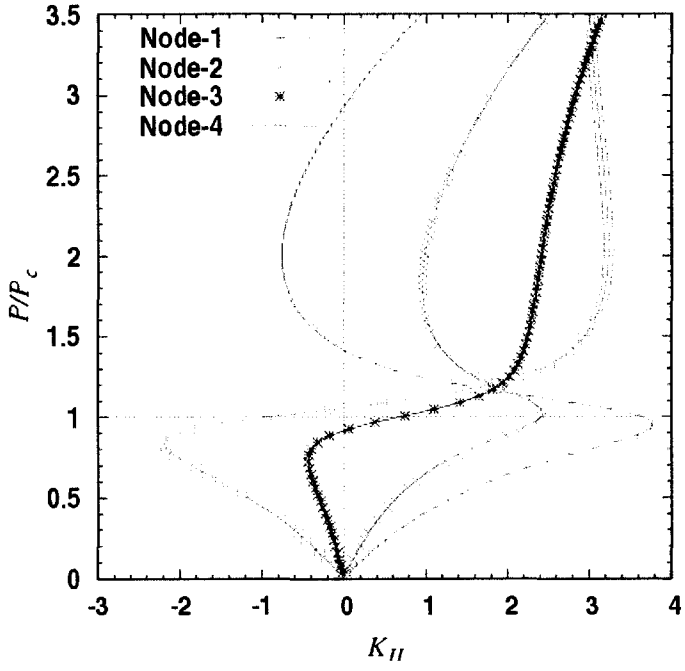


**Fig. 7-14** Load versus the stress intensity factor, $K_{II}$, during the postbuckling

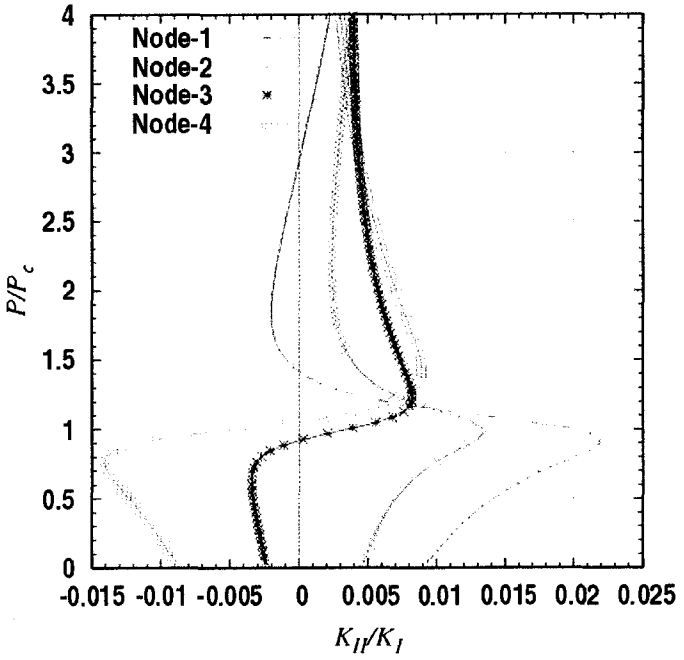


**Fig. 7-15** The ratio of $K_{II} / K_I$ during the loading

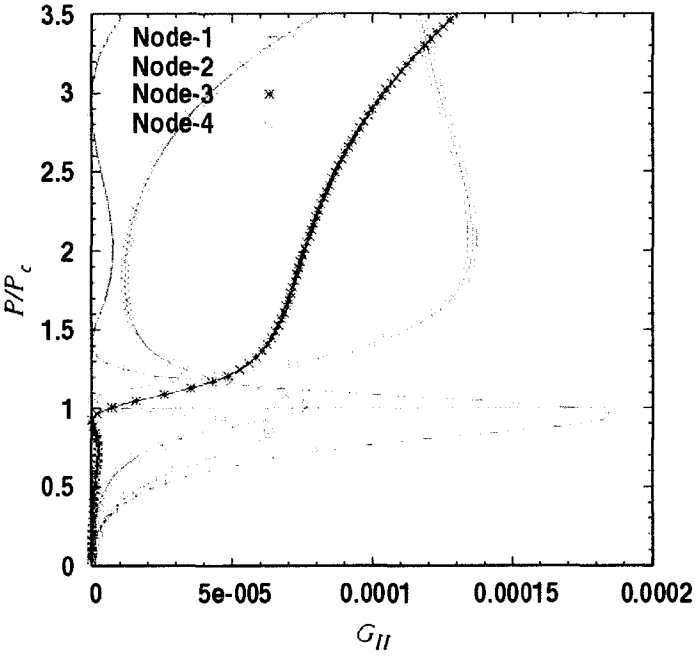


**Fig. 7-16** Load versus the energy release rate, $G_{II}$, during the postbuckling

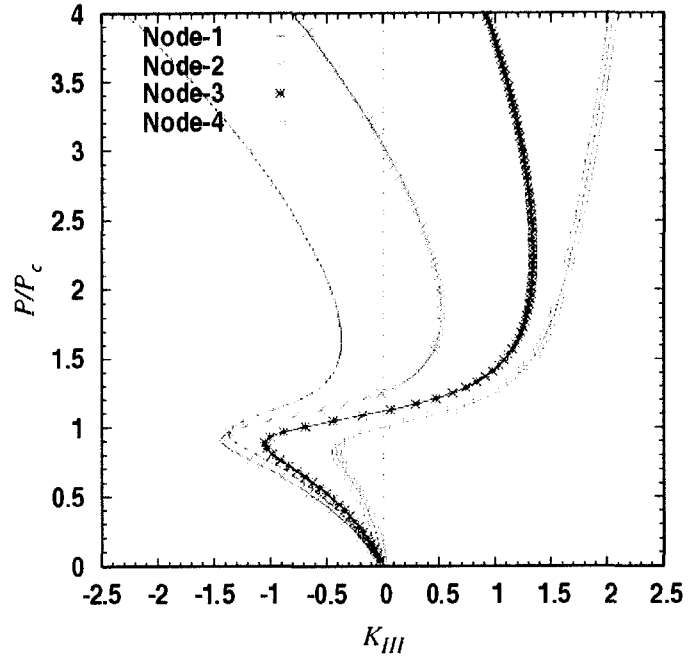


**Fig. 7-17** Load versus the stress intensity factor, $K_{III}$ , during the postbuckling

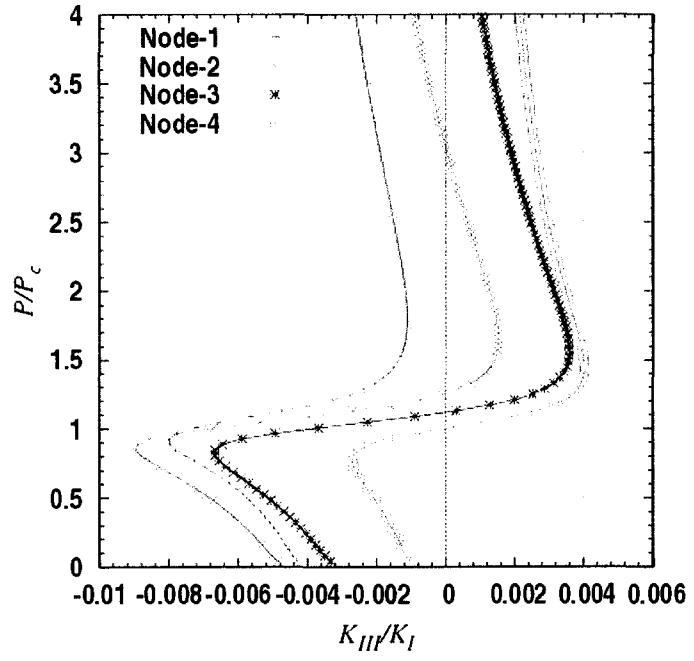


**Fig. 7-18** The ratio of $K_{III} / K_I$ during the loading

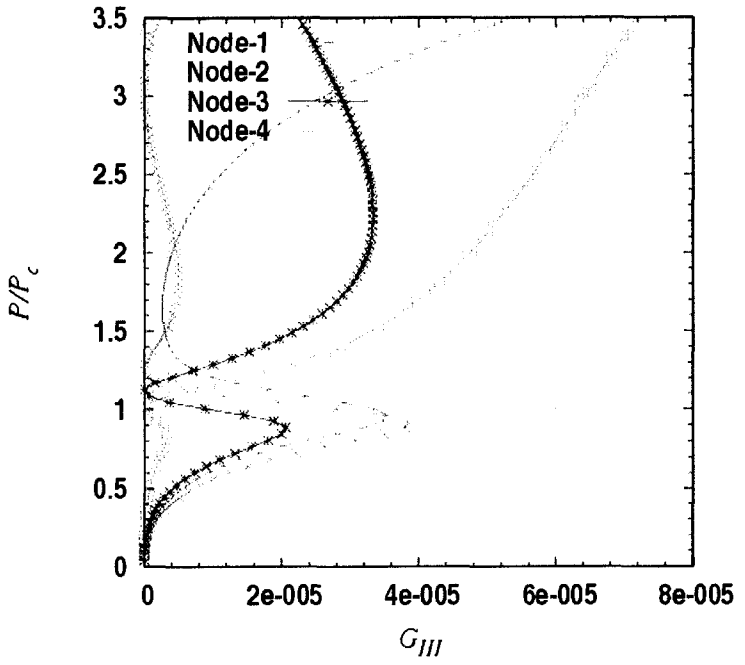


**Fig. 7-19** Load versus the energy release rate, $G_{III}$ , during the postbuckling

## 7.5 Summary

A method of perturbing the structure based on the eigen analysis to handle postbuckling analysis was developed. The imperfect system approach overcomes certain computational difficulties in postbuckling analysis, i.e., the transition from the pre-buckled state to the post-buckled state. Based on the postbuckling analysis procedure defined in this section, a thin plate with a straight central crack was examined to trace fracture information during the loading history. Because of the three-dimensional character of the fracture problem, $K_I, K_{II}$ and $K_{III}$ are computed.

Some new facts were revealed regarding the physics of the problem. These results from these calculations can be summarized as follows;

I. The coupling of buckling and fracture increases the magnitude of the stress intensity factors.

II. Planar analysis of fracture may not be suitable for thin plates that buckle.

III. Pre-buckling and postbuckling states exhibits different fracture behavior

IV. The mode-I stress intensity factor $K_I$ shows bilinear behavior. The slope of the load-$K_I$ relation changes after initial buckling.

V. The most significant changes occurs in the mode-I fracture parameters, i.e., $K_I$ and $G_I$

VI. During postbuckling, the mode-II and III fracture parameters are relatively insignificant as compared to those of the mode-I stress intensity factor.

# CHAPTER EIGHT: CONCLUSION AND FUTURE WORK

## 8.1 Conclusion

The coupled buckling/fracture problem occurs in a variety of forms and in different types of structures. Analytical solutions for most coupled buckling/fracture problems appear to be intractable. The finite element method is a convenient numerical tool to analyze these nonlinear problems. The FRAC3D finite element program was modified to solve this class of problems. The enriched crack tip element which was previously implemented into the code, correctly embeds crack tip stress singularity into the problem. Eigen-solver and geometrically nonlinear analysis capability were implemented into FRAC3D program, which can now correctly be used to analyze buckling/fracture problems.

Coupled fracture/buckling problems requires both eigen- and postbuckling analysis, because of the bifurcation type of behavior. The eigen-analysis enables us to find the critical load which causes buckling and the buckling mode shapes. The FRAC3D finite element program was extended with an eigen-solver to handle general buckling problems. The implemented eigen-solver uses the subspace iteration method. This method is one of the most efficient and widely accepted methods for the solution of large eigen systems. The method calculates given $n$ number of eigen-values (in ascending order) and the corresponding eigen-modes (the buckling mode shapes).

Postbuckling behavior is an inherently a nonlinear problem. Because of the finite change in geometry in the neighborhood of the buckled region, large displacements and rotations can develop. New stress and strain definitions are required for the geometrically nonlinear finite element problem. The FRAC3D finite element program was modified to solve these geometrically nonlinear problems using a "total Lagrangian formulation".

Finite element analysis of stability problems requires special nonlinear solution methods, e.g. path following methods, to overcome the difficulties associated with bifurcation in the solution path. In bifurcation type instability problems, the tangent stiffness of the system vanishes at the critical load, i.e. the determinant of the system's tangent-stiffness matrix becomes zero. If geometrical imperfections are present, the perturbed deflection will smoothly commence at the beginning of loading. The problem then becomes a load-deflection problem rather than a bifurcation problem. The imperfect structure approach is one of a number of alternative methods to handle bifurcation type buckling problems. In this study, the imperfect structure was generated using a perturbation on the perfect structure geometry based on percentage of the normalized buckling mode(s).

The finite element codes, eigen-solver and geometrically nonlinear analysis formulation, were tested with a number of benchmark problems. The benchmark results were in good agreement with the analytical results. Some small differences in the benchmark calculations can be attributed to the solution methods, e.g., round-off errors, and difference between 3-D and 2-D assumptions.

The local buckling of a cracked plate subjected to tensile loads was analyzed using the modified FRAC3D program. The stress distributions around the crack and cutouts before buckling was examined using exact analytical formulations. Based on the investigation of the compressive stress distributions, an empirical closed form solution was proposed to predict buckling loads. The pattern of the compressive stress distribution, which causes local buckling, around the crack or cutouts was analyzed. The effect that geometric parameters, such as the crack length, plate thickness, and crack inclination angle, have on the buckling loads was examined in detail. It was found that the buckling load is directly proportional to $(t/2a)^2$, square of plate thickness-half of the crack length ratio. If the plate is long enough so that the boundary conditions do not effect stress distribution around the crack, then the plate size does not seem to strongly affect the buckling stress. Crack inclination angle is another important factor affecting the buckling load. As the inclination angle decreases, the critical buckling load increases. A limited investigation on the effect of inclination angle was carried out.

The postbuckling analysis of a coupled fracture/buckling problems shows that linear fracture analysis underestimates the fracture parameters such as, stress intensity factors, energy release rate etc. for a given load level. Postbuckling analysis of a plate with a crack aspect ratio of 0.5 subjected to an axial load was presented. It was observed the postbuckling introduces mixed mode (mode-II and III) fracture after the critical buckling load level. But, the mixed mode fracture contribution caused by out-of-plane buckling is insignificant compared to the mode-I contribution.

## 8.2 Future Work

The numerical examples given in this study consisted of a few types of special three dimensional buckling/fracture problems e.g., thin plates with cracks. However, more complex structures that exhibit coupled buckling/fracture behavior can be analyzed using the code that was developed during this study. Examples of complex three dimensional coupled buckling/fracture problems would include non-axisymmetric blister formations in thin film (electronic packaging), non-symmetric delaminations in composites, etc.

Future extensions of this work would include 3-D buckling/fracture calculations for the structures that may exhibit a strong variation of mixed-mode stress intensity factors along the crack front. In addition, contact conditions can be incorporated into the buckling/fracture model so that crack surface contact is permitted.

In the chapter 2, a semi-closed formula was developed to predict the critical local buckling loads for the cracked plates with straight central cracks. However, a more general form of the formula, including the angle of inclination and plate size, can also be derived. But, this requires more computational runs to verify the formula.

# REFERENCES


[1] T.-C. Chiu and F. Erdogan, "Debonding of graded coatings under in-plane compression," *International Journal of Solids and Structures*, vol. 40, pp. 7155-7179, 2003.

[2] F. Erdogan and T.-C. Chiu, "Plane strain and axisymmetric spallation of graded coatings under thermal loading," *Journal of Thermal Stresses*, vol. 26, pp. 497-523, 2003.

[3] A. O. Ayhan, "Finite Element Analysis of Nonlinear Deformation Mechanisms in Semiconductor Packages.," Ph.D. Thesis. *Mechanical Engineering and Mechanics Department*. Bethlehem: Lehigh University, 1999.

[4] A. Ayhan, O. and and H. F. Nied, "Stress intensity factors for three dimensional surface cracks using enriched finite elements," *Int. Journal for Numerical Methods in Engineering*, vol. 54, pp. 899-921, 2002.

[5] T. d. Jong, "Delamination buckling of Fiber Metal Laminates," : http://www.vm.lr.tudelft.nl/education/masterprojects.php?id=4, 2004.

[6] E. R. Moore, "Analysis of Buckling in Thin Epoxy Films Due to Thermal/Moisture Induced Stresses," Master Thesis. *Mechanical Engineering Department*. Bethlehem: Lehigh University, 1999.

[7] J. W. Park, "Characterization of Interfacial Damage of Polymer Encapsulated Microelectronic Devices," Ph.D. Thesis, *Material Science Department*. Bethlehem: Lehigh University, 1998.

[8] B. Yildirim, "Nonlinear Thermal Stress/Fracture Analysis of Multilayer Structures Using Enriched Finite Elements," Ph.D. Thesis *Mechanical Engineering and Mechanics*. Bethlehem: Lehigh University, 2000, pp. 250.

[9] G. Cherepanov, P., "On the buckling under tension of a membrane containing holes," *Appl. Math. Mech. Translation of PMM*, vol. 27, pp. 405-420, 1963.

[10] R. G. Forman and A. S. Kobayashi, "On the Axial Rigidity of Perforated Strip and the Strain Energy Release Rate in a Centrally Notched Strip Subjected to Uniaxial Tension," *Journal of Basic Engineering*, pp. 693-699, 1964.

[11] M. Petyt, "The vibration characteristics of a tensioned plate containing a fatigue crack," *Journal of Sound and Vibration*, vol. 8, pp. 377-389, 1968.

[12] J. Dixon, R. and J. S. Strannigan, "Stress Distribution and buckling in thin sheets with central slits," presented at *Second International conference on Fracture*, Brighton, U.K., 1969.

[13] G. Zielsdorff, F. and R. Carlson, L., "On the Buckling of Tensioned Sheets with Cracks and Slots," *Engineering Fracture Mechanics*, vol. 4, pp. 939-950, 1972.

[14] A. Gilabert, P. Sibillot, D. Sornette, C. Vanneste, D. Maugis, and F. Muttin, "Buckling Instability and Pattern around the Holes or Cracks in Thin Plates under a Tensile Load," *Europian Journal of Mechanics and Solids*, vol. 11, pp. 65-89, 1992.

[15] M. S. Dyshel and O. B. Milananova, "A method of experimentally Analyzing the Instability of Plates with slits," *Translation of Prikladnaya Mekhanika*, vol. 13, pp. 491-495, 1977.

[16] M. S. Dyshel, "Stability of Thin Plates with Cracks under Biaxial Tension," , vol. 18, pp. 924-928, 1982.

[17] J. W. Hutchinson and Z. Suo, "Mixed Mode Cracking in Layered Materials," in *Advances in Applied Mechanics*, vol. 29, J. W. Hutchinson and T. Y. Wu, Eds.: Academic Press, 1992, pp. 63-191.

[18] Volinsky, "Experiments with in-situ thin film telephone cord buckling delamination propagation," presented at Mat. Res. Soc. Symp. Proc. Vol. 749, 2003.

[19] C. Wang, *Applied Elasticity*. New York: McGraw-Hill, 1953.

[20] Maugis, "Stresses and Displacements Around Cracks and Elliptical Cavities: Exact Solutions," *Engineering Fracture Mechanics*, vol. 43, pp. 217-255, 1992.

[21] W. Young, *Roark's Formulas for Stress and Strain*, 6th ed. New York: McGraw-Hill, 1996.

[22] M. Dyshel, Sh.,, "Stability under Tension of Thin Plates with Cracks," , vol. 14, pp. 1169-1173, 1978.

[23] W. F. Chen, *Constitutive equations for engineering materials*, vol. 1. Amsterdam, New York,: Elsevier, 1994.

[24] W. F. Chen and E. Mizuno, *Nonlinear analysis in soil mechanics*. Amsterdam: Elsevier, 1990.

[25] M. A. Crisfield, *Non-linear Finite Element Analysis of Solids and Structures, Volume 1*, vol. 1: John Wiley & Sons, 1991.

[26] W. Flugge, *Handbook of Engineering Mechanics*. New York: McGraw-Hill, 1962.

[27] S. P. a. G. Timoshenko, J. M., *Mechanics of Materials*. New York: D. Van Nostrand, 1972.

[28] C. Dym, L., *Stability theory and its applications to structural mechanics*. Leyden: Noordhoff, 1974.

[29] W. Press, H., S. Teukolsky, A, W. Vetterling, T., and B. Flannery, P, *Numerical recipes in FORTRAN*, 2 ed: Cambridge University Press, 1992.

[30] K. J. Bathe, *Finite Element Procedures*. Upper Saddle River, New Jersy: Prentice Hall, 1996.

[31] E. Riks, C. C. Rankin, and F. A. Brogan, "The Buckling Behavior of a Central Crack in a Plate Under Tension," *Engineering Fracture Mechanics*, vol. 43, pp. 529-548, 1992.

[32] A. Barut and E. Madenci, "Buckling of a Thin, Tension-Loaded, Composite Plate with an Inclined Crack," *Enginnering Fracture Mechanics*, vol. 58, pp. 233-248, 1997.

[33] D. Shaw and Y. H. Huang, "Buckling Behavior of a Central Cracked Thin Plate under Tension," *Engineering Fracture Mechanics*, vol. 35, pp. 1019-1027, 1990.

[34] T. Fujimoto and S. Seinoseku, "Local Buckling of Thin Tensioned Plate with a Crack," *Memoirs of the Faculty of Engineering, Kyashu University*, vol. 42, pp. 355-370, 1982.

[35] P.-L. Larsson, "On the Buckling of Orthotropic Stretched Plates with Circular Holes," *Composite Structures*, vol. 11, pp. 121-134, 1989.

[36] K. Markstorm and B. Storakers, "Buckling of Cracked Members under Tension," *International Journal of Solids and Structures*, vol. 16, pp. 217-229, 1980.

[37] A. Guz, N., G. Kuliyev, G., and I. Tsurpal, A., "On the Fracture of Brittle Materials from Loss of Stability near a Crack," *Engineering Fracture Mechanics*, vol. 10, pp. 401-408, 1978.

[38] M. S. Dyshel, "Failure in a Thin Plate with a Slit," *Translation of Prikladnaya Mekhanika*, vol. 14, pp. 1010-1012, 1978.

[39] M. Aliabadi, H. and Rooke, D., P., *Numerical Fracture Mechanics*, vol. 8. Southhampton, Boston: Kluwer Academeic Publishers, 1991.

[40] http://www.hks.com/reference/epaper/a97-2.pdf, "ABAQUS/Answers, "Static Postbuckling and Collapse Analysis Using the Modified Riks Procedure"," : HKS Inc., 1997.

[41] http://www.hks.com/reference/epaper/answers_winter_95.pdf, "Postbuckling of Imperfection Sensitivity Analysis," , vol. 195: HKS Inc., 1995.

[42] T. L. Anderson, *Fracture Mechanics, Fundamentals and its applications*, Second ed. Boca Raton: CRC Press, 1995.

[43] S. E. Benzley, "Representation of Singularities with Isoparametric Finite Elements," *Int. Journal of Numerical Methods in Engineering*, vol. 8, pp. 537-545, 1974.

# APPENDIX A: ENRICHED CRACK TIP ELEMENTS

## A.1 INTRODUCTION

Efficient computation of 3-D stress intensity factors can be performed using special crack tip elements. There are various numerical techniques to handle the crack tip singularity in two and three dimensional fracture analysis. These methods are mainly, boundary element method, alternating methods, virtual crack extension, line-spring method and suitably modified finite methods. The details of these numerical methods can be found in literature [[32, 39, 42, 43]]. Among the modified finite element methods, the enriched crack tip element method is very effective for direct calculation of stress intensity factors [3, 4].

A description of the enriched element used in the FRAC3D finite element code is described in ref [3]. This method is a 3-D extension of concepts introduced in [43]. It is basically the embedding of the closed form asymptotic crack tip displacement field into the regular isoparametric element with the stress intensity factors as additional unknowns. Inter-element displacement compatibility between regular and enriched element surfaces is satisfied by the use of "transition" elements. Transition elements are modified enriched elements in which a smoothing function is introduced so that asymptotic crack tip displacement field smoothly vanishes at the regular element surface. The geometry and crack front coordinate system of the enriched element needed to define the asymptotic displacement field are shown in the Fig. 0-1,

elements including transition and regular elements surrounding enriched element are shown on the Fig. 0-2.

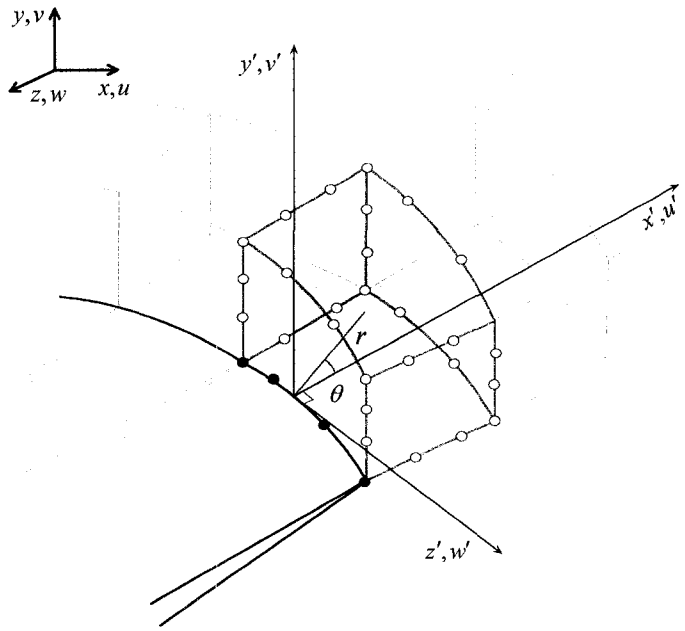


**Fig. 0-1** Enriched element model

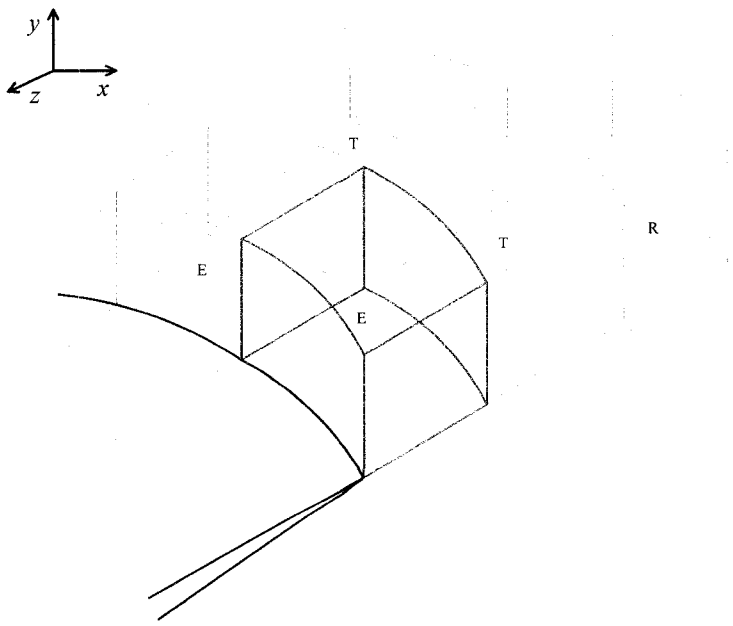


**Fig. 0-2** Enriched, transition and regular elements around the crack tip

The displacement field in x, y and z directions for an enriched element can be written respectively as

$$u(\xi,\eta,\rho)=\sum_{i=1}^{n}N_i(\xi,\eta,\rho)u_i+Z_0(\xi,\eta,\rho)\begin{Bmatrix}K_I(\Gamma)F_1(\xi,\eta,\rho)+\\K_{II}(\Gamma)G_1(\xi,\eta,\rho)+\\K_{III}(\Gamma)H_1(\xi,\eta,\rho)\end{Bmatrix} \tag{12}$$

$$v(\xi,\eta,\rho)=\sum_{i=1}^{n}N_i(\xi,\eta,\rho)v_i+Z_0(\xi,\eta,\rho)\begin{Bmatrix}K_I(\eta)F_2(\xi,\eta,\rho)+\\K_{II}(\eta)G_2(\xi,\eta,\rho)+\\K_{III}(\eta)H_2(\xi,\eta,\rho)\end{Bmatrix} \tag{13}$$

$$w(\xi,\eta,\rho)=\sum_{i=1}^{n}N_i(\xi,\eta,\rho)w_i+Z_0(\xi,\eta,\rho)\begin{Bmatrix}K_I(\Gamma)F_3(\xi,\eta,\rho)+\\K_{II}(\Gamma)G_3(\xi,\eta,\rho)+\\K_{III}(\Gamma)H_3(\xi,\eta,\rho)\end{Bmatrix} \tag{14}$$

where, the first terms are identical to the interpolation expressions used for regular isoparametric element displacement fields. The second term includes the analytic expressions for asymptotic displacement fields near the crack tip. $N_i(\xi,\eta,\rho)$'s are the conventional element shape functions expressed in terms of local coordinates, where $u_i$, $v_i$, and $w_i$ are the nodal displacements in the *x*, *y*, and *z* directions respectively. The total number of nodes is n. $K_I(\Gamma)$, $K_{II}(\Gamma)$, and $K_{III}(\Gamma)$, are the mode I, II and III stress intensity factors, which are function of the local coordinate $-1\le\Gamma\le1$ along the crack front defined by the interpolation functions $N_j(\Gamma)$, i.e.,

$$K_I(\Gamma)=\sum_{j=1}^{m}N_j(\Gamma)K_I^j \tag{15}$$

$$K_{II}(\Gamma)=\sum_{j=1}^{m}N_j(\Gamma)K_{II}^j \tag{16}$$

$$K_{III}(\Gamma) = \sum_{j=1}^{m} N_j(\Gamma) K_{III}^j \tag{17}$$

In (4)-(6) $m$ is the number of crack front nodes in the enriched element. The unknown nodal stress intensity factors at the crack front nodes are $K_I(\Gamma)$, $K_{II}(\Gamma)$, and $K_{III}(\Gamma)$,. For example, a 32-node enriched cubic element has 4 crack front nodes and the mode I crack front stress intensity factor distribution can be expressed as

$$K_1(\Gamma) = K_1(\eta) = -\frac{1}{16}(1-9\eta^2)(1-\eta)K_I^1 + \frac{9}{16}(1-\eta^2)(1-3\eta)K_I^2 + \frac{9}{16}(1-\eta^2)(1+3\eta)K_I^3 - \frac{1}{16}(1-9\eta^2)(1+\eta)K_I^4 \tag{18}$$

where, the functions as coefficients of the nodal intensity factors corresponds to the shape functions. These shape functions are also used to interpolate the crack front nodal coordinates, i.e.,

$$x(\Gamma) = \sum_{j=1}^{m} N_j(\Gamma) x_i, \quad y(\Gamma) = \sum_{j=1}^{m} N_j(\Gamma) y_i, \quad z(\Gamma) = \sum_{j=1}^{m} N_j(\Gamma) z_i \tag{19}$$

Depending upon which edge of the enriched element touches the crack front, the local crack front can be expressed in terms of local coordinate line, i.e., $\Gamma$ can be either, $\Gamma = \xi$, $\eta$, or $\rho$. The asymptotic displacements in the enriched element are given by the following equations

$$F_i(\xi,\eta,\rho) = f_i(\xi,\eta,\rho) - \sum_{j=1}^{n} N_j(\Gamma) f_{ij} \tag{20}$$

$$G_i(\xi,\eta,\rho) = g_i(\xi,\eta,\rho) - \sum_{j=1}^{n} N_j(\Gamma) g_{ij} \tag{21}$$

$$H_i(\xi,\eta,\rho) = h_i(\xi,\eta,\rho) - \sum_{j=1}^{n} N_j(\Gamma) h_{ij} \quad , \tag{22}$$

where, $f_i, g_i$, and $h_i$ *(i=1,2,3)* are the well known asymptotic displacement functions which are the functions necessary to compute the stress intensity factors $K_I(\Gamma)$, $K_{II}(\Gamma)$, and $K_{III}(\Gamma)$,. Nodal constants, $f_{ij}, g_{ij}$, and $h_{ij}$ are the asymptotic crack tip displacements calculated at the *j*th nodes. The asymptotic displacement field can be for any kind of crack interface, ie. it can be isotropic, orthotropic, etc. The displacements, including contributions from the mode-I mode-II and mode-III in in the local coordinate system can be written as

$$\begin{Bmatrix} u' \\ v' \\ w' \end{Bmatrix} = \begin{bmatrix} f_1' & g_1' & 0 \\ f_2' & g_2' & 0 \\ 0 & 0 & h_1' \end{bmatrix} \begin{Bmatrix} K_I \\ K_{II} \\ K_{III} \end{Bmatrix} \quad . \tag{23}$$

For an isotropic fracture analysis, the asymptotic crack tip displacements are given by

$$f_1' = \frac{1}{2G}\sqrt{\frac{r}{2\pi}}\cos\left(\frac{\theta}{2}\right)\left[\kappa - 1 + 2\sin^2\left(\frac{\theta}{2}\right)\right] \quad , \tag{24}$$

$$g_1' = \frac{1}{2G}\sqrt{\frac{r}{2\pi}}\sin\left(\frac{\theta}{2}\right)\left[\kappa + 1 + 2\cos^2\left(\frac{\theta}{2}\right)\right] \quad , \tag{25}$$

$$f_2' = \frac{1}{2G}\sqrt{\frac{r}{2\pi}}\sin\left(\frac{\theta}{2}\right)\left[\kappa + 1 - 2\cos^2\left(\frac{\theta}{2}\right)\right] \quad , \tag{26}$$

$$g_2' = -\frac{1}{2G}\sqrt{\frac{r}{2\pi}}\cos\left(\frac{\theta}{2}\right)\left[\kappa - 1 - 2\sin^2\left(\frac{\theta}{2}\right)\right] \quad , \tag{27}$$

$$h' = \frac{1}{G}\sqrt{\frac{r}{2\pi}}\sin\left(\frac{\theta}{2}\right), \tag{28}$$

where, $G=E/2(1+\mu)$ is the shear modulus, $\mu$ is Poisson's ratio, and $\kappa=3-4\mu$. All of these equations are in the local coordinate system. Transformation of the asymptotic displacements from the local coordinate system to a global system can be done with

$$\begin{Bmatrix} U \\ V \\ W \end{Bmatrix} = \begin{bmatrix} \cos(x',x) & \cos(x',y) & \cos(x',z) \\ \cos(y',x) & \cos(y',y) & \cos(y',z) \\ \cos(z',x) & \cos(z',y) & \cos(z',z) \end{bmatrix} \begin{Bmatrix} u' \\ v' \\ w' \end{Bmatrix} = \begin{bmatrix} a_{11} & a_{12} & a_{13} \\ a_{21} & a_{22} & a_{23} \\ a_{31} & a_{32} & a_{33} \end{bmatrix} \begin{Bmatrix} u' \\ v' \\ w' \end{Bmatrix}, \tag{29}$$

where, cos(a,b) represents the angle between $a$ in the local coordinates and $b$ at the global coordinates. Note that the displacements obtained from the equation (29) are asymptotic displacements in the global coordinates.

$$\begin{Bmatrix} U \\ V \\ W \end{Bmatrix} = \begin{bmatrix} a_{11}f_1'+a_{21}f_2' & a_{11}g_1'+a_{12}g_2' & a_{13}h_1' \\ a_{21}f_1'+a_{22}f_2' & a_{21}g_1'+a_{22}g_2' & a_{23}h_1' \\ a_{31}f_1'+a_{32}f_2' & a_{31}g_1'+a_{32}g_2' & a_{33}h_1' \end{bmatrix} \begin{Bmatrix} K_I \\ K_{II} \\ K_{III} \end{Bmatrix}, \tag{30}$$

$$\begin{Bmatrix} U \\ V \\ W \end{Bmatrix} = \begin{bmatrix} a_{11} & a_{12} & a_{13} \\ a_{21} & a_{22} & a_{23} \\ a_{31} & a_{32} & a_{33} \end{bmatrix} \begin{bmatrix} f_1' & g_1' & 0 \\ f_2' & g_2' & 0 \\ 0 & 0 & h_1' \end{bmatrix} \begin{Bmatrix} K_I \\ K_{II} \\ K_{III} \end{Bmatrix}, \tag{31}$$

$$\begin{Bmatrix} U \\ V \\ W \end{Bmatrix} = \begin{bmatrix} f_1 & g_1 & h_1 \\ f_2 & g_2 & h_2 \\ f_3 & g_3 & h_3 \end{bmatrix} \begin{Bmatrix} K_I \\ K_{II} \\ K_{III} \end{Bmatrix}. \tag{32}$$

Using the transformation in Eq. (32), the terms in Eq's (24) (25) (26),(27), and (28) are transformed asymptotic displacement fields and $f_{ij}$ at each node are calculated.

# VITAE

Mehmet Sahin was born in Oltu, Erzurum, Turkey on March 18$^{th}$ , 1962. He is the fifth out of sixth children of Dursun and Hamide Sahin. He finished elementary, middle, and high school in Erzurum, Turkey. He graduated from Civil Engineering Department of METU, Ankara, Turkey, in January, 1988 with B.S degree. After graduation, he worked at Unverdi Inc. as director. He joined army in March 1989. After the military service, He returned to his previous company, Unverdi Inc. He joined Ataturk University in 1991. He has worked as a research assistant until the end of 1991. He received his MS degree in civil engineering from Cleveland State University at 1993. He joined Lehigh University in 1993 and got MS in Civil Engineering at 1998.